Distributed H_∞ Control of Segmented Telescope Mirrors

by

Baris Ulutas
MSc, Bogazici University, 2008
BSc, Bogazici University, 2005

A Dissertation Submitted in Partial Fulfillment
of the Requirements for the Degree of

DOCTOR OF PHILOSOPHY

in the Department of Mechanical Engineering

Supervisory Committee

Distributed H_∞ Control of Segmented Telescope Mirrors

by

Baris Ulutas
MSc, Bogazici University, 2008
BSc, Bogazici University, 2005

Supervisory Committee

Dr. Afzal Suleman, Dept. of Mechanical Engineering, University of Victoria
Co-Supervisor

Dr. Edward J. Park, Dept. of Mechanical Engineering, University of Victoria
Co-Supervisor

Dr. Colin Bradley, Dept. of Mechanical Engineering, University of Victoria
Departmental Member

Dr. Issa Traore, Dept. of Electrical and Computer Engineering, University of Victoria
Outside Member

Abstract

Supervisory Committee
Dr. Afzal Suleman, Dept. of Mechanical Engineering, University of Victoria
Co-Supervisor
Dr. Edward J. Park, Dept. of Mechanical Engineering, University of Victoria
Co-Supervisor
Dr. Colin Bradley, Dept. of Mechanical Engineering, University of Victoria
Departmental Member
Dr. Issa Traore, Dept. of Electrical and Computer Engineering, University of Victoria
Outside Member

Segmented mirrors are to be used in the next generation of the ground-based optical telescopes to increase the size of the primary mirrors. A larger primary mirror enables the collection of more light, which results in higher image resolutions. The main reason behind the choice of segmented mirrors over monolithic mirrors is to reduce manufacturing, transportation, and maintenance costs of the overall system. However, segmented mirrors bring new challenges to the telescope design and control problem. The large number of inputs and outputs make the computations for centralized control schemes intractable. Centralized controllers also result in systems that are vulnerable to a complete system failure due to a malfunction of the controller.

Distributed control is a viable alternative that requires the use of a network of simple individual segment controllers that can address two levels of coupling among segments and achieve the same performance objectives. Since segments share a common support structure, there exists a coupling among segments at the dynamics level. Any control action in one segment may excite the natural modes of the support structure and disturb other segments through this common support. In addition, the objective of maintaining a smooth mirror surface requires minimization of the relative displacements among neighbouring segment edges. This creates another level of coupling generally referred to as the objective coupling.

This dissertation investigates the distributed H_∞ control of the segmented next generation telescope primary mirrors in the presence of wind disturbances. Three distributed H_∞ control techniques are proposed and tested on three segmented primary mirror models: the dynamically uncoupled model, the dynamically coupled model and the finite element model of Thirty Meter Telescope (TMT) project. It is shown that the distributed H_∞ controllers are able to satisfy the stringent imaging performance requirements.

Table of Contents

List of Tables

List of Figures

Acknowledgments

Foremost, I would like to express my sincere gratitude to my supervisors Dr. Afzal Suleman and Dr. Edward Park for their support, guidance, encouragement and most importantly for their patience.

Special thanks to my friend Kerem Karakoc for his invaluable help during my time in Canada.

I would like to thank my friends and colleagues, Bruno Rocha, Andre Carvalho, Ricardo Pavia, Adel Younis, Dan Kerley, Ali Taleb and many more for their friendship, support and kindness.

Special appreciation to Makosinski family and, all faculty and staff from Department of Mechanical Engineering.

Dedication

To my family

1. INTRODUCTION

1.1 Overview

From the early times of human history, heavens and heavenly bodies have always amazed people. Sumerians, Babylonians and Egyptians were the first civilizations who were quite advanced in the observation of the heavens and kept track of the heavenly bodies. By using the recordings of their observations of the celestial objects they invented calendars for agricultural purposes. In order to keep track of the movements of the heavenly bodies these early civilizations also developed complex mathematics that further enabled new discoveries in science and technology.

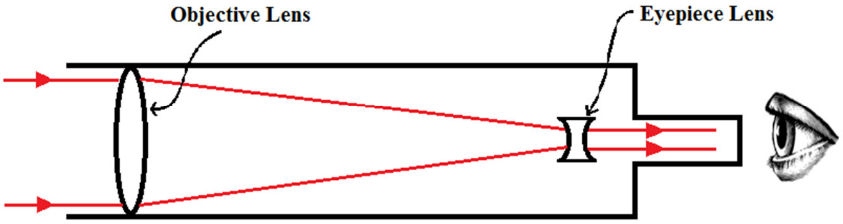

Figure 1-1.Refracting telescope design.

In order to observe heavens better and to understand its dynamics, various types of telescopes have been invented from very early recorded times. Although unclear, the Dutch spectacles-maker Liphershey is commonly accepted to be the inventor of the first refracting telescope. He filed his patent for the refracting telescope in 1608. Refracting telescopes use lenses to focus more light than a naked eye can see to be able to observe fainter objects in the sky. Figure 1-1 shows a refractive telescope design. In the following year, Galileo improved the first known telescope and proved the heliocentric model of the Copernicus by his numerous discoveries like the phases of Venus, the four largest satellites of Jupiter…etc. Although at first Galileo was objected by many, when telescopes became more available to the general public Copernicus heliocentric model gained acceptance. Following the Galileo's scientific breakthrough, Isaac Newton, who was born just two weeks before Galileo's death, started to get involved in the problem of the movements of the astral objects and investigated the movements of the heavenly bodies in his book “Mathematical Principles of Natural Philosophy”. In particular he focused on the falling moon problem and proved the inverse square law of gravitation. To be able to make calculations easier during his investigations of the heavens, he invented calculus. Newton also built the first known reflecting telescope that eliminates the chromatic aberration problem of the refracting telescopes in 1668. In Newton’s design, a small flat diagonal mirror as shown in Figure 1-2 is used to direct the reflected light from the main concave mirror to an eyepiece located on the side of the telescope tube. In 1672 Laurent Cassegrain used a convex secondary mirror instead of the flat diagonal one to direct the light to a central hole in the primary mirror. Although in his book Optica Promota (The Advance of Optics) James Gregory published his two mirror reflecting telescope design with two concave mirrors that is similar to the Cassegrain in 1663 (before Newton built his reflecting telescope), Robert Hooke was able to build the design five years after Newton’s first reflecting telescope in 1673. Figures 1-3 and 1-4 show the designs of Cassegrain and Gregory, respectively.

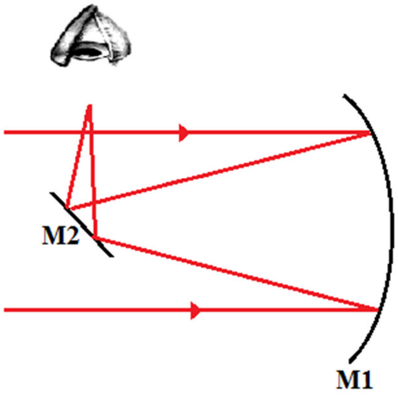

Figure 1-2.Newtonian reflecting telescope design.

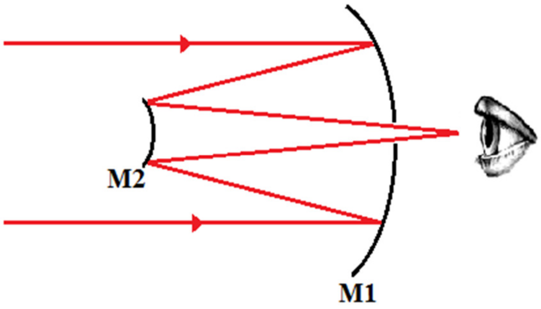

Figure 1-3.Cassegrain reflecting telescope design.

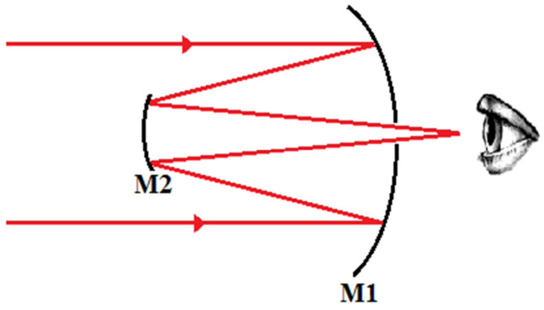

Figure 1-4.Gregorian reflecting telescope design.

As scientists tried to advance telescope technology with larger apertures, the resolution of the images obtained by the telescopes increased accordingly. The maximum attainable angular resolution α of a telescope is calculated as $\alpha = 1.22\lambda/D \approx \lambda/D$ where λ is the wavelength of the light to be observed and D is the diameter of the telescope aperture [1]. Figure 1-5 shows the increase in the size of the telescope apertures in history.

When the diameter of the optical apertures is increased over a certain point, the cost of the single monolithic mirror grows rapidly. In order to be cost effective, designers started to opt for hexagonal segmented mirrors when the mirror size exceeds 8 meters in diameter as calculations show that this number is a practical limit of a cost efficient monolithic design [2]. Today, most of the optical telescopes employ single monolithic mirrors less than eight meters in diameter. However, the largest optical telescopes and next generation telescopes employ segmented mirrors in their designs. Currently, two of the largest aperture ground-based optical telescopes in operation are the Gran Telescopio Canarias and the Keck telescope that are located in the Canary Islands of Spain and Mauna Kea in Hawaii, respectively [3,4]. In these telescopes 36 hexagonal segments that are each about 1.8 m across are used to create an optical aperture of around 10 m in diameter.

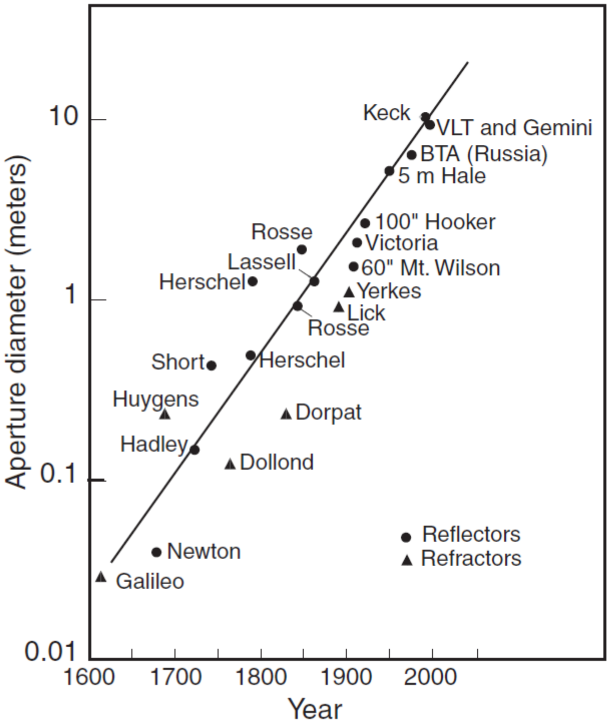

Figure 1-5.Evolution of telescope aperture diameter over last four centuries [2].

In the present thesis research, we have focused on the Thirty Meter Telescope (TMT). It is one of the most technically advanced, ground-based optical telescopes with a 30 m diameter primary mirror. It is scheduled to be built by 2018, in the proposed site of Mauna Kea, Hawaii. It will be equipped with 492 mirror segments, each with six edge sensors and three linear actuators that add up to a total of 2772 edge sensors and 1476 actuators [5]. A 3D rendering of the TMT is presented in Figure 1-6. Another prominent next generation telescope project, the European Extremely Large Telescope (E-ELT), is planned to have a 42 m diameter optical surface composed of 984 hexagonal segments that are to be controlled through 2952 actuators and 5604 edge sensors [6].

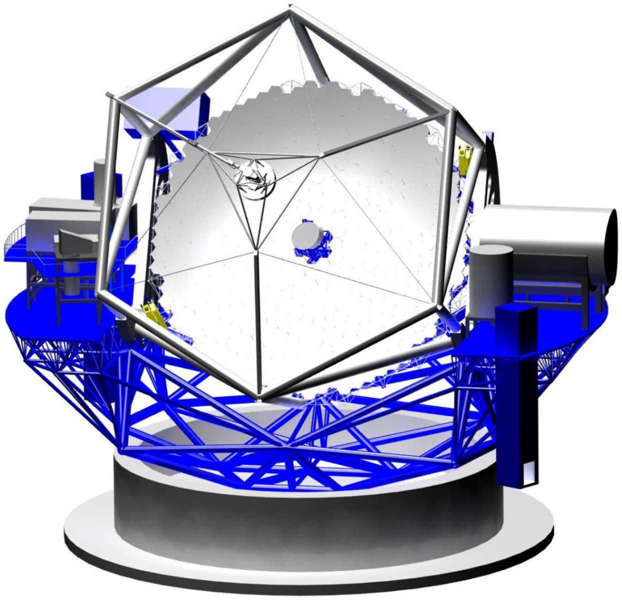

Figure 1-6.3D rendering of the Thirty Meter Telescope (TMT) under development [7].

The quality of an optical telescope is measured by the energy and the area of the image created on the image plane in the observation of the light emitted from a distant point in space. While traveling towards the telescope primary mirror, the light waveform gets distorted by the changes in the refractive index of the atmosphere, the diffractions at the edges of the optical elements on the path and the deviations from the initial design of the telescope (aberrations) creating the spreading of the energy on the image plane. The main aim of the telescope control is to correct the light waveform against disturbances (e.g. the errors in the design and manufacturing, gravity, deformations caused by the temperature changes, wind inside the telescope dome, seismic vibrations and vibrations caused by the operating machinery during the observations, atmospheric and thermal disturbances caused by the changes in the refractive index of the air…etc.). Table 1-1 summarizes the main sources of the disturbances during the observations.

Table 1-1. Disturbances degrading the image quality in the ground-based optical telescopes and their bandpasses [8].

Source of Error	Bandpass (Hz)
Optical Design	dc (fixed)
Optical manufacture	dc (fixed)
Theoretical errors of:	
-Mirror supports	dc to 10^{-3} (fixed to minutes)
-Structure	10^{-3} (minutes)
Maintenance errors of the structure and mirror supports	10^{-6} to 10^{-5} (days to hours)
Thermal distortions	
-Mirrors	10^{-5} to 10^{-4} (days to hours)
-Structure	10^{-3} (minutes)
Mechanical distortions of mirrors	10^{-7} (years)
Thermal effects of ambient air	10^{-4} to 10^{2} (hours to 0.01 sec)
Mirror deformation from wind gusts	10^{-2} to 10^{1} (minutes to 0.1 sec)
Atmospheric turbulence	2×10^{2} to 10^{3}+ (50 sec to < 10^{-3} sec)
Tracking error	5 to 10^{2} (0.2 sec to 0.01 sec)

The highest resolution image that can be obtained from an optical system is limited by diffraction. Diffraction occurs at the edges of opaque objects in the optical path of an imaging device. Every optical device suffers from the diffraction phenomenon and the resolution of an image that can be obtained is limited and depends on the geometric properties of the device and the properties of the light to be observed.

When a point source like a star in the sky is observed, on the image plane a central disk of light called Airy disk surrounded by fainter rings will be created. This pattern is known as Airy pattern and is named after George Biddell Airy who gave the full theoretical explanation of this pattern in his work "On the Diffraction of an Object-glass with Circular Aperture" in 1835 (see Figure 1-7). In a diffraction-limited system, the Airy disk contains the 84% of the energy collected by the telescope.

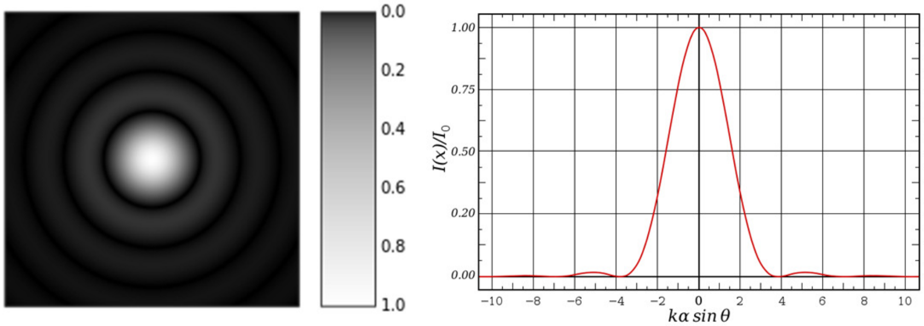

Figure 1-7.Airy Disk and its corresponding intensity graph [9].

In 1878, Lord Rayleigh stated that if the light waveform has a P-V error (i.e. the highest and lowest point on the light wave) of less than ¼ of the wavelength of the light observed, the optical system will not be significantly impaired. This value corresponds to the 1/8 wavelength of the optical surface error as any error on the optical surface will be doubled during the reflection of the light wave. To better describe this standard, rms criterion calculated for overall surface can be used. With the rms criterion, the ¼ of the wavelength of P-V criterion approximately corresponds to 1/14 of the wavelength (i.e. Marechal's approximation) for the rms criterion.

Table 1-2. Three optical quality measures of imaging devices and their corresponding values.

P-V value	**rms value**	**Strehl Ratio**
λ/4	λ /14	0.82
λ /8	λ /28	0.95
λ /10	λ/35	0.97

In this work, out of many optical quality measures, we concentrated on the Strehl ratio as it better describes the optical performance of telescopes compared to the others. The Sthrehl ratio is the ratio of the peak intensity of the observed Airy disk to the peak intensity of an error free optical system. The Strehl ratio of an optical device is defined in the range of 0 to 1 as 1 being a perfect optical device. The ¼ of the wavelength of P-V criterion approximately corresponds to a Strehl ratio of 0.82. Hence, usually an optical system with a Strehl ratio that is greater than 0.8 is considered as a perfectly operating imaging device [2]. Observations of a perfectly operating optical device are called diffraction-limited observations. Table 1-2 gives three different measures of the optical quality of imaging devices for three scenarios.

In optical telescopes, the light waveform reaching the image plane is generally corrected by using four levels of control. Although there may be some overlaps, these four levels of control usually have a good separation in spatial and temporal domains. Figure 1-8 presents these four levels of control on spatial and temporal axis.

The distortions caused by the atmospheric and thermal disturbances that cause changes in the refractive index of the air are indirectly corrected by using a deformable secondary mirror (M2). This type of control is called adaptive optics, and it was first mentioned in a paper published in 1953 by an astronomer named Horace Babcock at the Mount Wilson Observatory [10]. The technology at the time was not advanced enough for the application of this new idea. In the nineties, with the advances in computer technology, the application of the adaptive optics became easier making the diffraction-limited observation by the ground-based optical telescopes possible. Figure 1-9 presents the adaptive optics design and sample observations with and without adaptive optics.

The pointing of the telescope to a celestial body and tracking is achieved by using the main axes of the telescope structure. The alignment of the secondary mirror rigid body is controlled in another level of control.

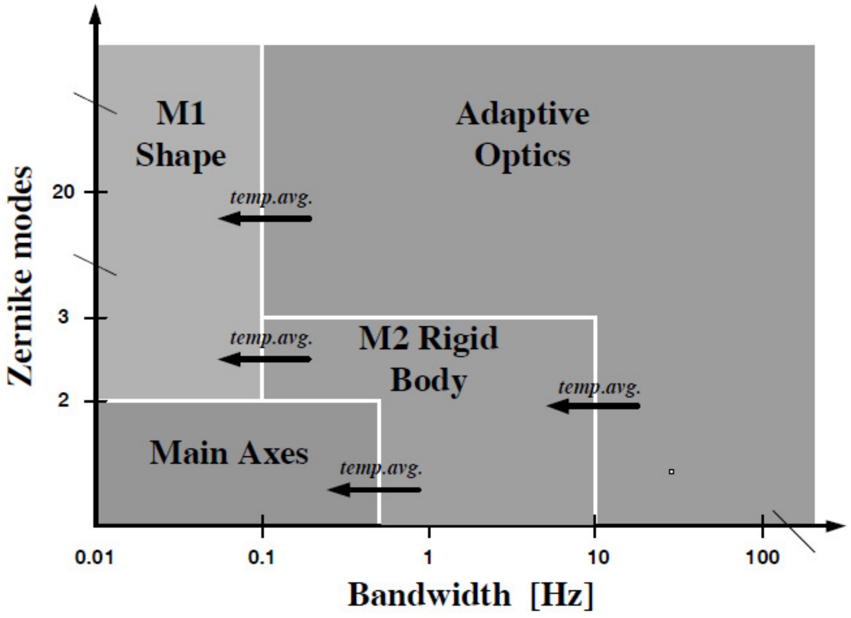

Figure 1-8. Four levels of telescope control [11].

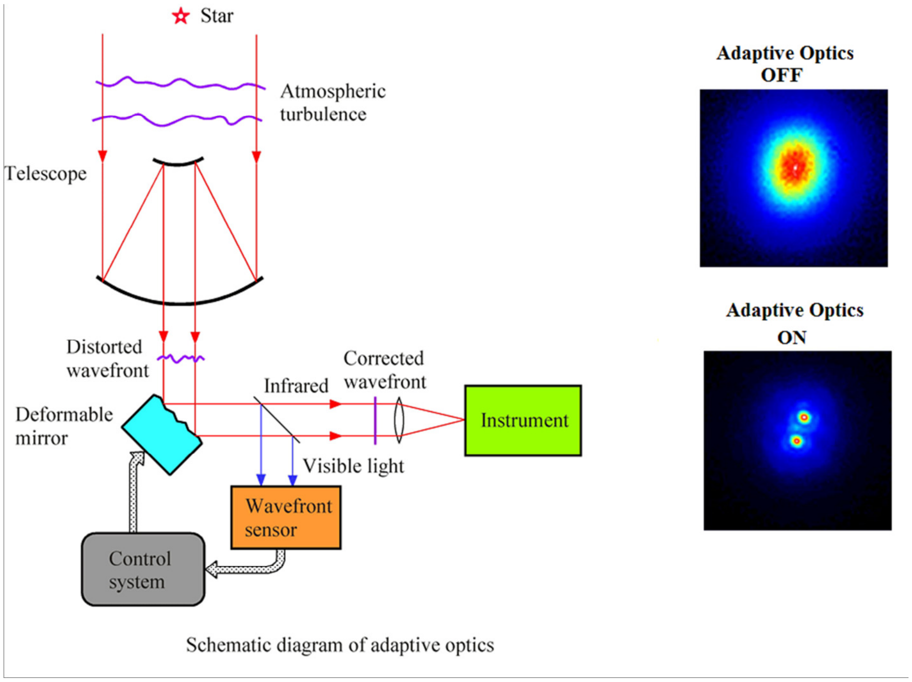

Figure 1-9. Adaptive optics [12, 13].

To maintain the shape and the continuity of the primary mirror (M1) against thermal, gravitational and wind disturbances, active optics is employed. In this dissertation, the active optics of the next generation telescopes is investigated. The main focus is the shape control problem of the primary mirrors of the next generation extremely large telescopes against the disturbances caused by the wind inside the telescope dome.

For the shape control of the primary mirrors of the optical telescopes with apertures greater than 2 meters diameter, passive means of control by relying on the intrinsic stiffness of the telescope structure is proven to be insufficient. For these telescopes, active control of the primary mirror shape is required for diffraction-limited observations [14].

In the Keck telescope, the shape control is achieved by using the pseudo-inverse of the Jacobian matrix A that relates the change in position actuators δp to change in the edge sensor readings δp [15]:

$$\delta s = A.\delta p \tag{1.1}$$

The matrix A is calculated analytically from the telescope design (together with recording the sensor readings while moving the actuators) and the pseudo-inverse B of matrix A is calculated to minimize the quadratic norm of the output error $||\delta s||_2$. The optimum values of the change in position of actuators δp^* to correct the shape of the mirror and the command sent to the actuators $\delta p_{applied}$ are calculated as follows:

$$\delta p^* = (A^T A)^{-1} A^T \delta\mathrm{s} = B.(s - s_d) \tag{1.2}$$

$$\delta p_{applied} = g \delta p^* \tag{1.3}$$

where s is the vector of sensor readings, s_d is the vector of desired sensor readings and g is the control system gain respectively. Although the bandwidth of the shape control is set to 0.5 Hz to avoid the control-structure interactions, some local segment structural modes around 25 Hz gets excited by the disturbances (e.g. wind) that are not accounted for [16]. With the introduction of extremely large telescopes, control issues have become a major concern in the design of these next generation telescopes.

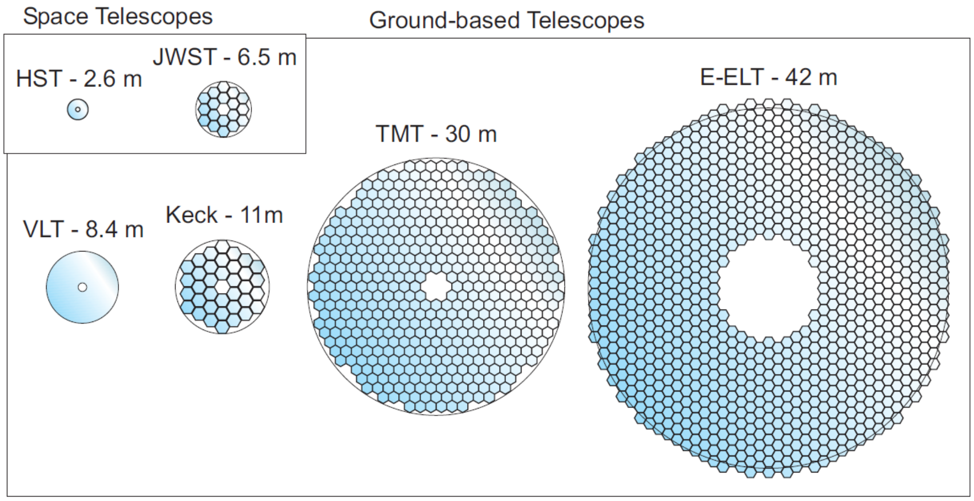

Figure 1-10. Primary mirrors of current and future optical telescopes [6].

Figure 1-10 shows some of the telescopes of current interest: the Very Large Telescope (VLT), the Keck Telescope, and the Hubble Space Telescope (HST); and the telescopes that are planned to be operational within a decade: the James Webb Space Telescope (JWST), the Thirty Meter Telescope (TMT), and the European Extremely Large Telescope (E-ELT). As it can be seen from Figure 1-10, a large leap in the size of telescopes is planned in near future. As the sizes of future telescopes increase in order to collect more light to see deeper into space, the control problem of stabilizing and aligning the vast number of segments has become a challenging task to address using classical centralized control techniques. Although with a centralized scheme, the control-structure interactions can easily be addressed in the synthesis of a controller, the vast number of control parameters requires a high capacity central computing unit with a high communication bandwidth to operate the closed-loop system [17]. With the implementation of a centralized scheme, a bottleneck in the system where all the information is collected, processed, and delivered is created which makes the system vulnerable to overall system outages as a result of controller crashes. On the other hand, the increase in the sensitivity of the support structure to the disturbances makes the decentralized techniques that cannot achieve cooperation among the neighbouring segment controllers to account for the structural coupling (i.e. dynamic coupling) and the objective coupling ineffective [6]. As the control bandwidth is increased to cope with the increased sensitivity of the support to disturbances, there is a need for a networked segment controller (i.e. distributed controller) architecture that enables controllers to co-operate toward a common goal of minimizing misalignments of segments. Subsequently, there is a need to take into account the control actions of neighbouring mirrors to address dynamic coupling. The gap between control bandwidth and the natural frequency of the existing telescopes allows current telescope control techniques to ignore the control structure interactions among segments [16]. Moreover, controllers employed by the existing telescopes also ignore the wind effect [16]. With the introduction of extremely large telescopes, wind effect that has a higher frequency content compared to the other sources of disturbances (such as thermal gradients and gravity) is believed to be the main source of disturbance that needs to be controlled in order to maintain a smooth mirror surface [18]. Although distributed controllers seem to be the best choice for the control of extremely large segmented mirrors in terms of the controller architecture, one should be careful about the effects of the noise propagation as a result of the spatial interconnections signals among neighbouring controllers. Figure 1-11 shows three control architectures that can be employed to control a system that is composed of interconnected subsystems.

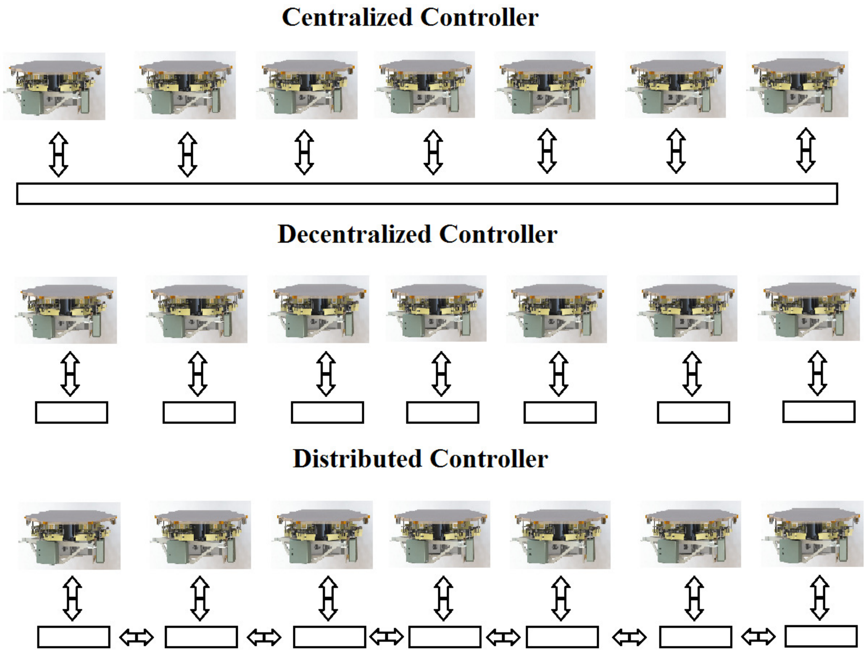

Centralized Controller

Decentralized Controller

Distributed Controller

Figure 1-11. Three control architectures.

All next generation telescope designs propose to use segmented mirrors to realize larger optical surfaces. Hexagonal segments connected in a honeycomb pattern will be employed in the two prominent next generation telescope projects E-ELT and TMT. Hexagonal segments in a honeycomb pattern can be considered as a spatially-invariant system and this aspect can be used in the design of distributed controllers. As a special case of a spatially-invariant system, actuation and sensing capabilities are lumped in spatial domain in segmented telescopes. There are many other systems that fall into this special category of spatially-discrete and spatially-invariant systems [19-22]. In these systems, system and control parameters can be indexed both spatially (i.e. in space) and temporarily (i.e. in time). For the segmented mirrors since the spatial variables are discrete, integers are used to represent segments where lumped actuation and sensing capabilities are located. Considering the sizes of the next generation telescopes, they can be assumed to be spatio-temporal systems [23] where dynamics and control variables are indexed with both temporal and spatial variables. The spatial invariance of the large segmented mirrors can be made use of in the synthesis of distributed controllers [24-26]. Spatial invariance enables one to define a single segment in a spatio-temporal state-space representation, and a distributed controller can be synthesized with the help of linear matrix inequalities (LMIs) [25]. In [24], a spatial frequency domain analysis of the spatio-temporal systems is investigated and a roadmap of designing distributed controllers with spatial approximations is presented. In [26], it is shown that if the system state-space matrices can be represented as a Kronecker product of matrices with pattern matrices that commute in multiplication, a distributed controller that have the same interconnection pattern as the plant can be synthesized.

In this dissertation, the application of the distributed H_∞ controller to the next generation telescopes is investigated. In order maintain the continuity of the optical surface against the higher frequency wind disturbance that will dominate the frequency and magnitude spectrum of the disturbances in the next generation telescopes, spatially-invariant distributed H_∞ controllers are designed via three existing methods in literature for three system models (dynamically decoupled model, dynamically coupled model and the finite element model of Thirty Meter Telescope). By connecting the neighbouring segment controllers, cooperation needed to align segments and minimize the interactions among segments is achieved.

An optical system working at its diffraction limit is called a diffraction-limited system. This limit can be calculated by taking into account the nature of the light to be observed and the geometry of the optical system. In order to get the best possible performance from an optical system, this limit can be set as the control objective, and any errors that can be bounded by this limit will not affect the quality of the captured image. In segmented mirrors, the root-mean-square (rms) value of the relative displacements (i.e. misalignments) at the segment edges are directly related to this limit and the error bounds for the control problem can be defined as the rms value of the relative displacements to operate the optical system in its best possible performance [27]. H_∞ approach allows us to specify this limit as the error bound of the synthesis, as H_∞ control deals with the rms gain from inputs to outputs of the closed-loop system [28]. By considering the expected wind blow and H_∞ approach, a diffraction-limited optical system that gives the best possible images in almost all wind conditions can be realized. In our work, the distributed H_∞ control approach with the frequency (i.e. Fourier), LMI-based and Decomposition-based synthesis with/without considering the control-structure interactions is chosen for its performance advantages in terms of stability margins and guaranteed image quality even in the worst-case closed-loop gain scenario. Also, H_∞ control allows us to define system uncertainties and set the robustness criteria accordingly that will be discussed during the controller synthesis for the TMT model. We tested these three different controllers with three system models that include the finite element model of the Thirty Meter Telescope. We also discussed possible system implementation for performance evaluation.

1.2 Objectives and contributions

The main objectives of this study are as follows:

- To perform a brief literature review to gain an understanding of the spatially invariant systems in the context of extremely large telescopes.
- To identify distributed control techniques that could be applied to the active optics of extremely large telescope mirrors.

- To design shape control strategies for extremely large telescope mirrors.
- To synthesize controllers for diffraction-limited observations even in the worst-case of closed-loop gain scenario, inherent model uncertainties and spatial variances.
- To test various types of distributed controllers with a system model that is as close as possible to the real Thirty Meter Telescope mirror.

1.2.1 Contributions

The main contributions of the thesis research are as follows:

- It is shown that the next generation extremely large telescope mirrors can be considered as spatially-invariant system and how the control problem can be made tractable with the use of distributed controllers is demonstrated.
- It is also shown that the small spatial variances among segments could be modelled as uncertainties and could be addressed during the controller synthesis.
- The application of the distributed H_∞ control synthesis problem with the main disturbance source (i.e. the wind disturbance) to the relative edge displacements (i.e. misalignments among segments) for diffraction-limited observations even in the worst-case closed-loop gain scenario is presented.
- The state-space representations compatible with the three distributed control methods have been derived from conventional dynamics of the extremely large telescope mirror model.
- The objective couplings among segments have been addressed via Decomposition-based distributed H_∞ control.
- The capabilities of the LMI-based distributed H_∞ control in addressing the objective and dynamic couplings, and small spatial variances among segments are presented.
- It is demonstrated that the Fourier-based distributed H_∞ control is able to address the objective and dynamic couplings using the spatial shift operators and the small spatial variances among segments could be considered in the robustness analysis.

1.3 Thesis Outline

In Chapter 2, three models (dynamically uncoupled, dynamically coupled and Thirty Meter Telescope models) used to test three distributed controller synthesis methods are presented. First, some information of the geometric properties of the segmented next generation extremely large telescope primary mirrors is given. Then for each model physical properties and calculations are provided.

In Chapters 3, 4 and 5, the summaries of the calculations for the three different methods (Fourier-based, LMI-based and Decomposition-based methods) to synthesize distributed H_∞ controllers are provided.

In Chapters 6 and 7, Fourier-based distributed H_∞ control of the 37-segment and Decomposition-based 492-segment (TMT-like) dynamically uncoupled systems are investigated, respectively. It is shown that Fourier-based and Decomposition-based methods can be applied to the control of segmented mirrors where structural deformation of the support is small enough to not put any restrictions to the quality of the images obtained from the optical system.

In Chapters 8 and 9, in addition to the objective coupling problems investigated in Chapters 6 and 7, structural coupling among segments are also addressed in the synthesis of Fourier-based distributed H_∞ control for a 7-segment dynamically coupled segmented primary mirror and LMI-based distributed H_∞ control for a 492-segment (TMT-like) dynamically coupled system models.

In Chapter 10, Fourier-based and LMI-based distributed H_∞ control techniques are used to synthesize controllers for the Thirty Meter Telescope finite element model provided by NRC-HIA. In this chapter in addition to the structural and objective couplings, it is shown that the small spatial variances caused by the aspheric nature of the telescope primary mirror can be modelled as uncertainties and a robust controller that will not destabilize the system as a result of uncertainties can be synthesized accordingly via the Fourier and LMI-based methods.

In Chapter 11, a possible system implementation for performance evaluation is investigated. A single segment setup is currently available at NRC-HIA. Specifications of the various components that are already obtained to build a single segment system are given. In this chapter, the preliminary study results of a candidate platform that can host the distributed controllers are also presented.

Finally in Chapter 12, the conclusions resulting from the current research are presented and possible future works and recommendations are put forward.

2. SEGMENTED MIRRORS

In this chapter, three segmented primary mirror models are discussed: the dynamically uncoupled segmented mirror, the dynamically coupled segmented mirror and TMT primary mirror. These have been used as test beds for the proposed distributed control techniques.

All proposed next generation telescope projects are planned to employ segmented mirrors in their primary mirror design. There are two main segmented mirror layouts reported in the literature: "petals" (also known as keystones) and "hexagons" [2] (see Figure 2-1). In two prominent next generation telescopes (TMT, E-ELT) hexagons are preferred over petals. Hexagonal design enables uniform support units and has uniform distribution of the active control elements that allows the design and implementation of spatially-invariant distributed controllers throughout the spatial domain of the primary mirror.

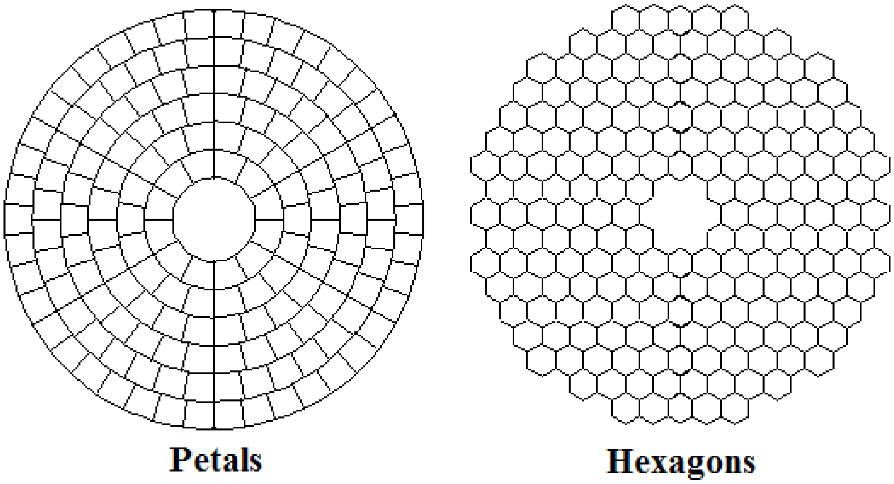

Figure 2-1. The two main segmented mirror geometries.

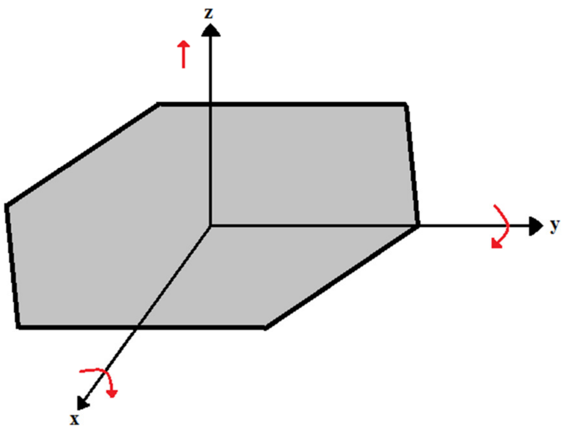

Three out-of-plane degrees of freedom

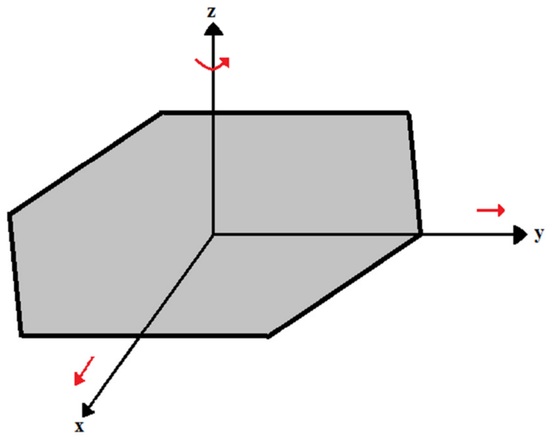

Three in-plane degrees of freedom

Figure 2-2. Segment degrees of freedom.

In the hexagonal design of the TMT primary mirror, each segment is supported by three actuators that can control three out-of-plane (tip and tilts) degrees of freedom of the segment body (see Figure 2-2). Three in-plane degrees of freedom are controlled passively by the placement of the segments to the support structure. These three in-plane degrees of freedom have negligible effect on the performance of the telescope and they are less sensitive to the disturbances acting on the primary mirror compared to the out-of-plane degrees of freedom [29]. In order to measure the misalignments at the segment edges, each segment is equipped with 6 edge sensors at 12 edge points. Figure 2-3 shows the locations of the sensing and actuation points of a segment. Figure 2-4 presents a candidate capacitive edge sensor design of TMT. In this design, at each sensing point an active or passive half of a capacitive sensor is located. By having two halves on the opposite side of an edge gap and by measuring the change of the capacitance, relative displacements between two sensing points located on two neighbouring segments can be measured. In order to operate the telescope in its diffraction-limit, the rms value of the misalignments at the segment edges should be smaller than a threshold value calculated according to the geometry of the telescope design and the properties of the light that is going to be observed.

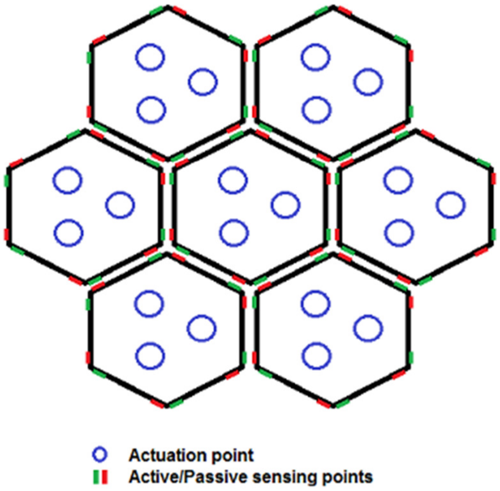

Figure 2-3. Geometric placements of sensors and actuators on the proposed TMT.

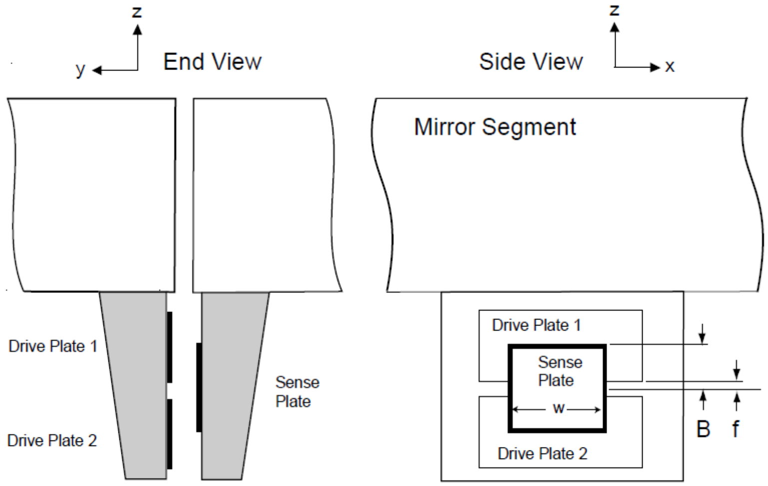

Figure 2-4. Capacitive edge sensor design with sense and drive plates [30].

In the hexagonal design of a segmented telescope mirror, each mirror segment can be considered as a unit that is spatially-invariant. In other words, moving forwards and backwards from one segment to the next in three spatial dimensions shown in Figure 2-5, system dynamics is assumed to not change. Considering S_1, S_2 and S_3 as the spatial shift operators, parameters of the neighbouring segments can be specified by using these spatial shift operators. In the case of the i^{th} segment, for example, in order to define the neighbouring segment's state vector x_j in the S_1 direction of i^{th} segment, the shift operator can be made use of as $x_j = S_1 x_i$.

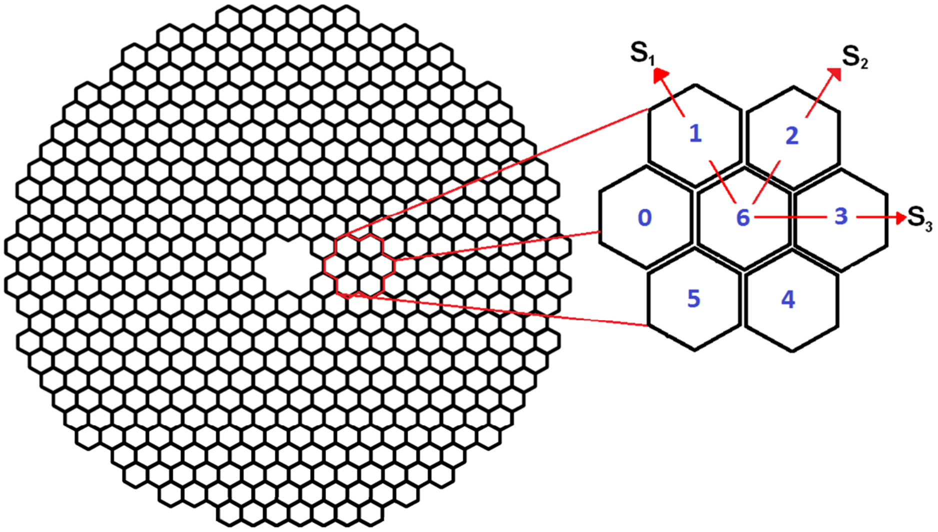

Figure 2-5. Spatial shift direction assignment for the TMT's segmented primary mirror.

2.1 Dynamically uncoupled model

A dynamically uncoupled system with the layout presented in Figure 2-3 and with parameters in Table 2-1 is modelled in [31]. In [31], a nodal model, i.e. a representation of localized masses mounted on springs and dampers, is adopted to tune natural frequencies and access the placement of nonlinearities to the model. A general nodal model with mass M, spring D and damping K coefficients is given below:

$$M\ddot{q} + D\dot{q} + Kq = B_w w + B_u u, \tag{2.1}$$

where q, $\dot{q}$, $\ddot{q}$ are the nodal displacements, nodal velocities and nodal accelerations, respectively. The control input u and the disturbance input w multiply the control B_u and the disturbance B_w matrices.

By assuming fixed support and modelling actuators as three springs with damping, a dynamically decoupled model can be obtained. The state-space representation of the i^{th} segment is given below:

$$\dot{x}_i = A_i x_i + B_{1i} w_i + B_{2i} u_i \tag{2.2}$$

where $x_i = [q_i^T \quad \dot{q}_i^T]^T$ is the state vector, and $A_i = \begin{bmatrix} 0 & I \\ -M_i^{-1}K_i & -M_i^{-1}D_i \end{bmatrix}, B_{1i} = \begin{bmatrix} 0 \\ M_i^{-1}B_{wi} \end{bmatrix}, B_{2i} = \begin{bmatrix} 0 \\ M_i^{-1}B_{ui} \end{bmatrix}.$

The state-space representation of a system with $n+1$ segments can be calculated by concatenation as follows:

$$\dot{x} = Ax + B_1 w + B_2 u, \tag{2.3}$$

where $A = \begin{bmatrix} A_0 & & \\ & \ddots & \\ & & A_n \end{bmatrix}, B_i = \begin{bmatrix} B_{i0} & & \\ & \ddots & \\ & & B_{in} \end{bmatrix} for\ i \in \{1, \quad 2\}$ and $x = \begin{bmatrix} x_0 \\ \vdots \\ x_n \end{bmatrix}$, $w = \begin{bmatrix} w_0 \\ \vdots \\ w_n \end{bmatrix}, u = \begin{bmatrix} u_0 \\ \vdots \\ u_n \end{bmatrix}.$

Table 2-1. Key geometric parameters of the segment model [31].

Parameter	**Symbol**	**Value**
Stiffness constant of the spring (N/m)	k	2.85×10^3
Damping coefficient of the spring (N/m/s)	α	1
Segment side length (m)	a	0.33
Mass of each segment (kg)	m	8.66
Density of each segment (kg/m^2)	ρ	30
Distance from the supporting point to the centre (m)	r	0.14
Distance from the sensing point to the nearest vertex (m)	g	0.055

For our control and simulation purposes, we assume, as in [31], that the sensor measurements are locally available at each segment and the direct displacements of three supporting points can be feedback to the controller by the following output equation:

$$y_i = C_i x_i + v_i \tag{2.4}$$

where $C = [I_3 \quad 0_3]$ and v is the measurement noise which is assumed to be comparable to the Keck's sensor noise level. The output equation for the state-space of $n+1$ segment can be obtained as follows:

$$y = Cx + v, \tag{2.5}$$

with $C = \begin{bmatrix} C_0 & & \\ & \ddots & \\ & & C_n \end{bmatrix}$ and $v = \begin{bmatrix} v_0 \\ \vdots \\ v_n \end{bmatrix}$.

2.2 Dynamically coupled model

In our simulation, for the dynamically coupled model we used the model designed in [32]. For the complete description, please refer to [32]. Here we will give a quick summary of the model used in our simulations.

2.2.1 Geometric design of support structure

As the hexagonal segments are placed further away from the main optical axis in the honeycomb pattern, their hexagonal shapes are distorted in order to obtain the aspheric curvature of the primary mirror. In this design, the mirror segments are defined in such a way that when they are projected to a plane whose normal vector is the optical axis, they appear as uniform hexagonal segments. The computer aided design (CAD) model and support structure of the 7-segment system are shown in Figures 2-6 and 2-7, respectively.

Following the steps previously outlined in [25, 33], first, three points are defined, which are named as the triad of the segment, on the surface of each segment. The triad of the segment is used to define the segment orientation plane and position with respect to the global coordinate system. By projecting these three points perpendicular to the orientation plane a new plane called top truss plane is obtained as shown by the shaded regions in Figure 2-8. The intersection point of the neighbouring three top truss planes then defines a top truss node. The top truss nodes define the geometry of the top truss surface of the segment support truss. In order to define the base truss surface, the line through top truss node whose points are equidistant from the adjacent top truss planes is calculated. The perpendicular planes to the calculated line are then defined as the base truss planes, shown in the shaded regions of Figure 2-9. The intersection point of the three neighbouring planes defines a base truss node. The three closest base truss nodes are then connected to the top truss node in a pyramid-like pattern via truss elements as shown in Figure 2-9. By connecting base truss and top truss nodes to their neighbours with the truss elements and with the pyramid structures defined a total support truss is obtained as shown in Fig. 2-10.

After defining the geometry of the support truss, actuators are needed to be placed to support the segments. Three linear actuators per segment are placed by inscribing a triangle in the top truss plane triangle shown in Figure 2-7. By rotating actuator triads about the centre of the top truss plane triangle, it is possible to optimize the separation of actuators relative to the centre of each segment. As described previously for the hexagonal segments, the actuator triads are also deformed from equilateral triangle as a function of radius from optical axis. To minimize this deformation, each actuator triad's dimension and orientation are optimized accordingly. The optimization helps to reduce the spatial variances in the structural dynamics and interconnections of each segment, since it is the base assumption for the application of the distributed control theories. Key geometric parameters of the system are given in Table 2-2.

2.2.2 Distributed segment modeling

In the distributed modelling of the 7-segment system defined in the previous section, the state-space framework for spatially-interconnected systems presented in [25, 33] is employed. In this modelling technique, the distributed model is obtained by spatially discretizing the structure into an array of spatially invariant interconnected systems. The spatial interconnection signals couple each discrete unit (i.e. each segment in our case) to the neighbouring units. The interconnection signals from one unit to the other results in disturbances flowing through the system. A disturbance affecting one unit ripples through the entire system via the interconnection signals and disturbs the other units as well. This signal flow through the system is one of the key motivators for the development of the distributed controller for highly segmented mirrors.

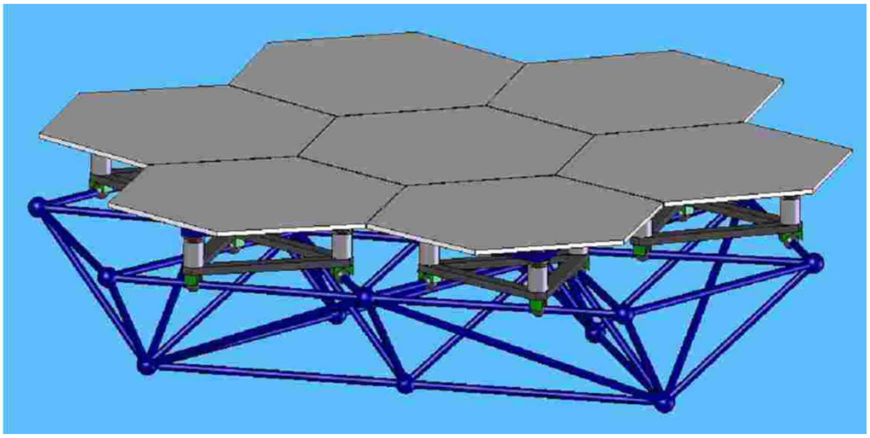

Figure 2-6. CAD model of 7-segment system.

The interconnection signals are defined along finite number of spatial dimensions. At each dimension, positive and negative directions with an input-output pair at each are defined to account for interactions among segments. By adding and removing units at each direction a large interconnected system can be obtained. In [25], the infinite extended systems are considered in the controller development. However, in [34], by converting the finite extended system to a ring-like system with special boundary conditions, the applicability of the distributed theory to the finite extended systems is proven.

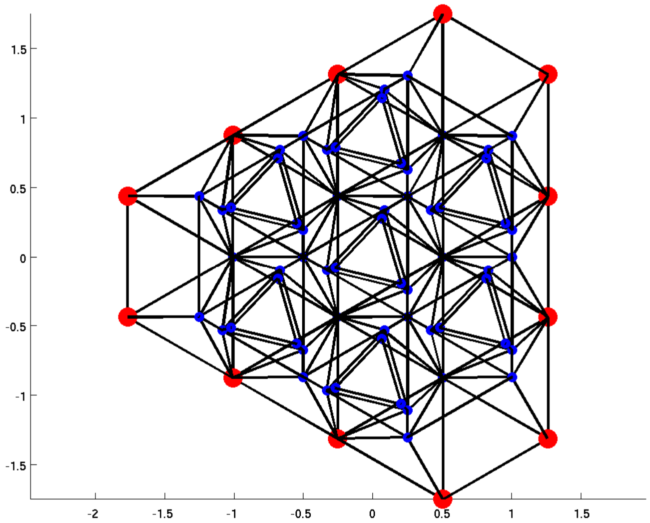

Figure 2-7. Support nodes and elements of 7-segment system.

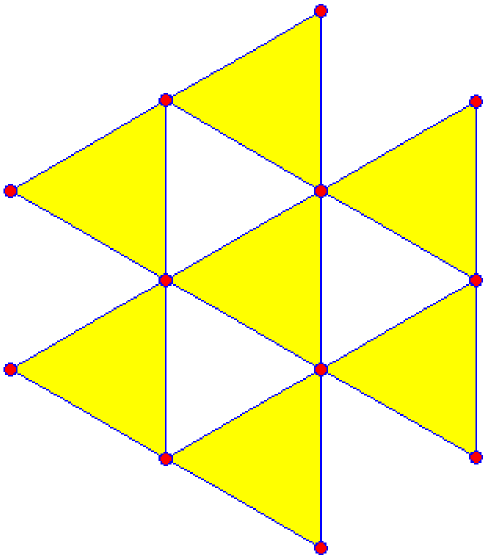

Figure 2-8. Top truss plane.

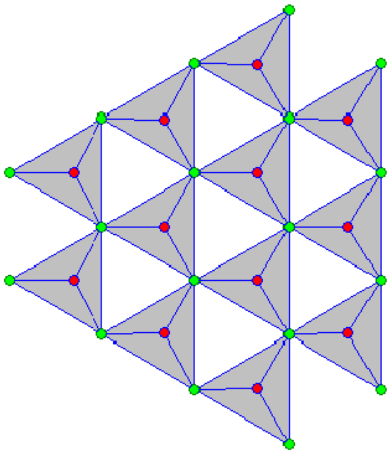

Figure 2-9. Base truss plane.

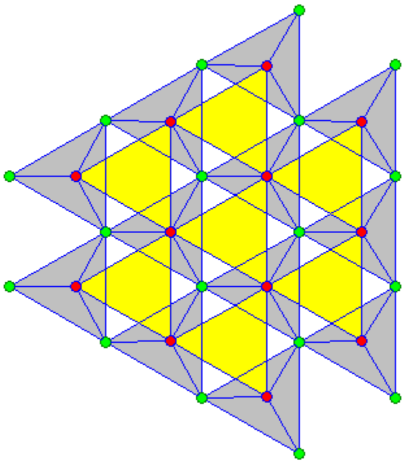

Figure 2-10. Overall truss plane.

Table 2-2. Key geometric parameters of the segment model.

Parameter	**Symbol**	**Value**
Radius of curvature (m)	R	60
Conical constant	K	0.9
Segment side length (m)	a	0.33
Pyramid truss height	h	0.4
Segment thickness	t	0.03
Distance from the supporting point to the centre (m)	r	0.14
Distance from the sensing point to the nearest vertex (m)	g	0.05

In our design, the obvious choice for the discrete units that are to be interconnected is the individual segments and their associated support structure below. In this scheme, since the segments and their support structure are distorted as a function of distance from the optical axis, the spatially-invariant condition is only approximately satisfied. However, as explained previously, these variations are minimized, and can merely be considered as an uncertainty in the distributed unit model. As a result of the hexagonal segmentation, each unit is surrounded by up to six other units that can be defined in three spatial dimensions. The outer segments are handled as a special case by considering [34] that addresses finite extended approximation of the infinite extended systems. Figure 2-11 shows a distributed representation of a single segment unit in three spatial dimensions and the 7-segment system which, in the case of the centre segment unit, is spatially interconnected through six directions.

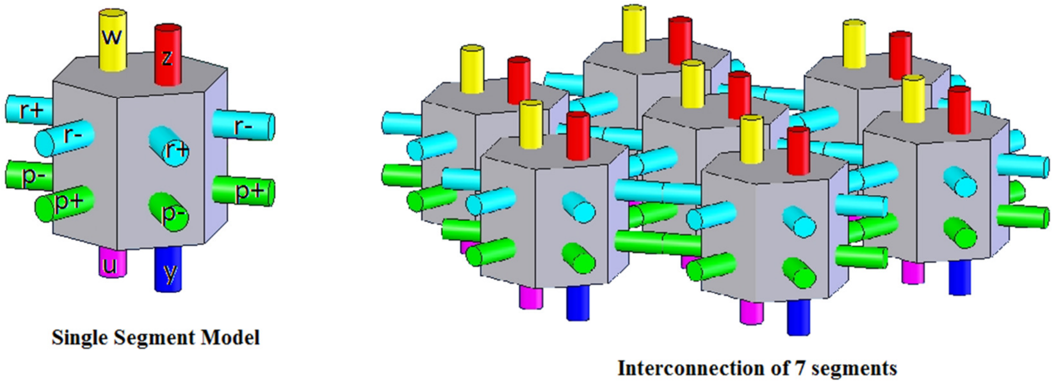

Single Segment Model

Interconnection of 7 segments

Figure 2-11. System representation and connections in three spatial dimensions.

The modified state-space of a distributed segment model is given by:

$$\begin{bmatrix} \dot{x}_i \\ r_i \\ y_i \end{bmatrix} = \begin{bmatrix} A_{TT} & A_{TS} & B_{Tw} & B_{Tu} \\ A_{ST} & A_{SS} & B_{Sw} & B_{Su} \\ C_T & C_S & D_w & D_u \end{bmatrix} \begin{bmatrix} x_i \\ p_i \\ w_i \\ u_i \end{bmatrix} \tag{2.6}$$

where the matrices A_{TT}, B_{T*}, C_T, D_* are the standard temporal-based state-space matrices, and the remaining matrices, denoted with an S subscript, are associated with the interconnections signals p_i and r_i. The subscript i denotes the i^{th} segment.

The modified state-space matrices A_{TT}, B_{T*}, C_T, D_* are obtained by using standard finite element method. Assuming each connection between nodes as a single cylindrical rod element and using lumped mass grid elements and proportional damping, a finite element model (FEM) of the designed support truss was previously obtained in [32]. For the sake of model simplification, actuators are modelled as a spring-damper system, acting along the line of actuator. The result of the FEM for the distributed segment unit in the augmented dynamic equation form is given by:

$$F = M\ddot{\delta} + D\dot{\delta} + K\delta + D_S\dot{\delta}_S + K_S\delta_S \tag{2.7}$$

where δ and δ_S are the coordinates of the local and interconnected nodal coordinates, respectively. M, D, and K are the standard mass, damping and stiffness matrices; and D_S and K_S are the interconnection damping and stiffness matrices (i.e. those of interconnecting grid element). For example, for an interconnecting element between a node on unit A and the other on neighbouring unit B, the interconnection stiffness matrix K_S in Eq. (2.7) can be partitioned as follows:

$$K_{AB} = \begin{bmatrix} K_{AA} & K_{AB} \\ K_{BA} & K_{BB} \end{bmatrix} \tag{2.8}$$

such that the static version of Eq. (2.7) for unit A becomes:

$$F = K_{AA}\delta_A + K_{AB}\delta_B = K_{AA}\delta + K_{AB}\delta_S \tag{2.9}$$

In Eq. (2.9), K_{AA} and K_{AB} matrices associated with the displacement vector of unit A and the neighbouring unit B (i.e. the interconnected signal) respectively can be assembled into K_S matrix. The remaining K_{BA} and K_{BB} matrices are ignored as they will be utilized in the counter case when unit B is modelled and unit A is considered as the neighbouring unit. The damping and mass matrices are also defined by using the same procedure.

The augmented dynamic equations in Eq. (2.7) can then be rewritten in the state-space form, i.e.

$$\begin{bmatrix} \dot{\delta} \\ \ddot{\delta} \end{bmatrix} = \begin{bmatrix} 0 & I \\ -M^{-1}K & -M^{-1}D \end{bmatrix} \begin{bmatrix} \delta \\ \dot{\delta} \end{bmatrix} + \begin{bmatrix} 0 & 0 \\ -M^{-1}K_S & -M^{-1}D_S \end{bmatrix} \begin{bmatrix} \delta_S \\ \dot{\delta}_S \end{bmatrix} + \begin{bmatrix} 0 \\ M^{-1} \end{bmatrix} F \tag{2.10}$$

in which $A_{TT} = \begin{bmatrix} 0 & I \\ -M^{-1}K & -M^{-1}D \end{bmatrix}, A_{TS} = \begin{bmatrix} 0 & I \\ -M^{-1}K & -M^{-1}D \end{bmatrix}, B_{T*} = \begin{bmatrix} 0 \\ M^{-1} \end{bmatrix}.$

In the above equations, A_{ST} is simply a permutation matrix since the output interconnection signals are a subset of the unit's state vector. Also with the same reasoning, A_{SS} and B_{S*} are equal to zero. The system output y of the distributed segment unit is the absolute positions of the actuator triad tied to the mirror segment called the actuation points. It is based off the unit's state variables resulting in C_T as permutation matrix while C_S and D_S are zero.

By using the above formulation, a spatially interconnected system with distributed segment units can be obtained. This model would be equivalent with the exception of order to the model produced by a FEM of the entire system without performing spatial discretization. The exception of the order is a result of the sharing of some nodes among the neighbouring units in the augmented model.

2.3 TMT finite element model

The finite element model of the TMT has been provided by NRC-HIA. Figure 2-12 shows the finite element model of the TMT. In this model, mirrors are modelled as triangular beams as the thickness to size ratio of the mirrors results in segment deformations that are negligible.

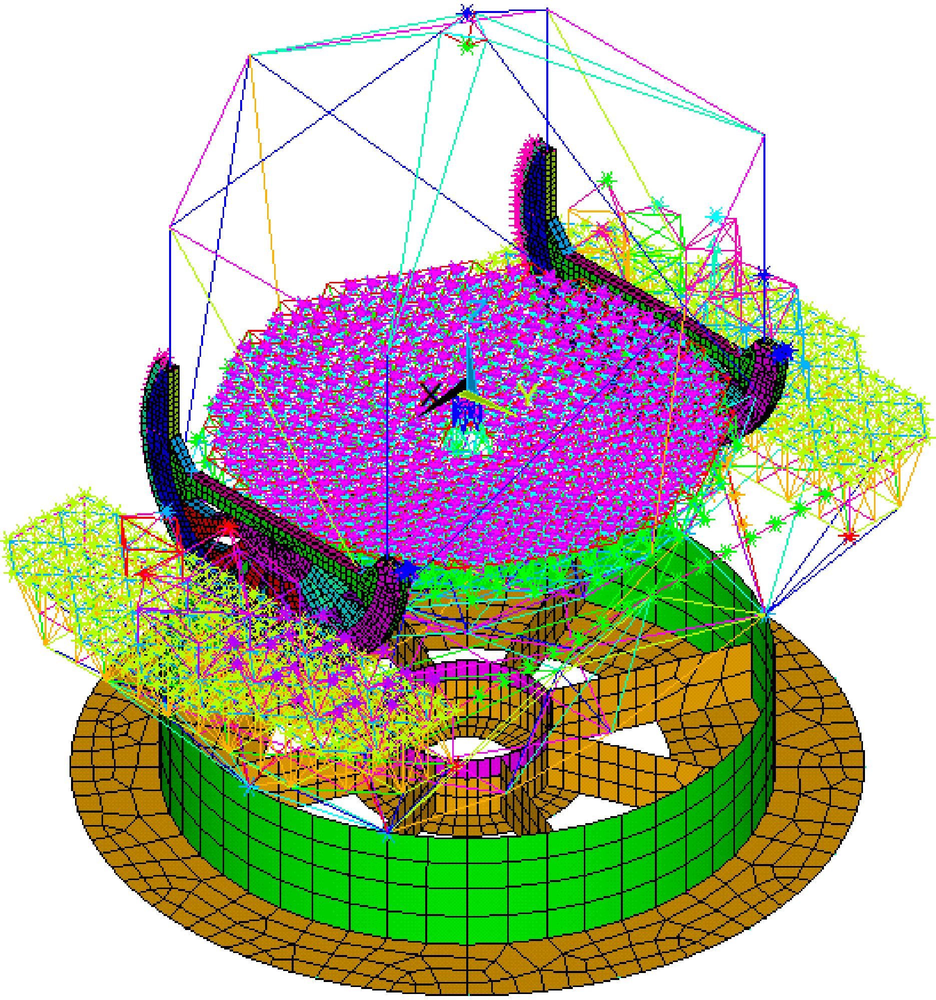

Figure 2-12. Finite element model of TMT.

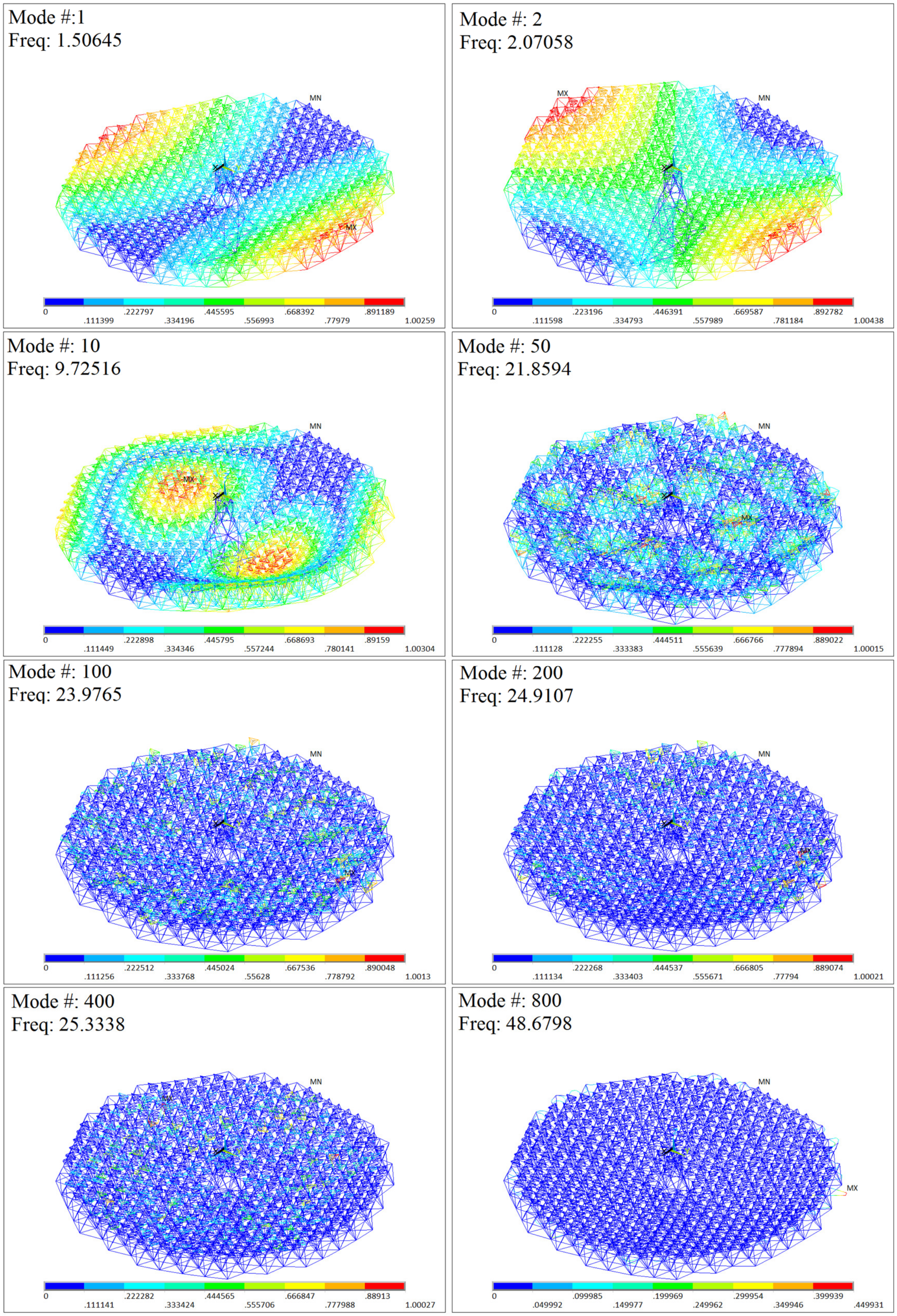

Figure 2-13. Sample modes of the primary mirror of the TMT.

Before the analysis, the primary mirror structure is separated from the overall TMT structure since the active control problem that we have been studying focuses on the problem of maintaining the continuity of the primary mirror surface. Other levels of telescope control address the problems of pointing the telescope to the celestial objects and tracking. On this separated primary mirror that is fixed at the elevation bearings on two sides, modal analysis has been carried out by the help of ANSYS software.

Figure 2-13 shows the sample modes of the primary mirror. In Figure 2-14, frequencies of first 750 structural modes are presented. As can be seen lower frequency modes correspond to the global structural modes and as frequency is increased local modes start to show up. Although the local mode frequency that corresponds to the single segment dynamics matches to the Keck telescopes single segment resonant frequency of 25 Hz, first global structural mode frequency drops from Keck’s 5.39 Hz to 1.5 Hz as expected [16]. Last modes correspond to the torsional modes which don’t have much effect on the continuity of the mirror surface and are controlled passively by the placement of segments to the support structure.

After the modal analysis, singular value plots of individual segments from three actuator force inputs to the three output actuator tip point positions have been investigated. The segment that has the highest input-output gain is taken as the nominal segment model. Since the highest input-output gain segment model is used in the synthesis by considering 100% multiplicative uncertainty, the closed-loop robustness could be guaranteed. The state-space model from three actuator force inputs of the highest input-output gain segment and eighteen actuator force inputs of the neighbouring six segments to the positions of the three actuator tip points is calculated. This twenty one input three output state-space model of the i^{th} segment can be represented as follows:

$$\dot{x}_i = Ax_i + B_F f_i \tag{2.11}$$

$$y_i = Cx_i \tag{2.12}$$

where $f_i \in R^{21}$, $y_i \in R^3$ are the input and output vectors respectively. This state-space model will be used as a spatially-invariant model in our controller synthesis and small variances will be addressed by adding the robustness criteria during the synthesis.

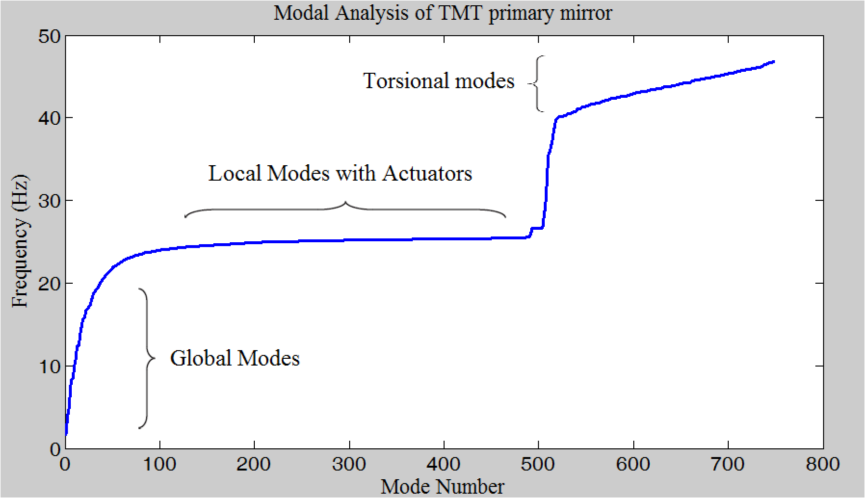

Figure 2-14. Mode number versus frequencies of TMT primary mirror.

3. FOURIER-BASED DISTRIBUTED CONTROL SYNTHESIS

In this chapter, Fourier-based distributed control will be discussed. In [24], a spatial frequency domain analysis of the spatio-temporal systems is investigated and a roadmap of designing distributed controllers with spatial approximations is presented. We will give the summary of the theory published in [24]. For complete discussions and proofs, please refer to [24].

In order to synthesize a distributed controller, we first need to discuss the synthesis of a generic H_∞ controller. Generic H_∞ control techniques assume unity signals and aims to calculate a feasible controller that will make the closed-loop system input-output H_∞ gain less than one. Figure 3-1 shows the closed-loop system with the plant G and the controller K that generic algorithm assumes. In this representation, w is the input disturbance, u is the control signal, y is the sensor output of the plant, and z is the output signal to be minimized. For a plant G generic H_∞ control algorithm calculates a controller K that will make closed-loop H_∞ gain from w to z less than one (i.e. $\|T_{wz}\|_\infty < 1$).

3.1 H_∞ controller synthesis

In our approach, the procedure presented in [28] is followed.

Let the state-space representation of the closed-loop system is given by:

$$\dot{x} = Ax + B_1 w + B_2 u, \tag{3.1}$$

$$z = C_1 x + D_{11} w + D_{12} u, \tag{3.2}$$

$$y = C_2 x + D_{21} w, \tag{3.3}$$

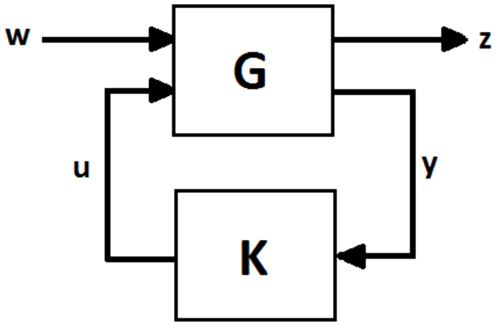

Figure 3-1. Closed-loop system representation for a generic H∞ synthesis algorithm.

where $x \in R^n$ is the state vector, $w \in R^{m_1}$ is the disturbance input vector, $u \in R^{m_2}$ is the control input vector, $z \in R^{p_1}$ is the output(error) vector, and $z \in R^{p_2}$ is the sensor (measurement) vector. Following matrices will be used later in the synthesis:

$$R_n = D_{1*}^T D_{1*} - \begin{bmatrix} I_{m_1} & 0 \\ 0 & 0 \end{bmatrix}, \tag{3.4}$$

$$\tilde{R}_n = D_{*1} D_{*1}^T - \begin{bmatrix} I_{p_1} & 0 \\ 0 & 0 \end{bmatrix}, \tag{3.5}$$

where $D_{1*} = [D_{11} \quad D_{12}]$ and $D_{*1} = \begin{bmatrix} D_{11} \\ D_{21} \end{bmatrix}$.

Now we can define the following two Hamiltonian matrices $\boldsymbol{H}$ and $\boldsymbol{J}$:

$$\boldsymbol{H} = \begin{bmatrix} A & 0 \\ -C_1^T C_1 & -A^T \end{bmatrix} - \begin{bmatrix} B \\ -C_1^T D_{1*} \end{bmatrix} R_n^{-1} [D_{1*}^T C_1 \quad B^T], \tag{3.6}$$

$$\boldsymbol{J} = \begin{bmatrix} A^T & 0 \\ -B_1 B_1^T & -A \end{bmatrix} - \begin{bmatrix} C^T \\ -B_1^T D_{*1}^T \end{bmatrix} \tilde{R}_n^{-1} [D_{*1} B_1^T \quad B^T] \tag{3.7}$$

Assume X and Y as the solutions to the following Algebraic Ricatti Equations (AREs):

$$X = Ric(\boldsymbol{H}), \tag{3.8}$$

$$Y = Ric(\boldsymbol{J}). \tag{3.9}$$

Then, we can calculate the state-feedback matrix F and the observer-gain matrix L as follows:

$$F = -R_n^{-1}(D_{1*}^T C_1 - B^T X) = \begin{bmatrix} F_1 \\ F_2 \end{bmatrix} = \begin{bmatrix} F_{11} \\ F_{12} \\ F_2 \end{bmatrix}, \tag{3.10}$$

$$L = -(B_1 D_{*1}^T + YC^T)\tilde{R}_n^{-1} = [L_1 \quad L_2] = [L_{11} \quad L_{12} \quad L_{22}], \tag{3.11}$$

where $F_1 \in R^{m_1}$, $F_2 \in R^{m_2}$, $F_{11} \in R^{(m_1-p_2)}$, $F_{12} \in R^{p_2}$, and $L_1^T \in R^{p_1}$, $L_2^T \in R^{p_2}$, $L_{11}^T \in R^{(p_1-m_2)}$, $L_{12}^T \in R^{m_2}$.

In the synthesis, the following assumptions are made:

1. (A, B_2) is stabilizable and (C_2, A) is detectable.
2. $D_{12} = \begin{bmatrix} 0 \\ I_{m_2} \end{bmatrix}$ and $D_{21} = [0 \quad I_{p_2}]$,
3. $\begin{bmatrix} A - jwI & B_2 \\ C_1 & D_{12} \end{bmatrix}$ has full column rank for all w,
4. $\begin{bmatrix} A - jwI & B_1 \\ C_2 & D_{21} \end{bmatrix}$ has full row rank for all w.

Now partition D_{11} into $D_{11} = \begin{bmatrix} D_{1111} & D_{1112} \\ D_{1121} & D_{1122} \end{bmatrix}$, where $D_{1122} \in R^{m_2 \times p_2}$.

There exists a stabilizing controller K that satisfies $\|T_{wz}\|_\infty < 1$, if and only if

- $\max(\bar{\sigma}[D_{1111} \quad D_{1112}], \bar{\sigma}[D_{1111}^T \quad D_{1112}^T]) < 1$,
- $\rho(XY) < 1$,

where $\rho(.)$ denotes the special radius.

If all the conditions above are satisfied, the state-space equations of a H_∞ controller are given by the following equations.

Define,

$$\widehat{D}_{11} = -D_{1121} D_{1111}^T (I - D_{1111} D_{1111}^T)^{-1} D_{1112} - D_{1122}, \tag{3.12}$$

$\widehat{D}_{12} \in R^{m_2 \times m_2}$ and $\widehat{D}_{21} \in R^{p_2 \times p_2}$ are any matrices that satisfy

$$\widehat{D}_{12}\widehat{D}_{12}^T = I - D_{1121}(I - D_{1111}^T D_{1111})^{-1} D_{1112}^T, \tag{3.13}$$

$$\widehat{D}_{21}^T\widehat{D}_{21} = I - D_{1112}(I - D_{1111} D_{1111}^T)^{-1} D_{1112}, \tag{3.14}$$

and

$$\widehat{B}_2 = Z(B_2 + L_{12})\widehat{D}_{12}, \tag{3.15}$$

$$\hat{C}_2 = -\widehat{D}_{12}(C_2 + F_{12}), \tag{3.16}$$

$$\widehat{B}_1 = -ZL_2 + \widehat{B}_2\widehat{D}_{12}^{-1}\widehat{D}_{11}, \tag{3.17}$$

$$\hat{C}_1 = F_2 + \widehat{D}_{11}\widehat{D}_{12}^{-1}\widehat{D}_{11}, \tag{3.18}$$

$$\hat{A} = A + BF + \widehat{B}_1\widehat{D}_{21}^{-1}\hat{C}_2, \tag{3.19}$$

where $Z = (I - YX)^{-1}$.

A H∞ controller satisfying $\|T_{wz}\|_\infty < 1$ can be represented as follows:

$$\dot{x} = \hat{A}x + \widehat{B}_1 y, \tag{3.20}$$

$$u = \hat{C}_1 x + \widehat{D}_{11} y. \tag{3.21}$$

3.2 Distributed H∞ controller synthesis

After describing the steps of generic H∞ controller synthesis via algebraic Riccati equations (AREs), in this section we will discuss the synthesis of distributed H∞ controller using Fourier transform. Let's assume the state-space representation of the i^{th} spatially-invariant segment is as follows:

$$\dot{x}_i = A_i x_i + B_{1_i} w_i + B_{2_i} u_i, \tag{3.22}$$

$$z_i = C_{1_i} x_i + D_{11_i} w_i + D_{12_i} u_i, \tag{3.23}$$

$$y_i = C_{2_i} x_i + D_{21_i} w_i, \tag{3.24}$$

The state-space matrices may contain spatial shift operators which carry information of the neighbouring segments and model the dynamic and objective couplings. By following the steps described in [24], we can synthesize a distributed H$_\infty$ controller.

As a first step we can take the Fourier transform of the state-space equations in order to decouple the shift operators:

$$\frac{\partial}{\partial t}\breve{x}_i = \breve{A}_i\breve{x}_i + \breve{B}_{1_i}\breve{w}_i + \breve{B}_{2_i}\breve{u}_i, \tag{3.25}$$

$$\breve{z}_i = \breve{C}_{1_i}\breve{x}_i + \breve{D}_{11_i}\breve{w}_i + \breve{D}_{12_i}\breve{u}_i, \tag{3.26}$$

$$\breve{y}_i = \breve{C}_{2_i}\breve{x}_i + \breve{D}_{21_i}\breve{w}_i. \tag{3.27}$$

After decoupling the shift operators from signals, we can design a H_∞controller in the Fourier domain and by calculating the inverse Fourier transform a controller in time domain can be calculated. However, taking the inverse is not trivial and the controller in time domain possibly will include infinite degree in shift operators. By taking into account the fact (given in [24]) that convolution kernels have exponential rates of decays, we can approximate a controller in time domain by using finite shift operators. If just the first neighbouring segments are considered, the state-space representation of a controller will be in the following form:

$$\begin{aligned} A_K(S) = A_{K0} + A_{K1}S_1 + A_{K2}S_2 + A_{K3}S_3 + A_{K4}S_1^{-1} \\ + A_{K5}S_2^{-1} + A_{K6}S_3^{-1}, \end{aligned} \tag{3.28}$$

$$\begin{aligned} B_K(S) = B_{K0} + B_{K1}S_1 + B_{K2}S_2 + B_{K3}S_3 + B_{K4}S_1^{-1} \\ + B_{K5}S_2^{-1} + B_{K6}S_3^{-1}, \end{aligned} \tag{3.29}$$

$$\begin{aligned} C_K(S) = C_{K0} + C_{K1}S_1 + C_{K2}S_2 + C_{K3}S_3 + C_{K4}S_1^{-1} + C_{K5}S_2^{-1} \\ + C_{K6}S_3^{-1}, \end{aligned} \tag{3.30}$$

$$\begin{aligned} D_K(S) = D_{K0} + D_{K1}S_1 + D_{K2}S_2 + D_{K3}S_3 + D_{K4}S_1^{-1} \\ + D_{K5}S_2^{-1} + D_{K6}S_3^{-1}. \end{aligned} \tag{3.31}$$

By following the procedure described in the previous section, H$_\infty$ controllers in Fourier domain at some gridding points can be synthesized. The matrices given in Eq.s (3.28)-

(3.31) can be estimated by using the Least Squares Estimation (LSE). Since we have three spatial directions, an example m^{th} gridding point can be defined as $(\theta_{1m} \quad \theta_{2m} \quad \theta_{3m})$. At his particular point, the state-space matrices in Eq.s (3.28)-(3.31) in Fourier domain can be represented as follows:

$$\begin{aligned} A_{K_m} = {} & A_{K0} + A_{K1} I_n e^{j\theta_{1m}} + A_{K2} I_n e^{j\theta_{2m}} + A_{K3} I_n e^{j\theta_{3m}} + A_{K4} I_n e^{-j\theta_{1m}} \\ & + A_{K5} I_n e^{-j\theta_{2m}} + A_{K6} I_n e^{-j\theta_{3m}}, \end{aligned} \tag{3.32}$$

$$\begin{aligned} B_{K_m} = {} & B_{K0} + B_{K1} I_n e^{j\theta_{1m}} + B_{K2} I_n e^{j\theta_{2m}} + B_{K3} I_n e^{j\theta_{3m}} + B_{K4} I_n e^{-j\theta_{1m}} \\ & + B_{K5} I_n e^{-j\theta_{2m}} + B_{K6} I_n e^{-j\theta_{3m}}, \end{aligned} \tag{3.33}$$

$$\begin{aligned} C_{K_m} = {} & C_{K0} + C_{K1} I_n e^{j\theta_{1m}} + C_{K2} I_n e^{j\theta_{2m}} + C_{K3} I_n e^{j\theta_{3m}} + C_{K4} I_n e^{-j\theta_{1m}} \\ & + C_{K5} I_n e^{-j\theta_{2m}} + C_{K6} I_n e^{-j\theta_{3m}} \end{aligned} \tag{3.34}$$

$$\begin{aligned} D_{K_m} = {} & D_{K0} + D_{K1} I_n e^{j\theta_{1m}} + D_{K2} I_n e^{j\theta_{2m}} + D_{K3} I_n e^{j\theta_{3m}} + D_{K4} I_n e^{-j\theta_{1m}} \\ & + D_{K5} I_n e^{-j\theta_{2m}} + D_{K6} I_n e^{-j\theta_{3m}}. \end{aligned} \tag{3.35}$$

After calculating H_∞ controllers at enough gridding points the matrices in Eq.s (3.28)-(3.31) can be estimated by using the LSE. As a result of our synthesis, we will have a controller in the following form:

$$\begin{aligned} \dot{x}_{K_i} = {} & (A_{K0} + A_{K1} S_1 + A_{K2} S_2 + A_{K3} S_3 + A_{K4} S_1^{-1} + A_{K5} S_2^{-1} \\ & + A_{K6} S_3^{-1}) x_{K_i} \\ & + (B_{K0} + B_{K1} S_1 + B_{K2} S_2 + B_{K3} S_3 + B_{K4} S_1^{-1} + B_{K5} S_2^{-1} \\ & + B_{K6} S_3^{-1}) y_i, \end{aligned} \tag{3.36}$$

$$\begin{aligned} \dot{x}_{K_i} = {} & (C_{K0} + C_{K1} S_1 + C_{K2} S_2 + C_{K3} S_3 + C_{K4} S_1^{-1} + C_{K5} S_2^{-1} \\ & + C_{K6} S_3^{-1}) x_{K_i} \\ & + (D_{K0} + D_{K1} S_1 + D_{K2} S_2 + D_{K3} S_3 + D_{K4} S_1^{-1} + D_{K5} S_2^{-1} \\ & + D_{K6} S_3^{-1}) y_i. \end{aligned} \tag{3.37}$$

From the above form, it can be seen that the controller does not only use its sensor signal and states but also takes into account the neighbouring segment controller sensor signal and states in order to calculate its actuation signals (i.e. control input).

4. LMI-BASED DISTRIBUTED CONTROL SYNTHESIS

In this chapter, the synthesis of a distributed controller by using Linear Matrix Inequalities (LMIs) is presented. In the following, we will give the summary of the procedure described in [25] and show how a distributed H_∞ controller can be calculated by using the modified state-space matrices. Just like the generic H_∞ controller synthesis, the synthesized controller will satisfy the closed-loop H_∞ gain bound 1. In other words, the resultant closed-loop system will have a H_∞ gain from input disturbance w to the output error z less than 1 (i.e. $\|T_{wz}\|_\infty < 1$) (see Figure 4-1). For the complete description and proofs please refer to [25].

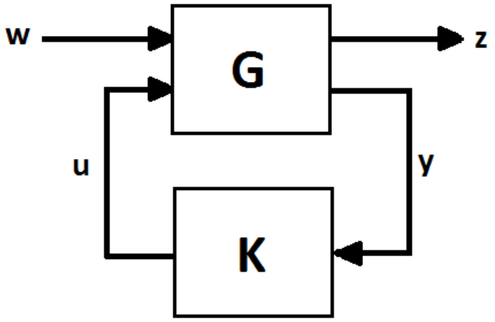

Figure 4-1. Closed-loop system representation for a generic H_∞ synthesis algorithm.

As described in [25], the modified state-space of the spatially-invariant plant is given as follows:

$$\begin{bmatrix} \dot{x}_i \\ r_i \\ z_i \\ y_i \end{bmatrix} = \begin{bmatrix} A_{TT} & A_{TS} & B_{Tw} & B_{Tu} \\ A_{ST} & A_{SS} & B_{Sw} & B_{Su} \\ C_{zT} & C_{zS} & D_{zw} & D_{zu} \\ C_{yT} & C_{yS} & D_{yw} & D_{yu} \end{bmatrix} \begin{bmatrix} x_i \\ p_i \\ w_i \\ u_i \end{bmatrix} \tag{4.1}$$

where the matrices A_{TT}, B_{T*}, C_T, D_* are the standard temporal-based state-space matrices, and the remaining matrices, denoted with an S subscript, are associated with the interconnection signals p_i and r_i. The subscript i denotes the i^{th} segment.

As a first step, in order to make the spatial-domain compatible to the time domain approach, a bilinear-like transformation (f_{D2C} transformation) is applied to the spatial domain. Asssuming $(I - A_{SS})^{-1}$ exists, define a matrix H as:

$$H = \begin{bmatrix} I_{m_1} & 0 & \cdots & 0 \\ 0 & -I_{m_1} & \cdots & 0 \\ \vdots & & \ddots & \\ 0 & \dots & 0 & -I_{m_{-L}} \end{bmatrix} \tag{4.2}$$

where m_* and m_{-*} are the size of connection signal in spatial directions S_* and S_*^{-1}.

Define $\mathrm{m} = (\mathrm{m}_0, \mathrm{m}_1, \mathrm{m}_{-1}, \cdots, \mathrm{m}_\mathrm{L}, \mathrm{m}_{-\mathrm{L}})$ as the set of all m_* . Next, define

$$A = \begin{bmatrix} A_{TT} & A_{TS} \\ A_{ST} & A_{SS} \end{bmatrix}, B = \begin{bmatrix} B_{Td} & B_{Tu} \\ B_{Sd} & B_{Su} \end{bmatrix}, C = \begin{bmatrix} C_{zT} & C_{zS} \\ C_{yT} & C_{yS} \end{bmatrix}, D = \begin{bmatrix} D_{zd} & D_{zu} \\ D_{yd} & D_{yu} \end{bmatrix} \tag{4.3}$$

Now define the f_{D2C} transform of system M where $M = \{A, B, C, D, m\}$, as:

$$f_{D2C}(M) = \bar{M} = \{\bar{A}, \bar{B}, \bar{C}, \bar{D}, \bar{m}\}, \tag{4.4}$$

$$\bar{m} = (m_0, m_1 + m_{-1}, 0, \cdots, m_L + m_{-L}, 0), \tag{4.5}$$

$$\bar{A}_{SS} = -(I + A_{SS})(I - A_{SS})^{-1}H, \tag{4.6}$$

$$[\bar{A}_{ST} \quad \bar{B}_S] = \sqrt{2}(I - A_{SS})^{-1}[A_{ST} \quad B_S], \tag{4.7}$$

$$\begin{bmatrix} \bar{A}_{TS} \\ \bar{C}_S \end{bmatrix} = -\sqrt{2}\begin{bmatrix} A_{TS} \\ C_S \end{bmatrix}(I - A_{SS})^{-1}H \tag{4.8}$$

$$\begin{bmatrix} \bar{A}_{TT} & \bar{B}_T \\ \bar{C}_T & \bar{D} \end{bmatrix} = \begin{bmatrix} A_{TT} & B_T \\ C_T & D \end{bmatrix} + \begin{bmatrix} A_{TS} \\ C_S \end{bmatrix}(I - A_{SS})^{-1}[A_{ST} \quad B_S] \tag{4.9}$$

and $C_T = [C_{zT} \quad C_{yT}]^T$, $C_S = [C_{zS} \quad C_{yS}]^T$, $B_T = [B_{Tw} \quad B_{Tu}]$, $B_S = [B_{Sw} \quad B_{Su}]$, $D = [D_w \quad D_u]$, $D_w = [D_{zw} \quad D_{yw}]^T$, *and* $D_u = [D_{zu} \quad D_{yu}]^T$.

To be able to synthesize a distributed H_∞ controller, the feasibility condition needs to be checked. Linear matrix inequality algorithm searches for matrices which satisfy the feasibility conditions that are set as linear matrix inequalities. These matrices are later used in the calculation of the controller state-space matrices. In the following, the superscripts G, C, and K denote the open-loop system, closed-loop system and controller, respectively. For the transformed system, there exist a controller satisfying well-posedness, stability and performance conditions if and only if there exist X^G and Y^G such that the three LMIs shown below are satisfied:

$$\begin{bmatrix} N_Y & 0 \\ 0 & I \end{bmatrix}^T \begin{bmatrix} \begin{bmatrix} \bar{A}^G Y^G + Y^G (\bar{A}^G)^T & Y^G (\bar{C}^G_{z*})^T \\ \bar{C}^G_{z*} Y^G & -\gamma I \end{bmatrix} & \begin{bmatrix} \bar{B}^G_{*d} \\ \bar{D}^G_{zd} \end{bmatrix} \\ [(\bar{B}^G_{*d})^T \quad (\bar{D}^G_{zd})^T] & -\gamma I \end{bmatrix} \begin{bmatrix} N_Y & 0 \\ 0 & I \end{bmatrix} < 0, \tag{4.10}$$

$$\begin{bmatrix} N_X & 0 \\ 0 & I \end{bmatrix}^T \begin{bmatrix} \begin{bmatrix} (\bar{A}^G)^T X^G + X^G \bar{A}^G & X^G \bar{B}^G_{*d} \\ (\bar{B}^G_{*d})^T X^G & -\gamma I \end{bmatrix} & \begin{bmatrix} (\bar{C}^G_{z*})^T \\ (\bar{D}^G_{zd})^T \end{bmatrix} \\ [\bar{C}^G_{z*} \quad \bar{D}^G_{zd}] & -\gamma I \end{bmatrix} \begin{bmatrix} N_X & 0 \\ 0 & I \end{bmatrix} < 0, \tag{4.11}$$

$$\begin{bmatrix} X^G_T & I \\ I & Y^G_T \end{bmatrix} \geq 0, \tag{4.12}$$

where $X^* = diag(X^*_T, X^*_{S,1}, \dots, X^*_{S,L})$ in which $X^*_{S,i} \in R_S^{m_i^* \times m_i^*}$ are symmetric matrices. The null spaces of $[(\bar{B}^G_{u*})^T \quad (\bar{D}^G_{zu})^T]$ and $[\bar{C}^G_{y*} \quad \bar{D}^G_{yd}]$ are denoted as N_x and N_y , respectively.

The X^G and Y^G matrices that satisfy the feasibility conditions can be used to calculate the scaling matrix $\bar{X}$ that is defined as follows:

$$\bar{X} = \begin{bmatrix} X^G & X^{GK} \\ (X^{GK})^T & X^K \end{bmatrix}^{-1} = \begin{bmatrix} Y^G & Y^{GK} \\ (Y^{GK})^T & Y^K \end{bmatrix} \tag{4.12}$$

The following inequality must hold for a well-posed, stable and contractive system. Hence, the controller state-space matrices $\bar{A}^K$, $\bar{B}^K$, $\bar{C}^K$, $\bar{D}^K$ in the transformed domain can be calculated by using the scaling matrix $\bar{X}$ and the following inequality:

$$\begin{bmatrix} (\bar{A}^C)^T \bar{X} + \bar{X} \bar{A}^C & \bar{X} \bar{B}^C & (\bar{C}^C)^T \\ (\bar{B}^C)^T \bar{X} & -I & (\bar{D}^C)^T \\ \bar{C}^C & \bar{D}^C & -I \end{bmatrix} < 0 \tag{4.13}$$

where

$$\begin{bmatrix} \bar{A}^C & \bar{B}^C \\ \bar{C}^C & \bar{D}^C \end{bmatrix} = \begin{bmatrix} A_0 & B_0 \\ C_0 & D_0 \end{bmatrix} + \begin{bmatrix} \widehat{B} \\ \widehat{D}_{12} \end{bmatrix} \theta [\hat{C} \quad \widehat{D}_{21}] \tag{4.14}$$

$$A_0 = \begin{bmatrix} \bar{A}^C & 0 \\ 0 & 0 \end{bmatrix} \;\; B_0 = \begin{bmatrix} \bar{B}^G_{*d} \\ 0 \end{bmatrix} \tag{4.15}$$

$$C_0 = [\bar{C}^G_{z*} \quad 0] \;\; D_0 = \bar{D}^G_{zd} \tag{4.16}$$

$$\widehat{B} = \begin{bmatrix} 0 & \bar{B}^G_{u*} \\ I & 0 \end{bmatrix} \; \hat{C} = \begin{bmatrix} 0 & I \\ \bar{C}^G_{y*} & 0 \end{bmatrix} \tag{4.17}$$

$$\widehat{D}_{12} = [0 \quad \bar{D}^G_{zu}] \;\; \widehat{D}_{21} = \begin{bmatrix} 0 \\ \bar{D}^G_{yd} \end{bmatrix} \tag{4.18}$$

$$\theta = \begin{bmatrix} \bar{A}^K & \bar{B}^K \\ \bar{C}^K & \bar{D}^K \end{bmatrix} \tag{4.19}$$

As a last step, an inverse transform is needed to be performed to obtain the spatially-invariant controller in discrete-spatial domain. In order to take the inverse transform, we first need to find a X_S^K that satisfy the following inequality:

$$(\bar{A}^K_{SS})^T X_S^K + X_S^K \bar{A}^K_{SS} < 0 \tag{4.20}$$

Then, we need to factor each $X_{S,i}^K$ as follows:

$$X_{S,i}^K = (T_i^K)^T \begin{bmatrix} I_{m_i^K} & 0 \\ 0 & -I_{m_{-i}^K} \end{bmatrix} T_i^K \tag{4.21}$$

and apply the state transformation shown below:

$$\bar{A}^K = (T^K)^{-1} \bar{A}^K T^K \tag{4.22}$$

$$\bar{B}^K = (T^K)^{-1} \bar{B}^K \tag{4.23}$$

$$\bar{C}^K = \bar{C}^K T^K \tag{4.24}$$

$$\bar{D}^K = \bar{D}^K \tag{4.25}$$

Now, we can calculate the state-space matrices of the controller in discrete-spatial domain as:

$$A_{SS}^{K} = (\bar{A}_{SS}^{K} H^{K} - I)^{-1} (\bar{A}_{SS}^{K} H^{K} - I) \bar{B}^{K} = (T^{K})^{-1} \bar{B}^{K} \tag{4.26}$$

$$[A_{ST}^{K} \quad B_{S}^{K}] = -\sqrt{2} (\bar{A}_{SS}^{K} H^{K} - I)^{-1} [\bar{A}_{ST}^{K} \quad \bar{B}_{S}^{K}] \tag{4.27}$$

$$\begin{bmatrix} A_{TS}^{K} \\ C_{S}^{K} \end{bmatrix} = \sqrt{2} \begin{bmatrix} \bar{A}_{TS}^{K} \\ \bar{C}_{S}^{K} \end{bmatrix} H^{K} (\bar{A}_{SS}^{K} H^{K} - I)^{-1} \tag{4.28}$$

$$\begin{bmatrix} A_{TT}^{K} & B_{T}^{K} \\ C_{T}^{K} & D^{K} \end{bmatrix} = \begin{bmatrix} \bar{A}_{TT}^{K} & \bar{B}_{T}^{K} \\ \bar{C}_{T}^{K} & \bar{D}^{K} \end{bmatrix} - \begin{bmatrix} \bar{A}_{TS}^{K} \\ \bar{C}_{S}^{K} \end{bmatrix} H^{K} (\bar{A}_{SS}^{K} H^{K} - I)^{-1} [\bar{A}_{ST}^{K} \quad \bar{B}_{S}^{K}] \tag{4.29}$$

where H^{K} is in the form presented in Eq. (4.2).

5. DECOMPOSITION-BASED DISTRIBUTED CONTROL SYNTHESIS

In this chapter we will discuss the synthesis of decomposition-based distributed controllers and give a summary of the method published in [26]. For the complete discussion and proofs please refer to [26].

In [26], it is shown that if the system under investigation has small subsystems interacting with each other and has a certain structural property, the overall system matrices can be converted into block diagonal matrices whose independent blocks represent modal subsystems. This idea of decomposing the system into smaller subsystems to simplify the controller synthesis problem has also been investigated by [35, 36] for the symmetrically interconnected systems, by [37] for the circulant systems and also in the application of SVD controllers [38, 39]. However in these methods instead of synthesizing distributed controllers, the main idea is to reduce the global controller synthesis problem of MIMO system with n inputs and n outputs to a modal controller synthesis problem of n SISO systems by transforming the inputs, outputs and states of the overall system. This approach results in a global controller rather than a distributed controller (see Figure 5-1). In [26], it is shown that after reducing the synthesis problem to independent smaller synthesis problems by imposing additional constraints to the controller synthesis of independent blocks, a distributed controller that has the same interconnection pattern as the plant can be synthesized.

The method presented in [26] assumes a discrete time plant, so in our discussion we assume that our plant is a discrete time system as follows:

$$x(k+1) = Ax(k) + B_w w(k) + B_u u(k), \tag{5.1}$$

$$z(k) = C_z x(k) + D_{zw} w(k) + D_{zu} u(k), \tag{5.2}$$

$$y(k) = C_y x(k) + D_{yw} w(k), \tag{5.3}$$

where $k \in Z$, u is the control input, w is the disturbance input, y is the sensor feedback and z is the error that needs to be bounded.

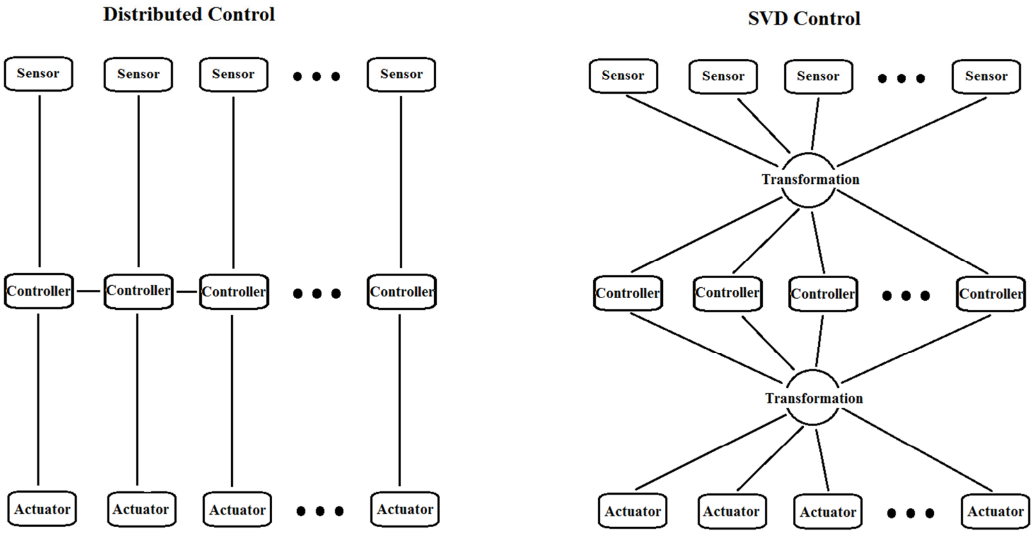

Figure 5-1. Comparision of Distributed and SVD control architectures.

If the state-space matrices of the overall system with n subsystems can be represented as:

$$A = I_n \otimes A_a + P_n \otimes A_b, \tag{5.4}$$

$$B_w = I_n \otimes B_{w_a} + P_n \otimes B_{w_b}, \tag{5.5}$$

$$C_z = I_n \otimes C_{z_a} + P_n \otimes C_{z_b}, \tag{5.6}$$

$$D_{zw} = I_n \otimes D_{zw_a} + P_n \otimes D_{zw_b}, \tag{5.7}$$

$$D_{zu} = I_n \otimes D_{zu_a} + P_n \otimes D_{zu_b}, \tag{5.8}$$

$$C_y = I_n \otimes C_{y_a} + P_n \otimes C_{y_b}, \tag{5.9}$$

$$D_{yw} = I_n \otimes D_{yw_a} + P_n \otimes D_{yw_b}, \tag{5.10}$$

where $P_n \in R^{\mathrm{n} \times \mathrm{n}}$ is a diagonalizable pattern matrix and $\otimes$ represent the Kronecker product [40]. Then, the state-space matrices can be decomposed as follows:

$$\mathbf{A} = (S_n \otimes I_l)^{-1} A (S_n \otimes I_l), \tag{5.11}$$

$$\mathbf{A} = I_n \otimes A_a + \Lambda_{P_n} \otimes A_b, \tag{5.12}$$

where $S_n \in R^{n \times n}$ is a non-singular matrix that diagonalizes P_n with $\Lambda_{P_n} = S_n^{-1} P_n S_n$.

Since I_n and Λ_{P_n} are diagonal, $\mathbf{A}$ is block diagonal. Any independent block matrix $\mathbf{A}_i$ will be of the following form:

$$\mathbf{A}_i = A_a + \lambda_i A_b, \tag{5.13}$$

where λ_i is the *ith* eigen value of P_n and also the *ith* entry in the diagonal of Λ_{P_n}.

So if transformation matrices $(S_n \otimes I_*)$ are applied to the system in Eq. (5.1) as follows:

$$\begin{aligned}(S_n \otimes I_l)^{-1}x(k+1) \\ &= \mathbf{A}(S_n \otimes I_l)^{-1}x(k) + \mathbf{B_w}\left(S_n \otimes I_{m_w}\right)^{-1}w(k) \\ &+ \mathbf{B_u}\left(S_n \otimes I_{m_u}\right)^{-1}u(k),\end{aligned} \tag{5.14}$$

$$\begin{aligned}z(k) = \mathbf{C_z}\left(S_n \otimes I_{r_z}\right)^{-1}x(k) + \mathbf{D_{zw}}\left(S_n \otimes I_{m_w}\right)^{-1}w(k) \\ + \mathbf{D_{zu}}\left(S_n \otimes I_{m_u}\right)^{-1}u(k),\end{aligned} \tag{5.15}$$

$$y(k) = \mathbf{C_y}\left(S_n \otimes I_{r_y}\right)^{-1}x(k) + \mathbf{D_{yw}}\left(S_n \otimes I_{m_w}\right)^{-1}w(k). \tag{5.16}$$

Then with the following change of variables:

$$x = (S_n \otimes I_l)\hat{x}, \tag{5.17}$$

$$w = \left(S_n \otimes I_{m_w}\right)\widehat{w}, \tag{5.18}$$

$$u = \left(S_n \otimes I_{m_u}\right)\hat{u}, \tag{5.19}$$

$$z = \left(S_n \otimes I_{r_z}\right)\hat{z}, \tag{5.20}$$

$$y = \left(S_n \otimes I_{r_y}\right)\hat{y}. \tag{5.21}$$

We will obtain the system:

$$\hat{x}(k+1) = \mathbf{A}\hat{x}(k) + \mathbf{B_w}\widehat{w}(k) + \mathbf{B_u}\hat{u}(k), \tag{5.22}$$

$$\hat{z}(k) = \mathbf{C_z}\hat{x}(k) + \mathbf{D_{zw}}\widehat{w}(k) + \mathbf{D_{zu}}\hat{u}(k), \tag{5.23}$$

$$\hat{y}(k) = \mathbf{C_y}\hat{x}(k) + \mathbf{D_{yw}}\widehat{w}(k), \tag{5.24}$$

where the system matrices $\mathbf{A}$, $\mathbf{B_w}$, $\mathbf{B_u}$, $\mathbf{C_z}$, $\mathbf{C_y}$, $\mathbf{D_{zw}}$, $\mathbf{D_{zu}}$, $\mathbf{D_{yw}}$ are all block diagonal. Hence we will have n independent modal subsystems as follows:

$$\hat{x}_i(k+1) = \mathbf{A}_{\boldsymbol{i}}\hat{x}_i(k) + \mathbf{B}_{\mathbf{w}_{\boldsymbol{i}}}\widehat{w}_i(k) + \mathbf{B}_{\mathbf{u}_{\boldsymbol{i}}}\hat{u}_i(k), \tag{5.25}$$

$$\hat{z}_i(k) = \mathbf{C}_{\mathbf{z}_{\boldsymbol{i}}}\hat{x}(k) + \mathbf{D}_{\mathbf{zw}_{\boldsymbol{i}}}\widehat{w}_i(k) + \mathbf{D}_{\mathbf{zu}_{\boldsymbol{i}}}\hat{u}_i(k), \tag{5.26}$$

$$\hat{y}_i(k) = \mathbf{C}_{\mathbf{y}_{\boldsymbol{i}}}\hat{x}_i(k) + \mathbf{D}_{\mathbf{yw}_{\boldsymbol{i}}}\widehat{w}_i(k), \tag{5.27}$$

for $i = 1, \dots, n$ and where $\hat{x}_i$, $\widehat{w}_i$, $\hat{u}_i$, $\hat{z}_i$ and $\hat{y}_i$ are the i^{th} blocks of $\hat{x}$, $\widehat{w}$, $\hat{u}$, $\hat{z}$ and $\hat{y}$ respectively. It should be noted that these independent subsystems are not physical subsystems but rather "*modal*" subsystems.

The Eq.s (5.25)-(5.27) can also be represented as:

$$\begin{aligned}\hat{x}_i(k+1) = (A_a + \lambda_i A_b)\hat{x}_i(k) + \left(B_{w_a} + \lambda_i B_{w_b}\right)\widehat{w}_i(k) \\ + \left(B_{u_a} + \lambda_i B_{u_b}\right)\hat{u}_i(k),\end{aligned} \tag{5.28}$$

$$\begin{aligned}\hat{z}_i(k) = \left(C_{z_a} + \lambda_i C_{z_b}\right)\hat{x}(k) + \left(D_{zw_a} + \lambda_i D_{zw_b}\right)\widehat{w}_i(k) \\ + \left(D_{zu_a} + \lambda_i D_{zu_b}\right)\hat{u}_i(k),\end{aligned} \tag{5.29}$$

$$\hat{y}_i(k) = \left(C_{y_a} + \lambda_i C_{y_b}\right)\hat{x}_i(k) + \left(D_{yw_a} + \lambda_i D_{yw_b}\right)\widehat{w}_i(k), \tag{5.30}$$

for $i = 1, \dots, n$.

After decomposing the global system into n independent modal subsystems, a controller can be synthesized for each subsystem and by concatenation a global controller can be calculated.

Assume a static feedback controller for each independent subsystem as:

$$\hat{u}_i = \mathbf{K_i}\hat{x}_i, \tag{5.31}$$

for $i = 1, \dots, n$ or dynamic output feedback controllers as:

$$\hat{x}_{c_i}(k+1) = \mathbf{A}_{\mathbf{c_i}}\hat{x}_{c_i}(k) + \mathbf{B}_{\mathbf{c_i}}\hat{y}_i(k), \tag{5.32}$$

$$\hat{u}_i = \mathbf{C}_{\mathbf{c_i}}\hat{x}_{c_i}(k) + \mathbf{D}_{\mathbf{c_i}}\hat{y}_i(k), \tag{5.33}$$

for $i = 1, \dots, n$.

Then a global controller for the transformed system can be calculated by concatenating the controller matrices and if an inverse transformation is applied as follows:

$$K = \left(S_n \otimes I_{m_u}\right)\mathbf{K}(S_n \otimes I_l)^{-1}, \tag{5.34}$$

$$A_c = (S_n \otimes I_l)\mathbf{A}(S_n \otimes I_l)^{-1}, \tag{5.35}$$

$$B_c = (S_n \otimes I_l)\mathbf{B}\left(S_n \otimes I_{r_y}\right)^{-1}, \tag{5.36}$$

$$C_c = \left(S_n \otimes I_{m_u}\right)\mathbf{C}(S_n \otimes I_l)^{-1}, \tag{5.37}$$

$$D_c = \left(S_n \otimes I_{m_u}\right)\mathbf{D}\left(S_n \otimes I_{r_y}\right)^{-1}, \tag{5.38}$$

a controller in the untransformed domain will be synthesized. However this controller will mostly likely be not a distributed controller that has the same interconnection pattern as the plant. To be able to synthesize a distributed controller that has the same interconnection pattern as the system itself, additional constraints should be imposed to the solution space of the controller synthesis problem of independent modal subsystems.

While synthesizing a distributed controller, one should be careful about the norms of the systems as the system norm in the transformed space differs from the system norms in the original space. Following is the relation of norms between two spaces:

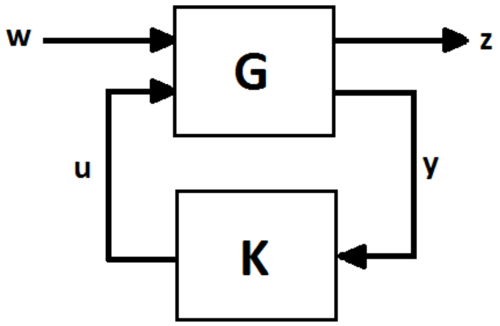

Figure 5-2. Closed-loop system representation for a generic H∞ synthesis algorithm.

$$\frac{\underline{\sigma}(S_n)}{\overline{\sigma}(S_n)}\left\|\hat{T}_{\hat{w}\hat{z}}\right\|_\infty \leq \|T_{wz}\|_\infty \leq \frac{\overline{\sigma}(S_n)}{\underline{\sigma}(S_n)}\left\|\hat{T}_{\hat{w}\hat{z}}\right\|_\infty, \tag{5.39}$$

where $\overline{\sigma}(S_n)$ and $\underline{\sigma}(S_n)$ are the maximum and minimum singular values of S_n respectively.

In our problem, we want to control a plant in discrete time:

$$x(k+1) = Ax(k) + B_w w(k) + B_u u(k), \tag{5.40}$$

$$z(k) = C_z x(k) + D_{zw} w(k) + D_{zu} u(k), \tag{5.41}$$

$$y(k) = C_y x(k) + D_{yw} w(k), \tag{5.42}$$

by using a dynamic controller:

$$x_c(k+1) = A_c x_c(k) + B_c y(k), \tag{5.43}$$

$$u(k) = C_c x_c(k) + D_c y(k), \tag{5.44}$$

that have the same interconnection pattern as the plant to make the $\|T_{wz}\|_\infty < 1$ as shown in Figure 5-2.

To be able to achieve our goal, after decomposing the system into smaller independent modal subsystems, if the set of additional constraints below:

$$X_i = X, \tag{5.45}$$

$$Y_i = Y, \tag{5.46}$$

$$S_i = S, \tag{5.47}$$

$$\mathbf{L_i} = L_a + \lambda_i L_b, \tag{5.48}$$

$$\mathbf{F_i} = F_a + \lambda_i F_b, \tag{5.49}$$

$$\mathbf{Q_i} = Q_a + \lambda_i Q_b, \tag{5.50}$$

$$\mathbf{R_i} = R_a + \lambda_i R_b, \tag{5.51}$$

$$P_i = P_i^T, H_i = H_i^T, J_i \text{ unconstrained for } i = 1, \dots, n. \tag{5.52}$$

together with

$$VU = S - YX \tag{5.53}$$

$$\mathbf{D_{c_i}} = \mathbf{R_i} \tag{5.54}$$

$$\mathbf{C_{c_i}} = (\mathbf{L_i} - \mathbf{R_i}\mathbf{C_{y_i}}X)U^{-1} \tag{5.55}$$

$$\mathbf{B_{c_i}} = V^{-1}(\mathbf{F_i} - Y\mathbf{B_{u_i}}\mathbf{R_i}) \tag{5.56}$$

$$\begin{aligned}\mathbf{A_{c_i}} = V^{-1}\left(\mathbf{Q_i} - Y\left(\mathbf{A_i} + \mathbf{B_{u_i}}\mathbf{R_i}\mathbf{C_{y_i}}\right)X - V\mathbf{B_{c_i}}\mathbf{C_{y_i}}X\right)U^{-1} \\ - V^{-1}Y\mathbf{B_{u_i}}C_{c_i}\end{aligned} \tag{5.57}$$

are applied to the decision variables in the solution space of the LMIs below:

$$\begin{bmatrix} P_i & J_i & \mathbf{A_i}X_i + \mathbf{B_{u_i}}\mathbf{L_i} & \mathbf{A_i} + \mathbf{B_{u_i}}\mathbf{R_i}\mathbf{C_{y_i}} & \mathbf{B_{w_i}} + \mathbf{B_{u_i}}\mathbf{R_i}\mathbf{D_{yw_i}} & 0 \\ * & H_i & \mathbf{Q_i} & Y_i\mathbf{A_i} + \mathbf{F_i}\mathbf{C_{y_i}} & Y_i\mathbf{B_{w_i}} + \mathbf{F_i}\mathbf{D_{yw_i}} & 0 \\ * & * & X_i + X_i^T - P_i & I_l + S_i^T - J_i & 0 & X_i^T\mathbf{C_{z\,i}^T} + \mathbf{L_i^T}\mathbf{D_{zu_i}^T} \\ * & * & * & Y_i + Y_i^T - H_i & 0 & \mathbf{C_{z\,i}^T} + \mathbf{C_y^T}\mathbf{R_i^T}\mathbf{D_{zu_i}^T} \\ * & * & * & * & I_{m_w} & \mathbf{D_{zw_i}^T} + \mathbf{D_{yw_i}^T}\mathbf{R_i^T}\mathbf{D_{zu_i}^T} \\ * & * & * & * & * & I_{r_z} \end{bmatrix} > \tag{5.58}$$

0 for $i = 1, \dots, n$.

one can synthesize a controller that has the same interconnection pattern as the plant.

In Eq. (5.58) whenever there is a product of two or more bold matrices, all the matrices except one should be constant over the index *i*.

6. FOURIER-BASED DISTRIBUTED AND CENTRALIZED H_∞ CONTROL OF DYNAMICALLY UNCOUPLED LARGE SEGMENTED TELESCOPES

In this chapter, the Fourier-based distributed H_∞ control of the primary mirror of the next generation telescopes is investigated. Both spatially-invariant distributed and centralized controllers are designed for simplified dynamic model of a 37 segment test unit. Firstly, the 37 segment system is calculated as described in Section 2.1. A centralized H_∞ controller is, then, designed and simulated in MatLab-Simulink environment. Next, the simulation results are presented and the performance of the controller is evaluated. Thirdly, spatially-invariant distributed controller is calculated following steps in Chapter 3. The spatially-invariant distributed controller is simulated for the 37 segment system. The simulation results of the controller is presented and compared with the results from centralized scheme. It is shown that both centralized and spatially-invariant distributed controllers satisfy the imaging performance requirements. The results of this chapter are published in [41].

After calculating the dynamically uncoupled 37-segment system model by following Section 2.1, to achieve control objective relative displacements from system outputs are needed to be defined. First, the absolute positions of the edge sensing points are determined as follows:

$$y_{s_i} = \begin{bmatrix} 5/3 & -7/9 & 1/9 & 0 & 0 & 0 \\ 5/3 & 1/9 & -7/9 & 0 & 0 & 0 \\ 13/9 & 5/9 & -1 & 0 & 0 & 0 \\ 5/9 & 13/9 & -1 & 0 & 0 & 0 \\ 1/9 & 5/3 & -7/9 & 0 & 0 & 0 \\ -7/9 & 5/3 & 1/9 & 0 & 0 & 0 \\ -1 & 5/3 & 5/9 & 0 & 0 & 0 \\ -1 & 5/3 & 13/9 & 0 & 0 & 0 \\ -7/9 & 13/9 & 5/3 & 0 & 0 & 0 \\ 1/9 & -7/9 & 5/3 & 0 & 0 & 0 \\ 5/9 & -1 & 13/9 & 0 & 0 & 0 \\ 13/9 & -1 & 5/9 & 0 & 0 & 0 \end{bmatrix} x_i, \tag{6.1}$$

where $y_{s_i} \in R^{12}$ is the vector of the absolute positions of the sensing points. Then, relative displacements are calculated by subtracting the absolute positions of the sensing points on the edges from the corresponding points of the neighbouring segments. Sensing points and supporting points are shown in Figure 6-1. Figure 6-2 shows the 37-segment system with spatial dimensions.

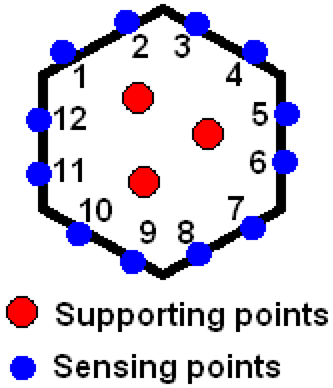

Figure 6-1. Supporting and sensing points.

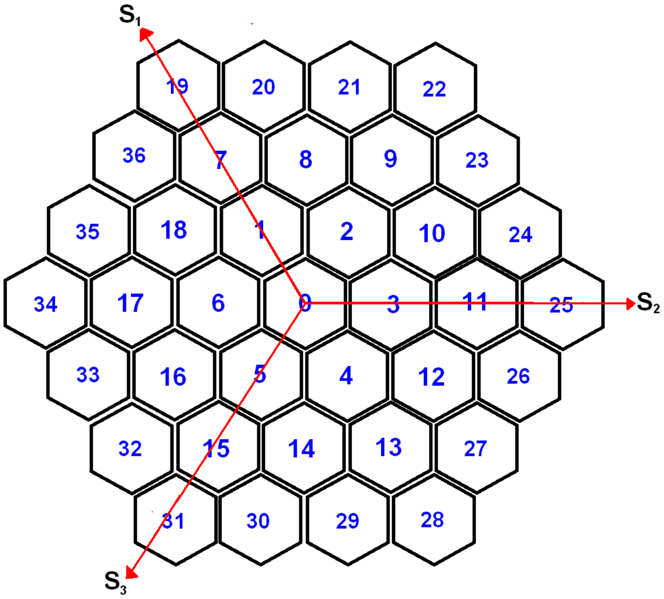

Figure 6-2. Spatial shift directions for 37-segment system.

6.1 Centralized controller

For the centralized control of 37-segments, the relative displacements are calculated as follows:

$$z_1 = C_m x, \tag{6.2}$$

where $C_m \in R^{444\times222}$ maps system state to the relative displacements and $z_1 \in R^{444}$ is the output of the system which gives the relative displacements of the segments. In order to meet the imaging performance requirements set in [2] and calculated in [31], a controller that achieves relative displacements less than 10^{-8} meters must be synthesized. Since C_m is rank degenerate, we also include the absolute displacement of *0th* segment y_0 and the average displacements of all supporting segments $r = (1/111)\sum_{i=0}^{37}(x_i^T[1 \quad 1 \quad 1]^T)$, where $z_2 = [y_0^T \quad r^T]^T \in R^4$. Then, our system output with the scaling factors η and $\beta = 10^8$ for the controller synthesis becomes $z_x = [\beta z_1^T \quad \eta z_2^T]^T = W_x x$. Since our synthesis assumes unit inputs, some scaling for the disturbance input w and the control input u is needed. For the disturbance scaling, as in [31], we adopt Von Karman model for the wind pressure power spectral density (PSD):

$$\Phi_{\mathrm{pt}}^{vK} = \frac{C_{pt}^{vK}}{\left[1+\left(\frac{f}{f_0}\right)^2\right]^{\frac{7}{6}}} \tag{6.3}$$

where C_{pt}^{vK} is the magnitude and f_0 is the bandwidth of the model. The magnitude and the bandwidth of the model is determined to be 10 and $\frac{1}{2\pi}$ Hz , respectively. A white noise filter of order two can be used to approximate the force disturbance. With the help of least-squares estimation, white noise force filter $W_{ni} = \frac{0.01941s+0.3043}{0.1196s^2+1.32s+1}$ for $i = \{i \in Z \mid 0 \le i \; and \; i \le 36\}$ is calculated. The noise scaling transfer function matrix for the 37-segment system is given by:

$$W_n = \begin{bmatrix} W_{n0} & & \\ & \ddots & \\ & & W_{n36} \end{bmatrix}. \tag{6.4}$$

For the control input scaling, we use a high-pass filter $W_{ui} = \frac{s+1}{s+1000}$ for each control channel to limit the bandwidth and the gain of the controller. As in disturbance filter, the filter for the 37-segment system is defined as:

$$W_u = \begin{bmatrix} W_{u0} & & \\ & \ddots & \\ & & W_{u36} \end{bmatrix}, \tag{6.5}$$

Figure 6-3 shows the system that is used for the centralized controller synthesis.

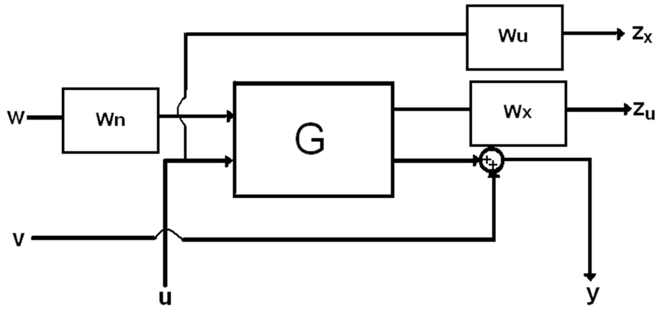

Figure 6-3. System for centralized H_∞ synthesis.

6.2 Simulation results for centralized H_∞ control

Our objective, as described in the previous sections, is to design a controller which achieves relative displacements in the orders of 10^{-8} meters. In Figure 6-4, we show some of the inter-edge relative displacements for the open-loop system. Figure 6-5 shows the same displacements with the controller activated. The sample actuator forces generated during the simulation is presented in Figure 6-6.

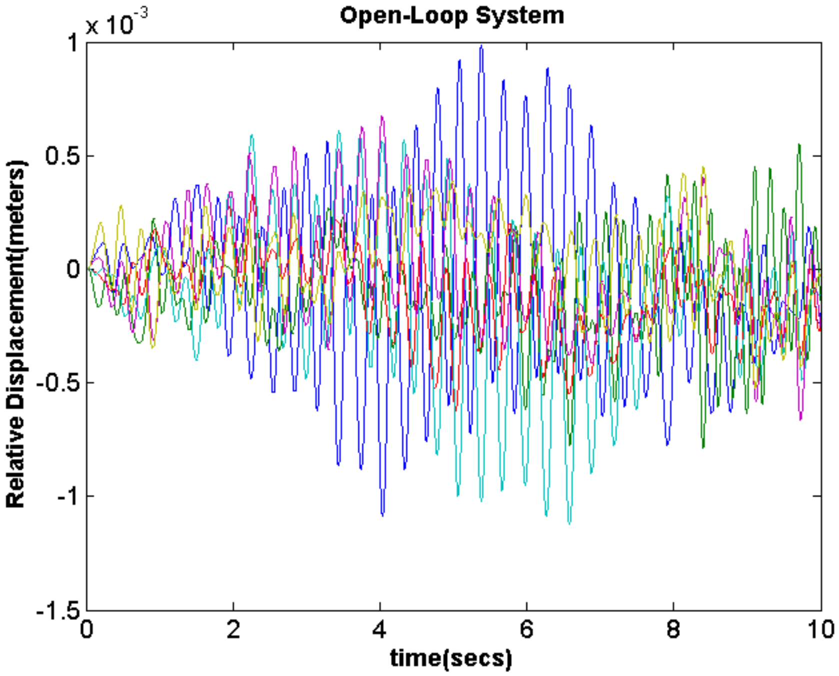

Figure 6-4. Simulation results for open-loop system.

6.3 Spatially-invariant distributed H$_\infty$ control

As described in Chapter 1, when the number of segments increases the centralized schemes become intractable and require too much computation power. To overcome the drawbacks and to achieve the global performance requirement which is coupled among the segments, we apply a distributed control scheme proposed in [24] to H$_\infty$ synthesis procedure described in previous Section 3.1.

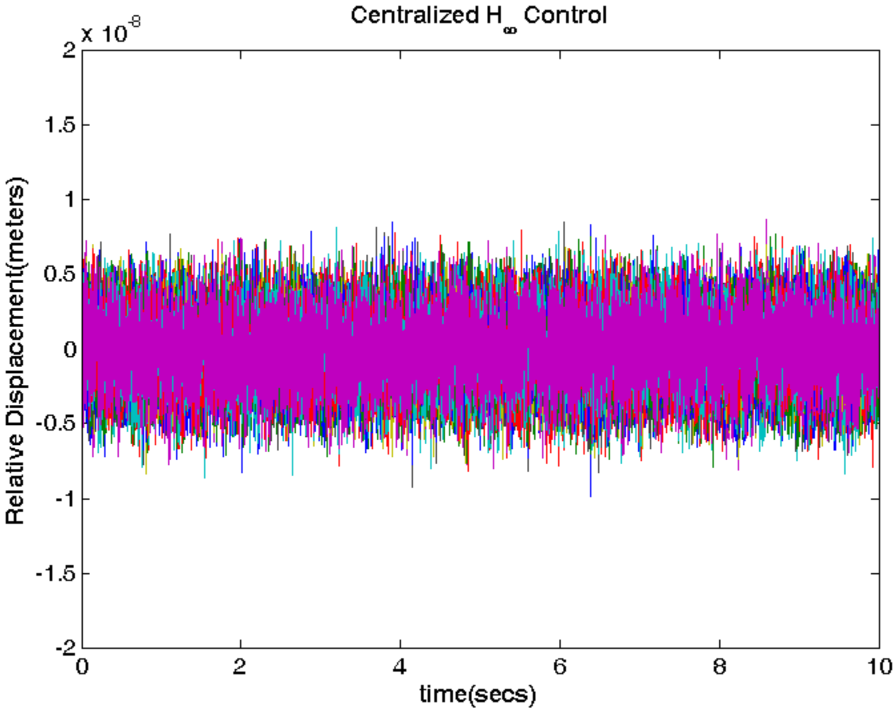

Figure 6-5. Simulation results for centralized H$_\infty$ control.

Before going into details, we need to define spatial invariance in our system. In Figure 6-2, three spatial directions are shown. The system is spatially-invariant under the translation operators S_1, S_2 and S_3 corresponding to the spatial directions. Some examples of spatial operations are $x_1 = S_1 x_0$, $x_4 = S_1^{-1} x_0$ and $A_1 = S_1 A_0 = A_0$. Notice that, these operators are geometrically symmetric and $S_i S_j S_k = 1$ for different i, j and k. In order to incorporate relative displacements to the distributed model of one segment, shift operators can be made use of in the output equation as:

$$z_i = \begin{bmatrix} -S_1 - \frac{5}{3} & \frac{5}{9}S_1 + \frac{7}{9} & \frac{13}{9}S_1 - \frac{1}{9} & 0 & 0 & 0 \\ -S_1 - \frac{5}{3} & \frac{13}{9}S_1 - \frac{1}{9} & \frac{5}{9}S_1 + \frac{7}{9} & 0 & 0 & 0 \\ \frac{13}{9}S_2 - \frac{1}{9} & -S_2 - \frac{5}{3} & \frac{5}{9}S_2 + \frac{7}{9} & 0 & 0 & 0 \\ \frac{5}{9}S_2 + \frac{7}{9} & -S_2 - \frac{5}{3} & \frac{13}{9}S_2 - \frac{1}{9} & 0 & 0 & 0 \\ \frac{5}{9}S_3 + \frac{7}{9} & \frac{13}{9}S_3 - \frac{1}{9} & -S_3 - \frac{5}{3} & 0 & 0 & 0 \\ \frac{13}{9}S_3 - \frac{1}{9} & \frac{5}{9}S_3 + \frac{7}{9} & -S_3 - \frac{5}{3} & 0 & 0 & 0 \end{bmatrix} x_i = [C_{zi} \quad 0_{6\times3}]x_i \tag{6.6}$$

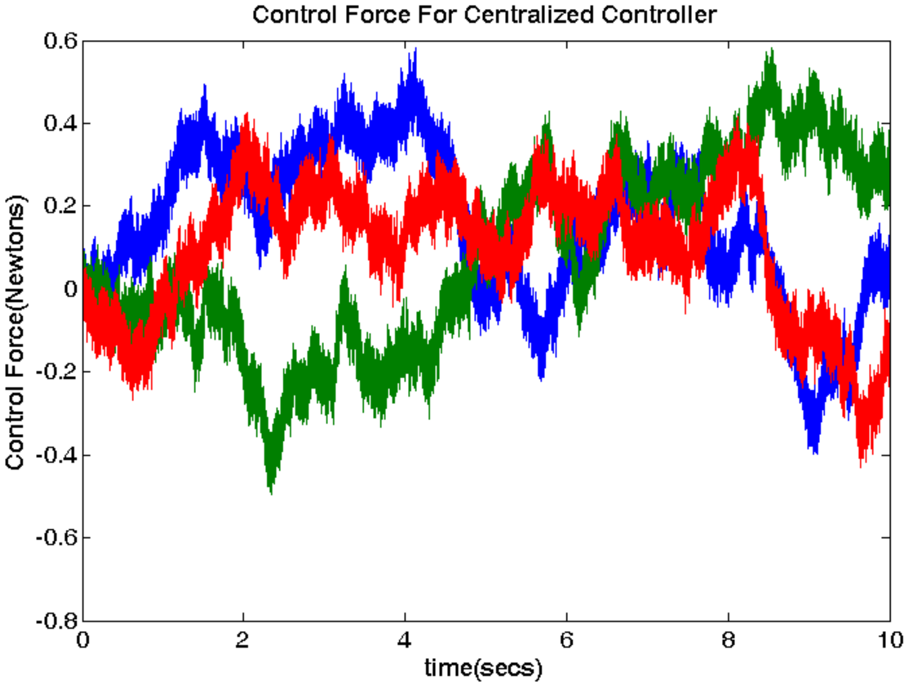

Figure 6-6. Sample actuator forces generated during the centralized simulation.

Notice that C_{zi} has full column rank almost everywhere. So by controlling relative displacements, one could also keep the absolute displacements small. In the distributed system output for the controller synthesis, we could ignore absolute positions. As in centralized scheme, the same scaling matrices(with reducing size to $R^{3\times3}$) are used and the output scaling matrix $W_x = \gamma C_{zi}$, where γ is weighting scalar, only includes relative displacements. The overall system that is used in synthesis with scaling matrices is similar to the Figure 6-3.

To synthesize the spatially-invariant distributed controller, we calculate the overall state-space equation:

$$\dot{x} = Ax + B_1 w + B_2 u, \tag{6.7}$$

$$z = C_1 x + D_{12} u, \tag{6.8}$$

$$y = C_2 x + D_{21} w. \tag{6.9}$$

Then, as described in [24], we take the Fourier transform to put the system into decoupled form:

$$\frac{\partial \breve{x}}{\partial t} = \breve{A}\breve{x} + \breve{B}_1 \breve{w} + \breve{B}_2 \breve{u}, \tag{6.10}$$

$$\breve{z} = \breve{C}_1 \breve{x} + \breve{D}_{12} \breve{u}, \tag{6.11}$$

$$\breve{y} = \breve{C}_2 \breve{x} + \breve{D}_{21} \breve{w}. \tag{6.12}$$

By going through the design steps from Section 3.1, one can obtain a controller in Fourier domain. Although by calculating the inverse Fourier of the calculated controller, a spatially invariant distributed controller could be determined, calculating the inverse Fourier is not easy and possibly includes infinite degree in shift operators. However, since, as described in [24], the convolution kernels have exponential rates of decay, by approximating the shift operator depended terms with finite neighbourhood terms, a controller can be approximated. By limiting the communication to the first neighbourhood, the state-space matrices of the controller can be approximated by least-squares estimation. In this case, the state-space matrices take the following form:

$$A_K(S) = A_{K0} + A_{K1}S_1 + A_{K2}S_2 + A_{K3}S_3 + A_{K4}S_1^{-1} + A_{K5}S_2^{-1} + A_{K6}S_3^{-1}, \tag{6.13}$$

$$B_K(S) = B_{K0} + B_{K1}S_1 + B_{K2}S_2 + B_{K3}S_3 + B_{K4}S_1^{-1} + B_{K5}S_2^{-1} + B_{K6}S_3^{-1}, \tag{6.14}$$

$$C_K(S) = C_{K0} + C_{K1}S_1 + C_{K2}S_2 + C_{K3}S_3 + C_{K4}S_1^{-1} + C_{K5}S_2^{-1} + C_{K6}S_3^{-1}, \tag{6.15}$$

$$D_K(S) = D_{K0} + D_{K1}S_1 + D_{K2}S_2 + D_{K3}S_3 + D_{K4}S_1^{-1} + D_{K5}S_2^{-1} + D_{K6}S_3^{-1}. \tag{6.16}$$

By gridding the Fourier frequencies and following the design procedure in section 3.1, the exact solutions for the matrices at frequency domain can be calculated. At $m^{th} = [\theta_{1m} \quad \theta_{2m} \quad \theta_{3m}]$ gridding point, approximation becomes:

$$\begin{aligned} A_{K_m} \cong A_{K0} &+ A_{K1} I_n e^{j\theta_{1m}} + A_{K2} I_n e^{j\theta_{2m}} + A_{K3} I_n e^{j\theta_{3m}} \\ &+ A_{K4} I_n e^{-j\theta_{1m}} + A_{K5} I_n e^{-j\theta_{2m}} + A_{K6} I_n e^{-j\theta_{3m}} \end{aligned} \tag{6.17}$$

$$\begin{aligned} B_{K_m} \cong B_{K0} &+ B_{K1} I_n e^{j\theta_{1m}} + B_{K2} I_n e^{j\theta_{2m}} + B_{K3} I_n e^{j\theta_{3m}} \\ &+ B_{K4} I_n e^{-j\theta_{1m}} + B_{K5} I_n e^{-j\theta_{2m}} + B_{K6} I_n e^{-j\theta_{3m}} \end{aligned} \tag{6.18}$$

$$\begin{aligned} C_{K_m} \cong C_{K0} &+ C_{K1} I_n e^{j\theta_{1m}} + C_{K2} I_n e^{j\theta_{2m}} + C_{K3} I_n e^{j\theta_{3m}} + C_{K4} I_n e^{-j\theta_{1m}} \\ &+ C_{K5} I_n e^{-j\theta_{2m}} + C_{K6} I_n e^{-j\theta_{3m}} \end{aligned} \tag{6.19}$$

$$\begin{aligned} D_{K_m} \cong D_{K0} &+ D_{K1} I_n e^{j\theta_{1m}} + D_{K2} I_n e^{j\theta_{2m}} + D_{K3} I_n e^{j\theta_{3m}} \\ &+ D_{K4} I_n e^{-j\theta_{1m}} + D_{K5} I_n e^{-j\theta_{2m}} + D_{K6} I_n e^{-j\theta_{3m}} \end{aligned} \tag{6.20}$$

After getting values from enough gridding points and by using least-squares estimation, all coefficients for the shift operators in the controller state matrices can be determined. The designed controller has the following state-space form:

$$\begin{aligned} \dot{x} = &(A_{K0} + A_{K1} S_1 + A_{K2} S_2 + A_{K3} S_3 + A_{K4} S_1^{-1} + A_{K4} S_2^{-1} + A_{K4} S_3^{-1}) x \\ &+ (B_{K0} + B_{K1} S_1 + B_{K2} S_2 + B_{K3} S_3 + B_{K4} S_1^{-1} + B_{K4} S_2^{-1} \\ &+ B_{K4} S_3^{-1}) y, \end{aligned} \tag{6.21}$$

$$\begin{aligned} u = &(C_{K0} + C_{K1} S_1 + C_{K2} S_2 + C_{K3} S_3 + C_{K4} S_1^{-1} + C_{K4} S_2^{-1} + C_{K4} S_3^{-1}) x \\ &+ (D_{K0} + D_{K1} S_1 + D_{K2} S_2 + D_{K3} S_3 + D_{K4} S_1^{-1} + D_{K4} S_2^{-1} \\ &+ D_{K4} S_3^{-1}) y. \end{aligned} \tag{6.22}$$

Notice that the controller needs both the controller states and the outputs of the neighbouring segments.

6.4 Simulation results for distributed H_∞ control

As in the centralized scheme, 37-segment system model is used for the simulations. The results show that the relative displacements of inter-edge points can be kept under 10^{-8} meters as set by the imaging requirements. Some of the relative inter-edge displacements are shown in Figure 6-7. The sample actuator forces generated during the simulation is presented in Figure 6-8.

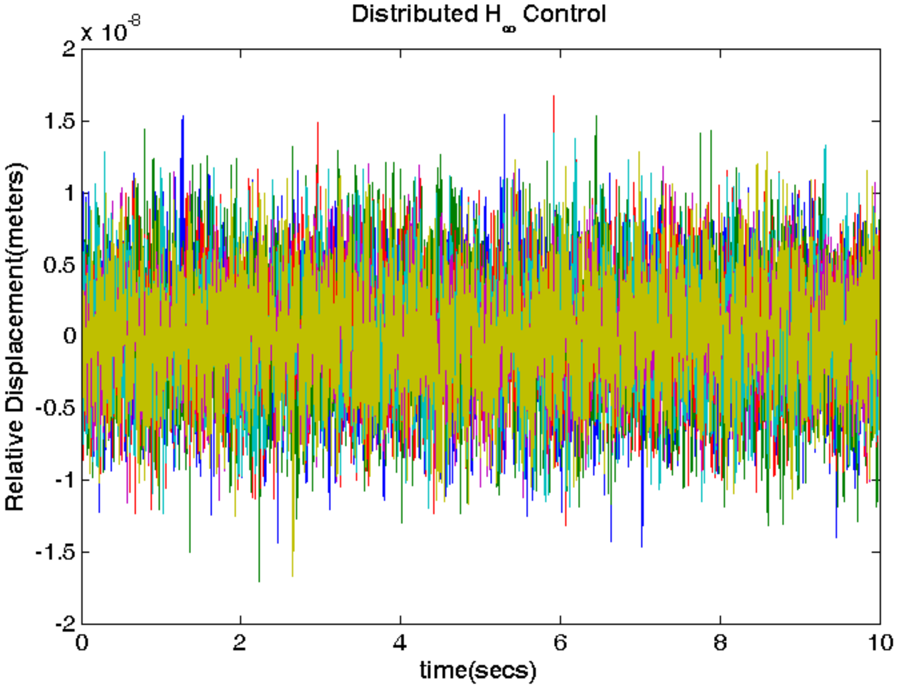

Figure 6-7. Simulation results for distributed H_∞ control.

6.5 Conclusion

In this chapter, the H_∞ control of dynamically uncoupled large segmented mirrors is investigated. As the number of segments increases the control of the telescope becomes a challenging task. Centralized control schemes require time consuming computations which make them infeasible considering the control bandwidth requirements and the current computation power of computers. Decentralized control schemes are easier to implement and less prone to errors compared to the centralized schemes, however they generally lack global performance objectives. A networked distributed control scheme is a compromise and can be tuned between two extremes according to the objectives. We introduce some background information about both the next generation telescope structures and the research work done proving the existence of the truncated local controllers which can accomplish relative displacement objectives. To evaluate our controller performance, 37-segment test unit is modelled in a dynamically uncoupled way by assuming a nodal model. Although the model is dynamically uncoupled, the global objective of keeping relative displacement small is coupled among the segments. Both spatially-invariant distributed and centralized controllers are synthesized for the modelled unit. The simulation results for both controllers are shown to satisfy the imaging performance requirements set by previous research. One should keep in mind that the centralized control problem requires more computation power as the number of segments increases. However, spatially-invariant distributed control problem is independent from the number of segments in the design. Our next research goal is to include structural interactions to the model and investigate networked controllers for a system where both the objective and the dynamics are coupled among the segments.

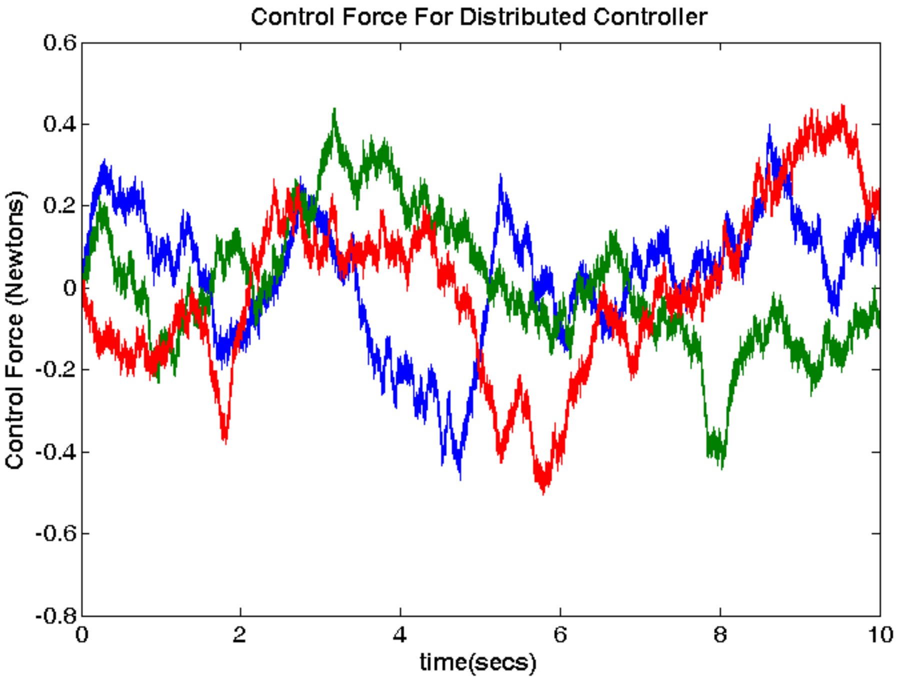

Figure 6-8. Sample actuator forces generated during the distributed simulation.

7. DECOMPOSITION-BASED DISTRIBUTED H_∞ CONTROL OF DYNAMICALLY UNCOUPLED LARGE SEGMENTED MIRRORS

In this chapter, we investigate the decomposition-based distributed H_∞ control of dynamically uncoupled large segmented mirrors. Although the system under investigation is dynamically uncoupled, aligning the mirror segments to maintain the continuity of the primary mirror against disturbances requires co-operation among individual segment controllers. This co-operation could be achieved via distributed control techniques. A 492-segment system (similar to the TMT primary mirror) is chosen to show the applicability of the theory to the active control of segmented mirrors. Distributed control technique applied uses decomposition method to simplify the problem of the controller synthesis and by imposing additional constraints to the linear matrix inequality solution space in the expense of sub-optimality a distributed controller that has the same interconnection pattern as the system is synthesized. Synthesized distributed controller is tested through simulations and is shown to satisfy the imaging performance requirement for diffraction-limited observations. The results of this chapter are published in [42].

7.1 Modelling

In order to model TMT-like 492-segment dynamically uncoupled primary mirror, the procedure described in Section 2.1 is followed. Figure 7-1 shows the TMT-like system layout.

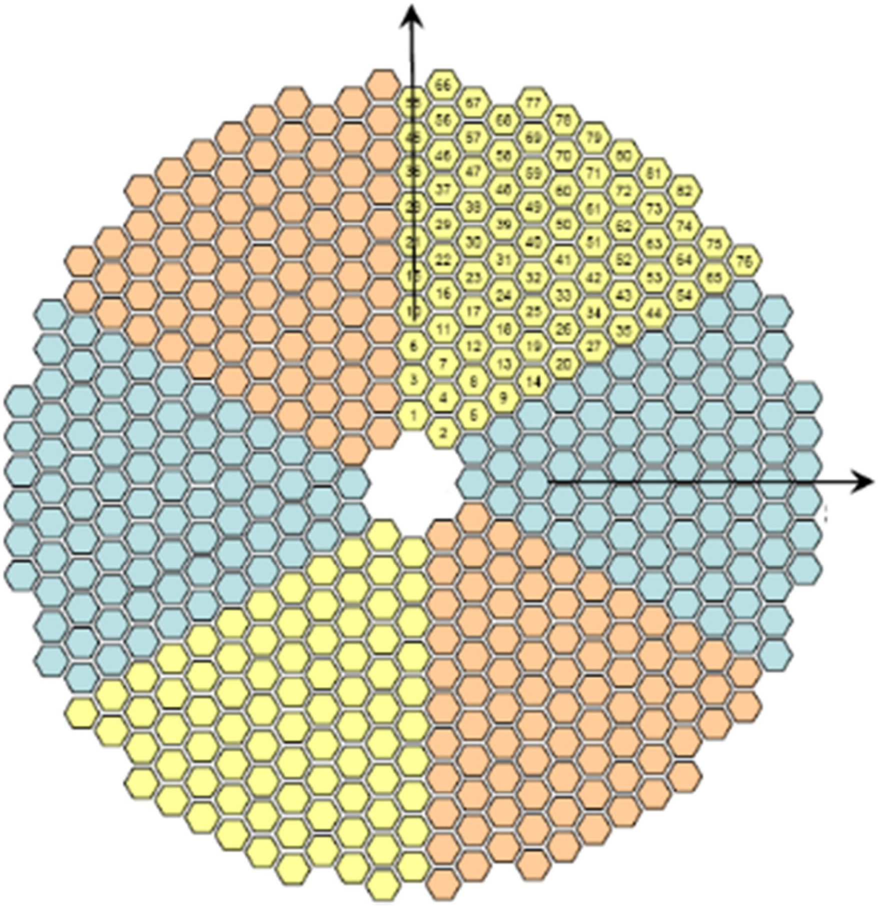

Figure 7-1. 492-segment TMT-like system [42].

7.2 Setting up the model

7.2.1 Disturbance inputs

In the algorithms currently used to control the existing telescopes, the size of the primary mirror allows engineers to neglect the wind disturbance acting on the primary mirror inside the telescope dome. However, with the drastic size increase in the next generation telescopes wind disturbance becomes the major source of disturbance surpassing thermal and gravitational disturbances [18]. Compared to the other sources of disturbances acting on the primary mirror, wind disturbance includes higher frequency spectrum that requires faster responses from controllers. Since in this paper H_∞ approach (i.e. keeping the worst-case rms gain below a threshold) is considered, rms value of the input disturbance should be taken into account. In [31], white noise force filter is calculated as $\frac{0.01941s+0.3043}{0.1196s^2+1.32s+1}$. With this filter the expected wind disturbance rms value can be calculated as 0.1904 N. However from our experience of extensive simulations and to be more conservative in our analysis we scale the input force disturbance of i^{th} segment through $W_{wi} = 0.3 \times I_3$ as shown in Figure 7-2.

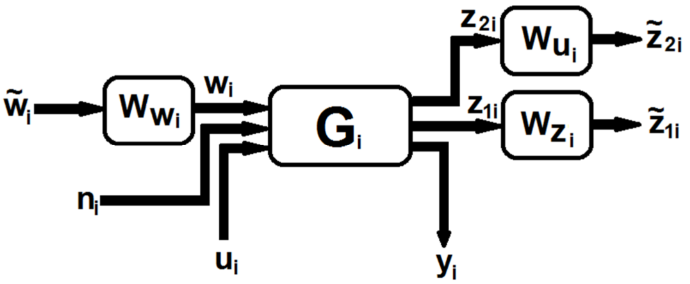

Figure 7-2. Control system block diagram for the H∞ synthesis.

7.2.2 Imaging performance requirement

Every imaging device suffers from the phenomenon called the diffraction of light when they are used in their limits. Even with a perfect imaging system, it is not possible to capture infinite resolution images. For any device this limit can be calculated by taking into account the geometry of the optical structure. In [31] this limit is calculated for the geometry of the system considered in this paper. According to [31], the rms value of relative edge displacements should be kept around 10^{-8} meters to not limit the captured image resolution. In our H∞ approach, to take this limit as our objective, the performance output z_i is scaled with $W_{zi} = 2 \times 10^7 \times I_3$ filter (see Figure 7-2). Considering the relation between the relative actuation point displacements and the segment edge misalignments if the relative displacements of the actuation points could be kept below this limit, our controller is proven to have not put any restrictions to the observed image resolution as the telescope already works in its diffraction limit.

7.2.3 Control input and noise

In our controller synthesis, to be able to synthesize a controller that is physically feasible, input is also filtered through $W_{ui} = (s + 10)/(s + 1000)$ to constrain the frequency and the force of the controller (see Figure 7-2). Also, noise n_i is added to the sensor readings to better implement the working conditions of the telescope controller. This noise is comparable to the noise currently present in the sensor readings of the Keck telescope.

7.2.4 Overall system state-space

In this chapter, the decomposition-based distributed controller synthesis is shown to be applicable to the active control problem of the next generation telescopes. To apply the theory developed in [26] to the active control problem of the next generation telescopes, the performance index should be defined in such a way to allow decomposition by the pattern matrices that commute in multiplication. The objective of the active control of telescopes is to maintain the shape of the primary mirror against disturbances. In the next generation telescopes, the active control problem involves the alignment of the neighbouring segments. To capture this and to be compatible with the decomposition approach, instead of the edge point misalignments, the relative displacements of the actuation points can be taken as the output of the system. The relative displacements of the actuation points correspond to more than the half of the edge point misalignments. So the scaling filter $W_{zi} = 2 \times 10^7 \times I_3$ already accounts for this relation. In order to make use of the theory developed in [26], the output of the system is defined by using the Kronecker delta product.

The overall performance index z is defined as follows to make the output matrix decomposable:

$$z = I \otimes \begin{bmatrix} 0_3 \\ \tilde{z}_{2i} \end{bmatrix} + P \otimes \begin{bmatrix} \tilde{z}_{1i} \\ 0_3 \end{bmatrix}, \tag{7.1}$$

where I_{492} is a 492-by-492 identity matrix and each row of 492-by-492 matrix P_{492} satisfy the following:

$$P_{492}(i,j) = \begin{cases} k, & i = j \\ -1, & j \in N_i \\ 0, & otherwise \end{cases} \tag{7.2}$$

where $i \in \{1, 2, 3, \dots, 492\}$, k is the total number of neighbouring segments of the i^{th} segment, N_i is the list of these neighbouring segments of the i^{th} segment and $P_{492}(i,j)$ is the i^{th} row-j^{th} column entry of the matrix P_{492}. For $i = 1$, $N_1 = \{3,\ 4,\ 2,\ 84,\ 87\}$ and $k = 5$ whereas for $i = 30$, $N_{30} = \{38,\ 39,\ 31,\ 23,\ 22,\ 29\}$ and $k = 6$ (see Figure 7-1). With defining the pattern matrix P_{492} as a symmetric graph Laplacian matrix, the weighted supporting point positions of each segment are subtracted from the sum of the neighbouring segment supporting point positions that allows us to set the relative displacements as the performance index of the controller synthesis. After defining all the necessary equations, the overall state-space matrices can be calculated as:

$$\dot{x} = Ax + B_d d + B_u u, \tag{7.3}$$

$$z = C_z x + D_{zd} d + D_{zu} u, \tag{7.4}$$

$$y = C_y x + D_{yd} d + D_{yu} u. \tag{7.5}$$

where x, d, u, y are concatenated forms of 492 segment x_i, d_i, u_i, y_i signals and z is defined as in Eq. (7.1). Wind disturbance and noise signals are grouped into signal d_i that is defined as $d_i = [\widetilde{w}_i^T \quad n_i^T]^T$. Since in [26] the synthesis of a controller for a discrete-time system is considered, we discretized the above equation by using the zero-order hold with a sample time of 10^{-4} seconds. If we denote the discretization function as *c2d*, the discrete-time equivalent of system matrices can be represented as:

$$\hat{A}, \hat{B}, \hat{C}, \widehat{D} = c2d(A, B, C, D) \tag{7.6}$$

7.3 H$_\infty$ controller synthesis

In the controller synthesis, the roadmap presented in [26] is followed. In this approach the state-space matrices must be decomposable with one or more pattern matrices. Since we have defined our relative displacements in a decomposable form compatible with [26] it is possible to decompose the overall system matrices as follows:

$$\widehat{\mathbf{A}} = (S_{492} \otimes I_l)^{-1}\hat{A}(S_{492} \otimes I_l), \tag{7.7}$$

$$\widehat{\mathbf{B}}_{\mathbf{d}} = (S_{492} \otimes I_l)^{-1}\hat{B}_d\left(S_{492} \otimes I_{m_d}\right), \tag{7.8}$$

$$\widehat{\mathbf{B}}_{\mathbf{u}} = (S_{492} \otimes I_l)^{-1}\hat{B}_u\left(S_{492} \otimes I_{m_u}\right), \tag{7.9}$$

$$\hat{\mathbf{C}}_{\mathbf{z}} = \left(S_{492} \otimes I_{r_z}\right)^{-1}\hat{C}_z(S_{492} \otimes I_l), \tag{7.10}$$

$$\hat{\mathbf{C}}_{\mathbf{y}} = \left(S_{492} \otimes I_{r_y}\right)^{-1}\hat{C}_y(S_{492} \otimes I_l), \tag{7.11}$$

$$\widehat{\mathbf{D}}_{\mathbf{yd}} = \left(S_{492} \otimes I_{I_{r_y}}\right)^{-1}\widehat{D}_{yd}\left(S_{492} \otimes I_{m_d}\right), \tag{7.12}$$

$$\widehat{\mathbf{D}}_{\mathbf{yu}} = \left(S_{492} \otimes I_{r_y}\right)^{-1}\widehat{D}_{yu}\left(S_{492} \otimes I_{m_u}\right), \tag{7.13}$$

$$\widehat{\mathbf{D}}_{\mathbf{zd}} = \left(S_{492} \otimes I_{r_z}\right)^{-1}\widehat{D}_{zd}\left(S_{492} \otimes I_{m_d}\right), \tag{7.14}$$

$$\widehat{\mathbf{D}}_{\mathbf{zu}} = \left(S_{492} \otimes I_{r_z}\right)^{-1}\widehat{D}_{zu}\left(S_{492} \otimes I_{m_u}\right), \tag{7.15}$$

where $\widehat{\mathbf{A}}$, $\widehat{\mathbf{B}}_{\mathbf{d}}$, $\widehat{\mathbf{B}}_{\mathbf{u}}$, $\hat{\mathbf{C}}_{\mathbf{z}}$, $\hat{\mathbf{C}}_{\mathbf{y}}$, $\widehat{\mathbf{D}}_{\mathbf{yd}}$, $\widehat{\mathbf{D}}_{\mathbf{yu}}$, $\widehat{\mathbf{D}}_{\mathbf{zd}}$ and $\widehat{\mathbf{D}}_{\mathbf{zu}}$ are block diagonal and S is the matrix that diagonalizes P_{492} with $\Lambda_{492} = S_{492}^{-1}P_{492}S_{492}$. Each of the i^{th} block of a state-space matrix can be expressed as:

$$\widehat{\mathbf{A}}_{\mathbf{i}} = \hat{A}_1 + \lambda_i\hat{A}_2, \tag{7.16}$$

$$\widehat{\boldsymbol{B}}_{\boldsymbol{d}_{\mathbf{i}}} = \widehat{B}_{d_1} + \lambda_i\widehat{B}_{d_2}, \tag{7.17}$$

$$\widehat{\boldsymbol{B}}_{\boldsymbol{u}_{\mathbf{i}}} = \widehat{B}_{u_1} + \lambda_i\widehat{B}_{u_2}, \tag{7.18}$$

$$\widehat{\boldsymbol{C}}_{\boldsymbol{z}_{\mathbf{i}}} = \hat{C}_{z_1} + \lambda_i\hat{C}_{z_2}, \tag{7.19}$$

$$\widehat{\boldsymbol{C}}_{\boldsymbol{y}_{\mathbf{i}}} = \hat{C}_{y_1} + \lambda_i\hat{C}_{y_2}, \tag{7.20}$$

$$\widehat{\boldsymbol{D}}_{\boldsymbol{yd}_{\mathbf{i}}} = \widehat{D}_{yd_1} + \lambda_i\widehat{D}_{yd_2}, \tag{7.21}$$

$$\widehat{\boldsymbol{D}}_{\boldsymbol{yu}_{\mathbf{i}}} = \widehat{D}_{yu_1} + \lambda_i\widehat{D}_{yu_2}, \tag{7.22}$$

$$\widehat{\boldsymbol{D}}_{\boldsymbol{zd}_{\mathbf{i}}} = \widehat{D}_{zd_1} + \lambda_i\widehat{D}_{zd_2}, \tag{7.23}$$

$$\widehat{\boldsymbol{D}}_{\boldsymbol{zu}_{\mathbf{i}}} = \widehat{D}_{zu_1} + \lambda_i\widehat{D}_{zu_2}, \tag{7.24}$$

where λ_i is the i^{th} entry in the diagonal of Λ_{492}. In the transformed space, a controller for each independent block can be synthesized. By concatenating controller state-space matrices into global controller state-space matrices and by using the inverse transformation, a global controller could be calculated. However, this global controller might not have the same interconnection structure as the system. So in [26] it is shown that with additional constraints on the solution space, it is possible to synthesize a distributed controller that has the same interconnection pattern as the system. However, one should be careful of the system norms as the decomposition of the state space matrices affects the system norms. By further restricting the system norms according to the maximum and minimum singular of S_{492} the same objectives could be set as in the original controller synthesis. For the sake of concise publication readers are referred to [26] for the complete discussion of the synthesis and to Chapter 5 for the summary.

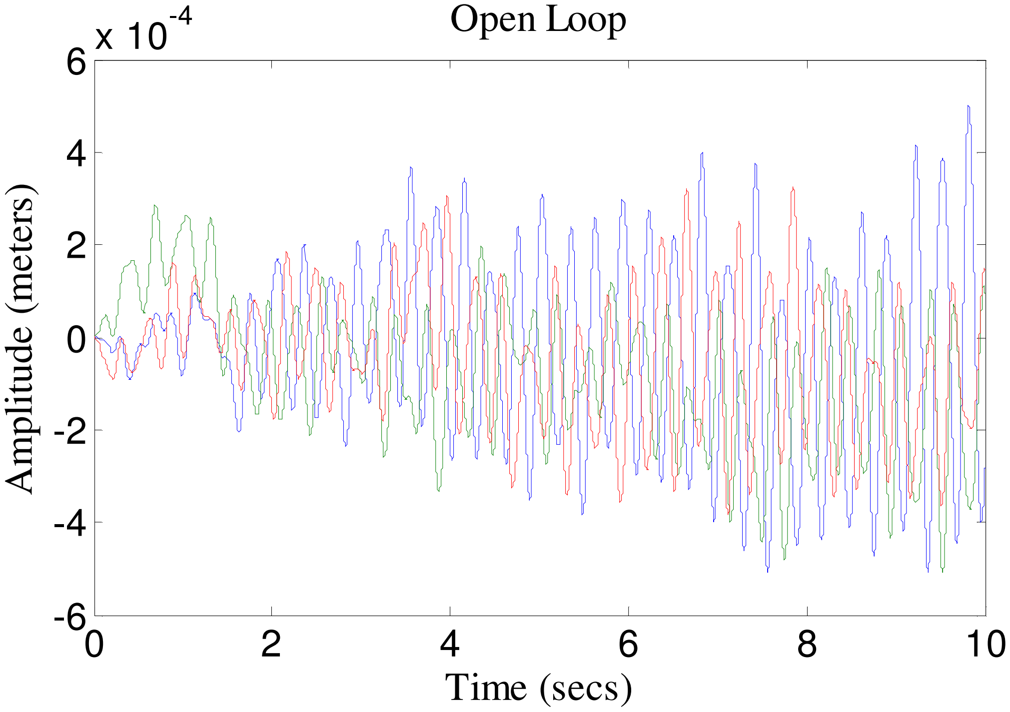

Figure 7-3. Sample relative displacement in the simulation of open-loop synthesis.

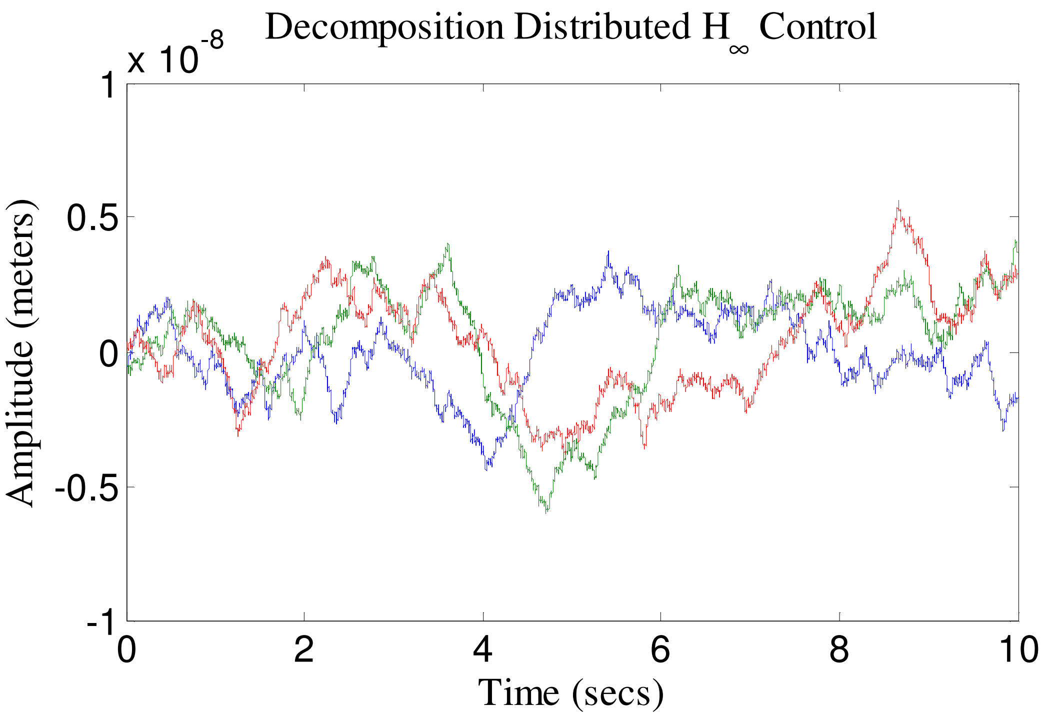

Figure 7-4. Sample relative displacements in the simulation of distributed H_∞ controller.

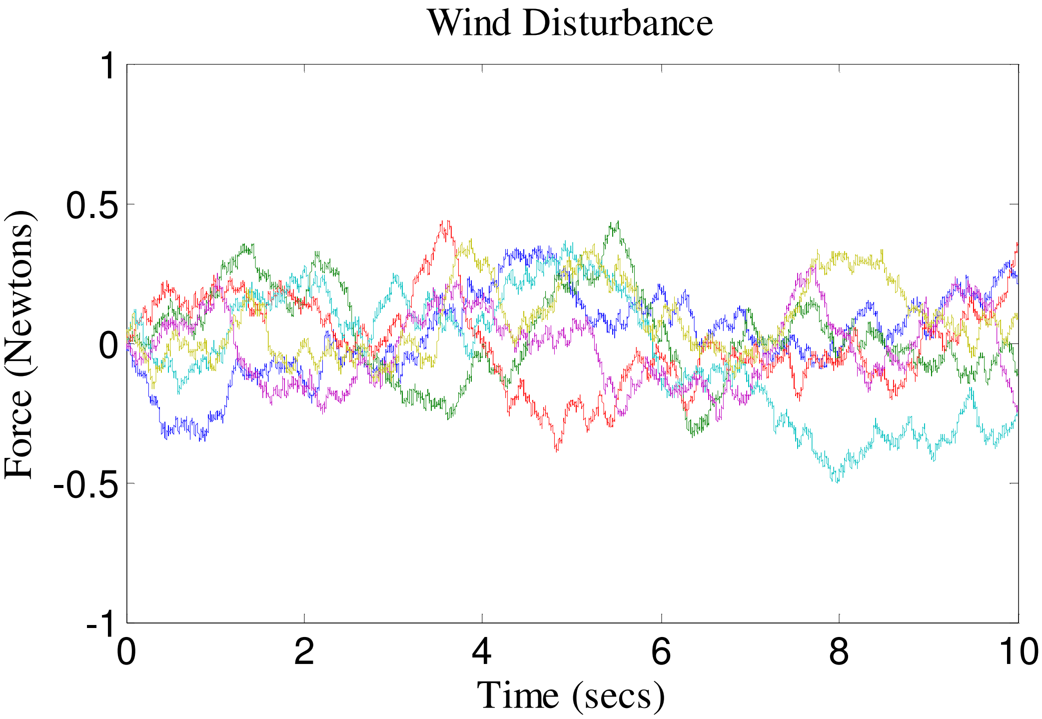

Figure 7-5. Sample simulated wind disturbances.

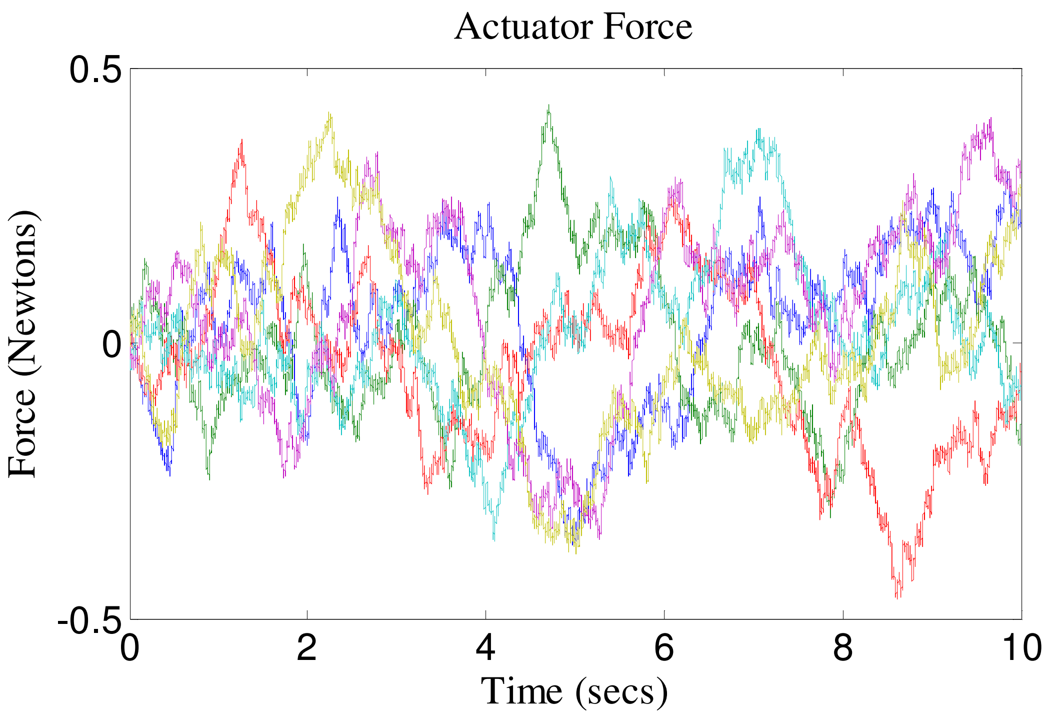

Figure 7-6. Sample actuator forces in the simulation of distributed H_∞ controller.

7.4 Simulation results

In order to test the performance of the controller, first a 492-segment dynamics is calculated by following the procedure described in Section 2.1. To apply the theory developed in [26], continuous time system is then converted to discrete-time by using the zero-order hold with a sample time of 10^{-4} seconds. After the conversion of the system to its discrete time equivalent, the design procedure described in Chapter 5 is followed, and a distributed controller that satisfies the imaging performance requirements and the control input restrictions is synthesized. Simulations are carried out in MatLab Simulink environment. Figures 7-3 and 7-4 show the relative segment displacements between the actuation point positions of the first segment and the neighbouring segment actuation point positions in the simulation of the open-loop and the closed-loop systems, respectively. As can be seen from the figures the sample relative displacement values of the closed-loop system are well below the rms value of 5×10^{-8} meters and are calculated as 1.56, 2.22, 2.02 nm. These results prove that the rms error contributed by the controller performance does not put any restriction to the observed image resolution since the optical telescope already works in its diffraction limit. Figure 7-5 shows the sample wind disturbances acting on the sample segments of the 492-segment system. As expected, the rms value of the sample wind disturbances are below 0.3 N and are calculated as 0.15 N, 0.17 N, 0.16 N, 0.23 N, 0.13 N, 0.15 N. In Figure 7-6, the values of the force supplied by the actuators are presented. From the graph, we can see that the actuator is indeed physically feasible as was set one of the objectives of the synthesis.

7.5 Conclusions

In this chapter, the decomposition-based H_∞ control of dynamically uncoupled large segmented mirrors is investigated. To increase the primary mirror size of the telescope further, segmented mirrors will be employed by the next generation telescopes. Some of the largest existing telescopes already use segmented mirrors as their primary mirrors to collect light. The success in the application of the segmented mirrors in the optical telescopes convinces designers to increase the primary mirror sizes drastically in the next generation telescope designs. Although with segmented mirrors it is possible to increase the size of the primary mirror, this increase will bring new challenges to the active control of the next generation telescope mirrors. Aligning segments to maintain the shape of the primary mirror can be achieved by using either a centralized or a distributed approach as the alignment of the neighbouring segments requires co-operation among the segment controllers. However the big leap in the size of the primary mirrors requires very large matrices to be handled by a central computing system that makes centralized approach troublesome with the current computing capabilities of computers. Distributed control, on the other hand, could achieve the same objectives by using simple computing units distributed spatially over the system. To synthesize a distributed controller, first a dynamically decoupled model is presented. Then, an output matrix is defined as a decomposable matrix that allows us to simplify the synthesis problem. After the calculation of the distributed controller, performance tests have been carried out by using 492-segment TMT-like system model in MatLab Simulink. The results show that the designed controller is physically feasible and does not put any restrictions on the image observed by the optical system as it already works in its diffraction limit. As a next step in our research, we will try to apply the same methodology to a dynamically coupled (i.e.

flexible support) system where control action at one segment can disturb the neighbouring segment dynamics.

8. FOURIER-BASED DISTRIBUTED H_∞ CONTROL OF DYNAMICALLY COUPLED LARGE SEGMENTED MIRRORS

In this chapter, the Fourier-based distributed H_∞ control of the dynamically coupled segmented primary mirror is investigated. Both spatially-invariant distributed and centralized H_∞ controllers are designed for a 7-segment proof-of-concept system model as described in Section 2.2. In our proposed mirror design, the segments are dynamically coupled through a uniform support structure, which is modelled using the finite element method. In addition, the segments have the coupled control objective of maintaining the overall mirror shape to allow the highest possible image resolution. A spatially-invariant distributed model is obtained by following Section 2.2. The resulting model is then used to synthesize a spatially-invariant distributed controller. The simulation results of the distributed controller is presented and compared with the results from the centralized H_∞ controller applied to the 7-segment system. It is shown that both centralized and spatially-invariant distributed controllers satisfy the imaging performance requirements. The main results of this chapter are published in [44].

8.1 Centralized H_∞ control

In this section, an H_∞ controller for the 7-segment system is designed. In section 3.1, we describe the synthesis procedure to obtain a stabilizing controller K, which satisfies our suboptimal objective of $\|T_{zw}\| < 1$ for the closed-loop system.

In order to meet the imaging performance requirements set in [2], and calculated in [31], a controller that achieves relative displacements of 10^{-8} m scale must be synthesized. To achieve this control objective, relative displacements from the system outputs need to be calculated. First, the absolute positions of the edge sensing points are determined via geometric calculations as in [31]:

$$y_{s_i} = \begin{bmatrix} 5/3 & -7/9 & 1/9 \\ 5/3 & 1/9 & -7/9 \\ 13/9 & 5/9 & -1 \\ 5/9 & 13/9 & -1 \\ 1/9 & 5/3 & -7/9 \\ -7/9 & 5/3 & 1/9 \\ -1 & 5/3 & 5/9 \\ -1 & 5/3 & 13/9 \\ -7/9 & 13/9 & 5/3 \\ 1/9 & -7/9 & 5/3 \\ 5/9 & -1 & 13/9 \\ 13/9 & -1 & 5/9 \end{bmatrix} y_i, \tag{8.1}$$

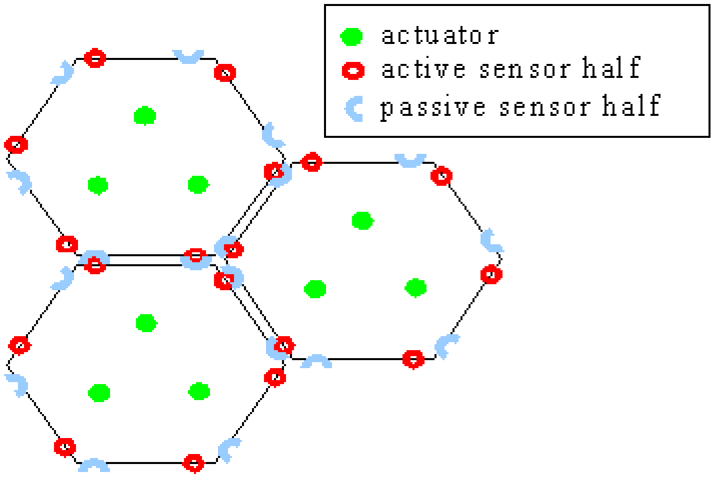

Figure 8-1. Geometric placements of sensors and actuators [25].

where $y_i \in R^3$ and $y_{Si} \in R^{12}$ are the vectors of the absolute positions of the supporting and sensing points of the i^{th} segment, respectively. Then, relative displacements are calculated by subtracting the absolute positions of the sensing points on the edges from the corresponding points of the neighbouring segments. The location of the edge sensing points and actuation points were previously shown in Figure 8-1. The relative displacements are then set to be the outputs of the system as follows:

$$z_{y_S} = C_m y, \tag{8.2}$$

where $C_m \in R^{84\times 21}$ maps the output vector y to the relative displacements $z_{y_S} \in R^{84}$, which is the output vector of the system that gives the relative displacements of the segments. Then, our system output with the scaling factor β for the controller synthesis becomes $z_x = \beta z_{y_S} = W_x y$. Since our synthesis assumes unit inputs, scaling of the disturbance input w and the control input u is necessary. For the disturbance scaling, as done in [31], we can adopt Von Karman model for the wind pressure power spectral density (PSD):

$$\Phi_{\mathrm{pt}}^{vK} = \frac{C_{pt}^{vK}}{\left[1+\left(\frac{f}{f_0}\right)^2\right]^{\frac{7}{6}}} \tag{8.3}$$

where $\mathrm{C}_{\mathrm{pt}}^{\mathrm{vK}}$ is the magnitude and f_0 is the bandwidth of the model. The values for the magnitude and the bandwidth of the model are determined to be 10 and $\frac{1}{2\pi}$ Hz, respectively [31]. A white noise filter of order two can be used to approximate the force disturbance due to the wind. With the help of least-squares estimation, white noise disturbance filter $W_{ni} = (0.01941s + 0.3043)/(0.1196s^2 + 1.32s + 1)$ for $i = \{i \in Z \mid 0 \leq i \ and\ i \leq 20\}$ can be obtained (see [31] for detailed derivation). The resulting disturbance scaling transfer matrix for the 7-segment system is then given by:

$$W = \begin{bmatrix} W_{n0} & & \\ & \ddots & \\ & & W_{n20} \end{bmatrix}. \tag{8.4}$$

For the control input scaling, we use a high-pass filter $W_{ui} = (s+1)/(s+1000)$ for each control channel to limit the bandwidth and the gain of the controller. As in the above disturbance filter, the input scaling transfer function matrix for the 7-segment system is defined as:

$$W = \begin{bmatrix} W_{u0} & & \\ & \ddots & \\ & & W_{u20} \end{bmatrix}. \tag{8.5}$$

Figure 8-2 shows the control system block diagram that is used for the centralized H∞ controller synthesis.

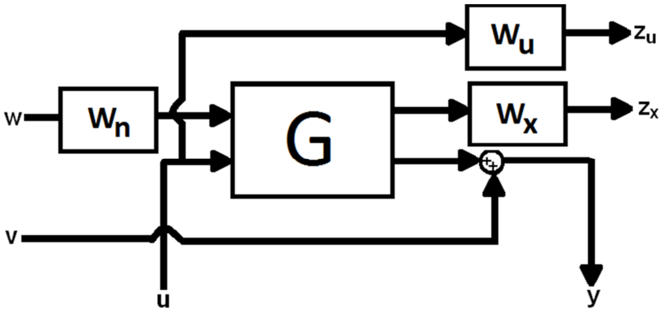

Figure 8-2. Control system block diagram for the centralized H∞ synthesis.

8.1.1 Simulation results

Our main goal, as mentioned in the previous sections, is to design a controller that achieves relative segmental displacements of in the orders of 10^{-8} m. In Figure 8-3, we show a simulation example of the inter-edge relative displacements for the open-loop system, in which the relative displacement amplitude reaches up to 1.5×10^{-6} m. Figure 8-4 shows the same displacements with the centralized H∞ controller activated, which shows a significant improvement. A sample force supplied by an actuator is also shown in Figure 8-5 for the corresponding simulation. Figure 8-6 shows the sensor noise level used in the simulation. As mentioned earlier, the Keck telescope sensor noise level is used in our simulations. Also, as expected, the average wind disturbance force is around 0.3N (see Figure 8-7).

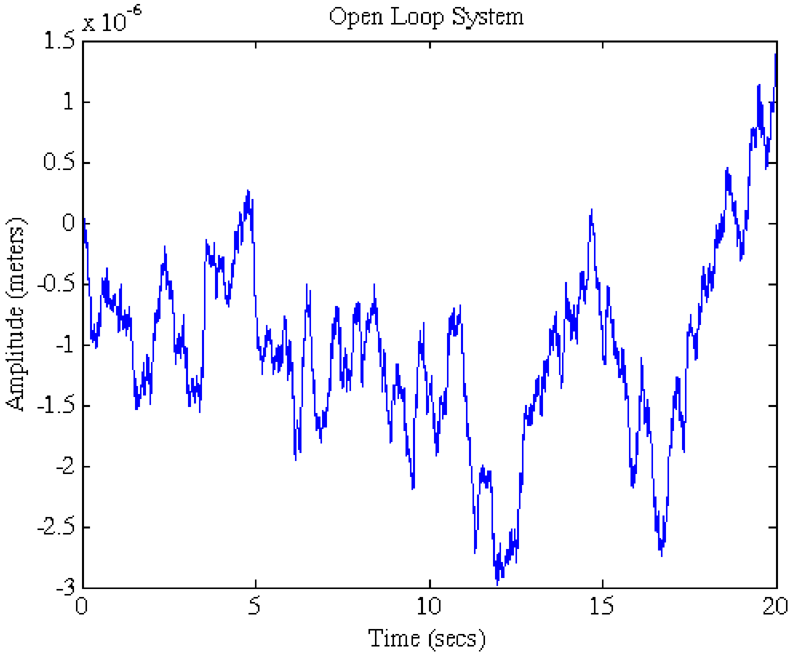

Figure 8-3. Relative edge displacement for the open-loop system.

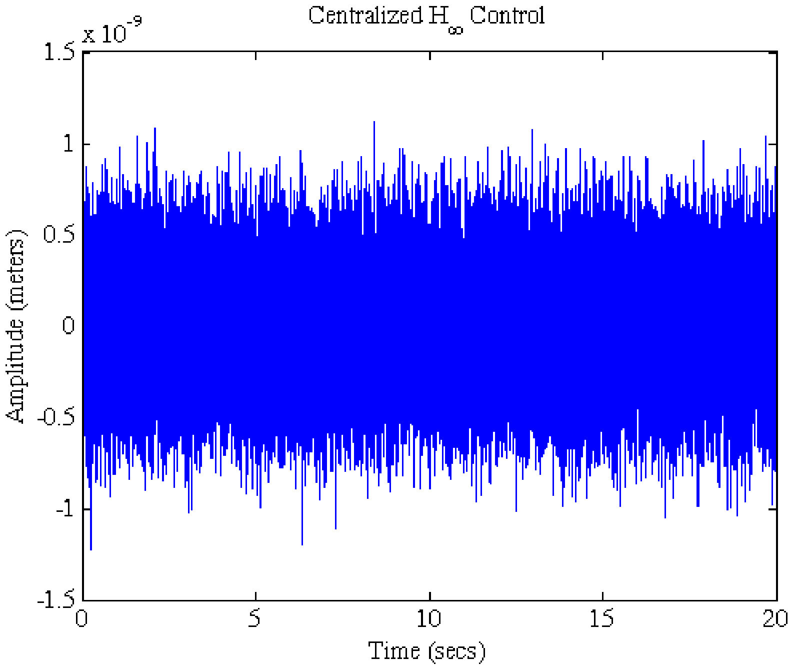

Figure 8-4. Simulation results for the centralized H_∞ control.

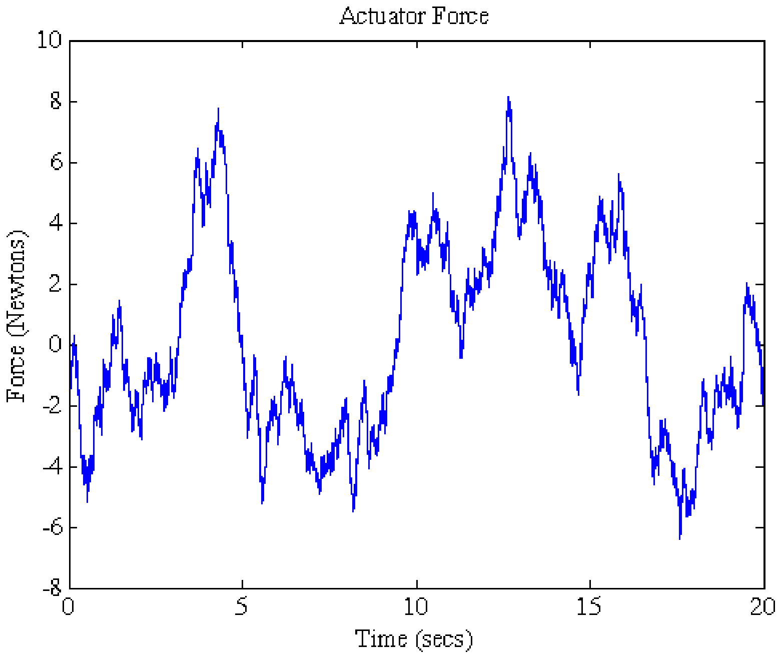

Figure 8-5. Supplied force by actuators used in the simulation of the centralized H_∞ control.

8.2 Spatially-invariant distributed H_∞ control

As described earlier, when the number of segments increases the centralized schemes become intractable and require too much computational power that is cost prohibitive. To overcome the drawbacks and to achieve the global performance requirement for the dynamically coupled segments, we apply a distributed control scheme proposed in [24] to the H_∞ synthesis procedure described in the Section 3.1.

In order to apply the distributed control scheme of [24], first, the spatial-invariance in our system needs to be defined. In Figure 8-8, three spatial directions are shown. The system is spatially-invariant under the translation operators S_1, S_2 and S_3 corresponding to each spatial direction. Some useful examples of spatial operations are $y_1 = S_1 y_0$, $y_4 = S_1^{-1} y_0$, and $A_1 = S_1 A_0$. Notice that, these operators are geometrically symmetric, i.e. $S_i S_j S_k = 1$ for different i, j and k.

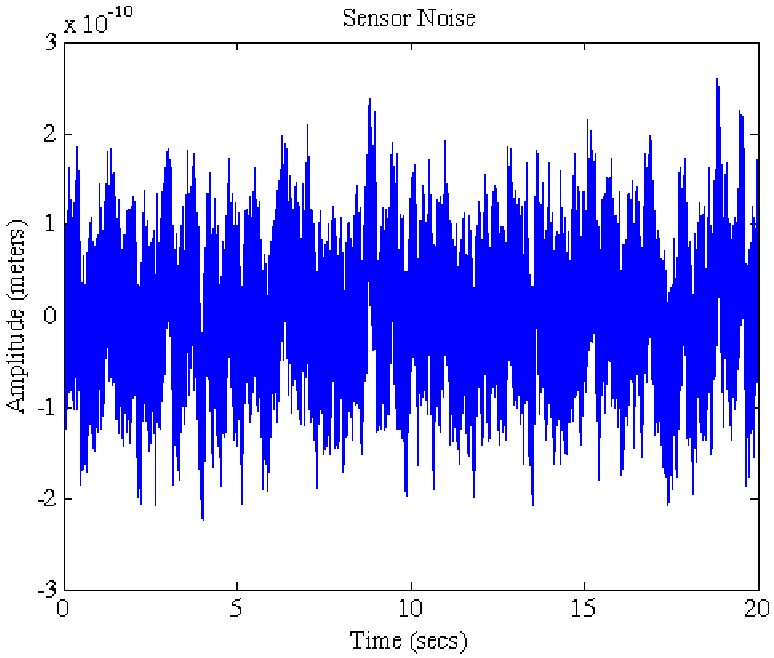

Figure 8-6. Sensor noise in feedback reading.

8.2.1 Shift operator in the output equation

In order to incorporate the relative displacements to the distributed model of one segment, the above shift operators can be used in the output equation to obtain:

$$z_i = \begin{bmatrix} -S_1 - \frac{5}{3} & \frac{5}{9}S_1 + \frac{7}{9} & \frac{13}{9}S_1 - \frac{1}{9} \\ -S_1 - \frac{5}{3} & \frac{13}{9}S_1 - \frac{1}{9} & \frac{5}{9}S_1 + \frac{7}{9} \\ \frac{13}{9}S_2 - \frac{1}{9} & -S_2 - \frac{5}{3} & \frac{5}{9}S_2 + \frac{7}{9} \\ \frac{5}{9}S_2 + \frac{7}{9} & -S_2 - \frac{5}{3} & \frac{13}{9}S_2 - \frac{1}{9} \\ \frac{5}{9}S_3 + \frac{7}{9} & \frac{13}{9}S_3 - \frac{1}{9} & -S_3 - \frac{5}{3} \\ \frac{13}{9}S_3 - \frac{1}{9} & \frac{5}{9}S_3 + \frac{7}{9} & -S_3 - \frac{5}{3} \end{bmatrix} y_i = [C_{zi}]y_i \tag{8.6}$$

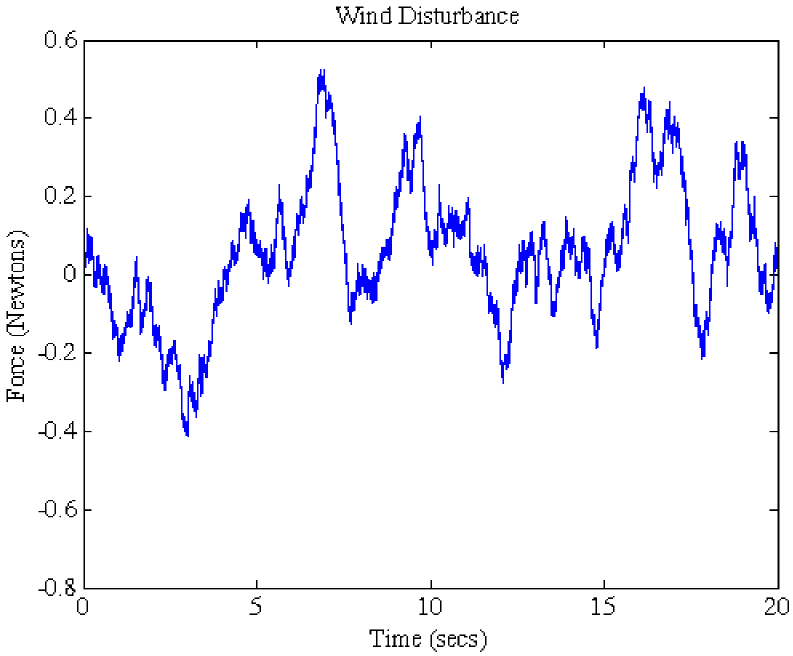

Figure 8-7. Wind disturbance in simulations.

As in the centralized scheme, the same scaling matrices (with the reduction of their sizes to $R^{3\times 3}$) are used and the output scaling matrix $W_x = \gamma C_{zi}$, where γ is a weighting value, which only includes the relative displacements. The overall control system block diagram representation that is used in the distributed control synthesis with the inclusion of the scaling matrices attached is similar to that of Figure 8-2.

8.2.2 Shift operator in the distributed model

The shift operators are not only used to define the relative displacements, but also to define the structural interactions among the segments. Eq. (2.6) can be simplified, by using the following relations from [25]:

$$p_+(s+1) = r_+(s) \tag{8.7}$$

$$p_-(s-1) = r_-(s) \tag{8.8}$$

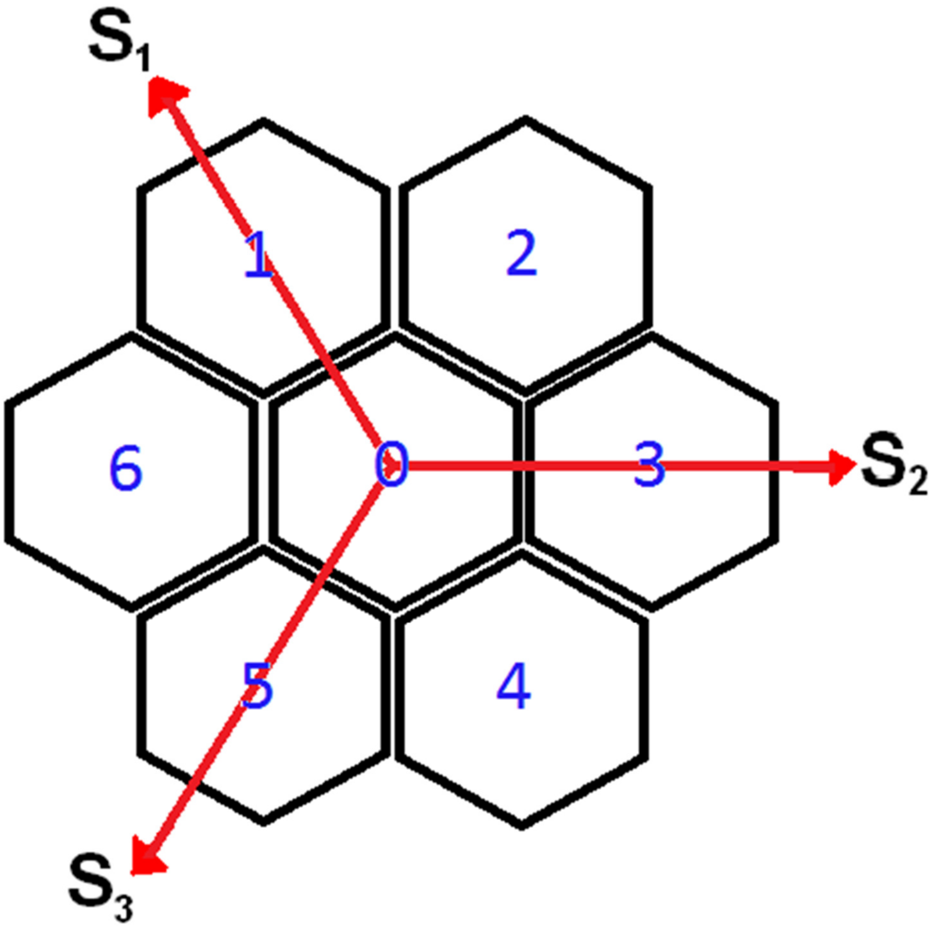

Figure 8-8. Spatial shift directions for the 7-segment system.

where s is a spatial variable and, p and r are the interconnection input and output signals respectively. Shift operators can be put at the diagonal entries of the shift matrix as follows:

$$\Delta_{S,m} = \begin{bmatrix} S_1 I_{m_1} & & & & & \\ & S_1^{-1} I_{m_{-1}} & & & & \\ & & S_2 I_{m_2} & & & \\ & & & S_2^{-1} I_{m_{-2}} & & \\ & & & & S_3 I_{m_3} & \\ & & & & & S_3^{-1} I_{m_{-3}} \end{bmatrix}, \tag{8.9}$$

where m_1, m_{-1}, m_2, m_{-2}, m_3, m_{-3} are the sizes of the interconnection signals.

By using the shift matrix, Eq. (2.6) can be rearranged as:

$$\dot{x}_i = \mathbf{A}x_i + \mathbf{B_1}w_i + \mathbf{B_2}u_i, \tag{8.10}$$

$$y_i = \mathbf{C}x_i + \mathbf{D_1}w_i + \mathbf{D_2}u_i, \tag{8.11}$$

where

$$\begin{bmatrix} \mathbf{A} & \mathbf{B_1} & \mathbf{B_2} \\ \mathbf{C} & \mathbf{D_1} & \mathbf{D_2} \end{bmatrix} = \begin{bmatrix} A_{TT} & B_{Tw} & B_{Tu} \\ C_T & D_w & D_u \end{bmatrix} + \begin{bmatrix} A_{TS} \\ C_S \end{bmatrix} (\Delta_{S,m} - A_{SS})^{-1} \begin{bmatrix} A_{ST} \\ B_{Sw} \\ B_{Su} \end{bmatrix}. \tag{8.12}$$

8.2.3 Synthesis

The shift operators in both the output and dynamics equations can be grouped into a single state-space form as follows:

$$\dot{x}_i = \mathbf{A}x_i + \mathbf{B_1}w_i + \mathbf{B_2}u_i, \tag{8.13}$$

$$z_i = \mathbf{C_{rel}}x_i, \tag{8.14}$$

$$y_i = \mathbf{C}x_i + \mathbf{D_1}w_i + \mathbf{D_2}u_i, \tag{8.15}$$

where $\mathbf{C_{rel}} = C_{zi}C_T$. Then, as described in [24], we can perform the Fourier transform to put the system into the following decoupled form:

$$\frac{\partial \check{x}_i}{\partial t} = \check{\mathbf{A}}\check{x} + \check{\mathbf{B}}_{\mathbf{1}}\check{w}_i + \check{\mathbf{B}}_{\mathbf{2}}\check{u}_i, \tag{8.16}$$

$$\check{z}_i = \check{\mathbf{C}}_{\mathbf{rel}}\check{x}_i, \tag{8.17}$$

$$\check{y}_i = \check{\mathbf{C}}\check{x}_i + \check{\mathbf{D}}_{\mathbf{1}}\check{w}_i + \check{\mathbf{D}}_{\mathbf{2}}\check{u}_i, \tag{8.18}$$

By going through the design steps from section 3.1, one can obtain a controller in the Fourier domain. Although by calculating the inverse Fourier of the designed controller, a spatially-invariant distributed controller could be determined, calculating the inverse Fourier is not trivial and possibly includes infinite degree in the shift operators. However, since, as described in [24], the convolution kernels have exponential rates of decay, by approximating the shift operator in terms of finite neighbouring units, such a controller can be approximated. By limiting the communication to the first neighbouring segments, the state-space matrices of the distributed controller can be approximated by least-squares estimation. In this case, the state-space matrices take the following form:

$$A_K(S) = A_{K0} + A_{K1}S_1 + A_{K2}S_2 + A_{K3}S_3 + A_{K4}S_1^{-1} + A_{K5}S_2^{-1} + A_{K6}S_3^{-1}, \tag{8.19}$$

$$B_K(S) = B_{K0} + B_{K1}S_1 + B_{K2}S_2 + B_{K3}S_3 + B_{K4}S_1^{-1} + B_{K5}S_2^{-1} + B_{K6}S_3^{-1}, \tag{8.20}$$

$$C_K(S) = C_{K0} + C_{K1}S_1 + C_{K2}S_2 + C_{K3}S_3 + C_{K4}S_1^{-1} + C_{K5}S_2^{-1} + C_{K6}S_3^{-1}, \tag{8.21}$$

$$D_K(S) = D_{K0} + D_{K1}S_1 + D_{K2}S_2 + D_{K3}S_3 + D_{K4}S_1^{-1} + D_{K5}S_2^{-1} + D_{K6}S_3^{-1}. \tag{8.22}$$

By gridding the Fourier frequencies and following the design procedure in section 3.1, the exact solutions of the matrices at frequency domain can be calculated. At the $m^{th} = [\theta_{1m} \quad \theta_{2m} \quad \theta_{3m}]$ gridding point, approximation becomes:

$$\begin{aligned} A_{K_m} \cong{}& A_{K0} + A_{K1}I_n e^{j\theta_{1m}} + A_{K2}I_n e^{j\theta_{2m}} + A_{K3}I_n e^{j\theta_{3m}} \\ &+ A_{K4}I_n e^{-j\theta_{1m}} + A_{K5}I_n e^{-j\theta_{2m}} + A_{K6}I_n e^{-j\theta_{3m}} \end{aligned} \tag{8.23}$$

$$\begin{aligned} B_{K_m} \cong{}& B_{K0} + B_{K1}I_n e^{j\theta_{1m}} + B_{K2}I_n e^{j\theta_{2m}} + B_{K3}I_n e^{j\theta_{3m}} \\ &+ B_{K4}I_n e^{-j\theta_{1m}} + B_{K5}I_n e^{-j\theta_{2m}} + B_{K6}I_n e^{-j\theta_{3m}} \end{aligned} \tag{8.24}$$

$$\begin{aligned} C_{K_m} \cong{}& C_{K0} + C_{K1}I_n e^{j\theta_{1m}} + C_{K2}I_n e^{j\theta_{2m}} + C_{K3}I_n e^{j\theta_{3m}} \\ &+ C_{K4}I_n e^{-j\theta_{1m}} + C_{K5}I_n e^{-j\theta_{2m}} + C_{K6}I_n e^{-j\theta_{3m}} \end{aligned} \tag{8.25}$$

$$\begin{aligned} D_{K_m} \cong{}& D_{K0} + D_{K1}I_n e^{j\theta_{1m}} + D_{K2}I_n e^{j\theta_{2m}} + D_{K3}I_n e^{j\theta_{3m}} \\ &+ D_{K4}I_n e^{-j\theta_{1m}} + D_{K5}I_n e^{-j\theta_{2m}} + D_{K6}I_n e^{-j\theta_{3m}} \end{aligned} \tag{8.26}$$

After getting values from enough gridding points and by using least-squares estimation, all coefficients for the shift operators in the controller state matrices can be determined. The designed controller has the following state-space form:

$$\begin{aligned}\dot{x} = (&A_{K0} + A_{K1}S_1 + A_{K2}S_2 + A_{K3}S_3 + A_{K4}S_1^{-1} + A_{K4}S_2^{-1}\\ &+ A_{K4}S_3^{-1})x\\ &+ (B_{K0} + B_{K1}S_1 + B_{K2}S_2 + B_{K3}S_3 + B_{K4}S_1^{-1}\\ &+ B_{K4}S_2^{-1} + B_{K4}S_3^{-1})y,\end{aligned} \tag{8.27}$$

$$\begin{aligned}u = (&C_{K0} + C_{K1}S_1 + C_{K2}S_2 + C_{K3}S_3 + C_{K4}S_1^{-1} + C_{K4}S_2^{-1} + C_{K4}S_3^{-1})x\\ &+ (D_{K0} + D_{K1}S_1 + D_{K2}S_2 + D_{K3}S_3 + D_{K4}S_1^{-1}\\ &+ D_{K4}S_2^{-1} + D_{K4}S_3^{-1})y.\end{aligned} \tag{8.28}$$

Notice that the controller needs both the controller states and the outputs of the neighbouring segments.

8.2.4 Simulation results

As in the centralized scheme, the 7-segment system model is used for the simulations. The results show that the relative displacements of the inter-edge points can be kept in the 10^{-8} m order as set by the imaging requirements. Sample relative inter-edge displacements are shown in Figure 8-9. In comparison to the centralized scheme, the relative displacements in the distributed H_∞ control show small amplitude oscillations. These gross oscillations are the direct result of the controller truncation due to the implementation of the proposed distributed controller. Since only the information from the nearest neighbouring segments is used in our design, as the number of segments increased further (e.g., by adding a second ring or a third ring as we have previously done in [41]). The relative displacements would still lie around 10^{-8} m as set by the control objective. A sample force supplied by an actuator is shown in Figure 8-10. Figure 8-11, 8-12 and 8-13 show the Simulink models used for the simulation of the distributed closed-loop system.

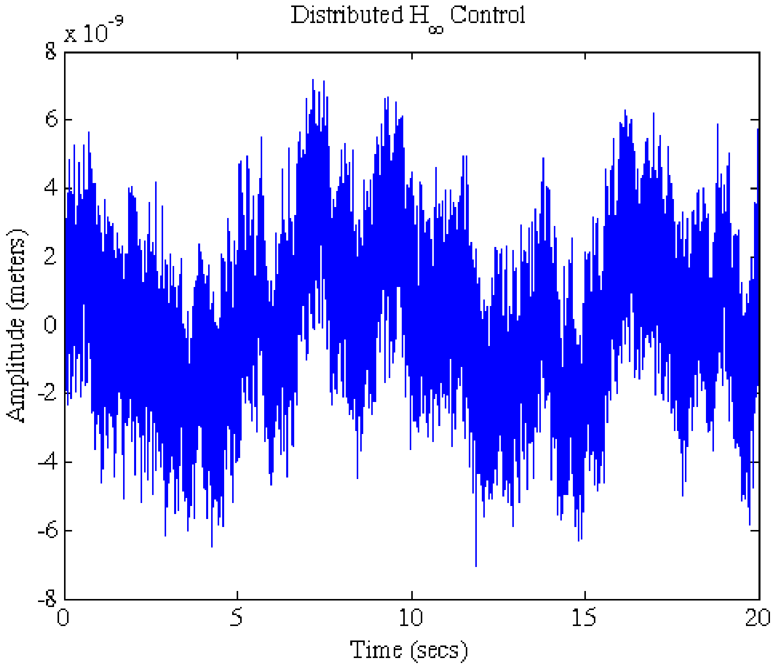

Figure 8-9. Simulation results for the distributed H_∞ control.

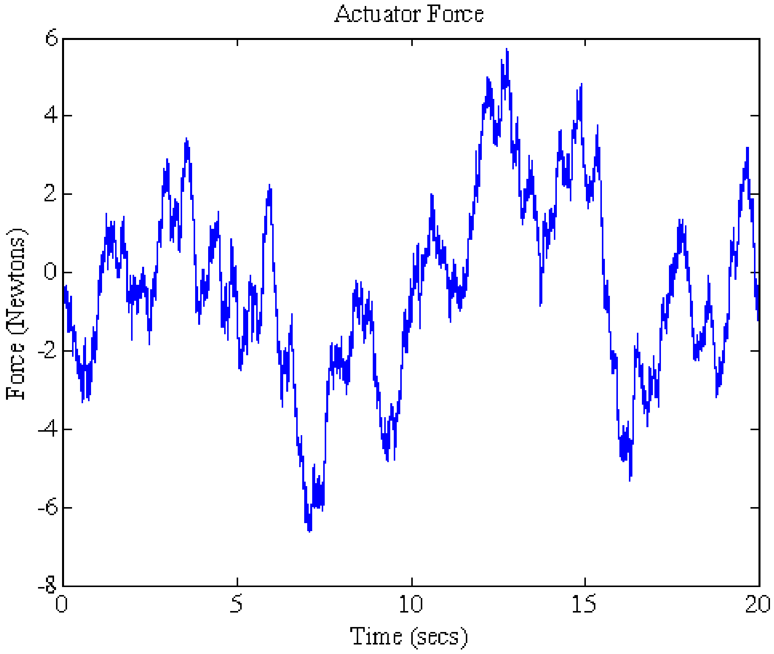

Figure 8-10. Supplied force by actuators used in the simulation of the distributed H_∞ control.

8.3 Conclusion

In this chapter, H_∞ control of dynamically coupled large segmented mirrors is investigated. As the number of segments increases the control of the telescope becomes a challenging task. Centralized control schemes require time consuming computations, which make them infeasible considering the control bandwidth requirements and the current computation power of computers. Decentralized control schemes are easier to implement, but they generally lack global performance objectives. A networked distributed control scheme is a compromise and can be tuned between the two extremes according to the control objectives. To evaluate our controller performance, 7-segment proof-of-concept is modelled in a dynamically coupled way via FEM. In addition to the dynamic interactions between the segments, the global objective of keeping relative displacement small also requires cooperation among the segments. Both spatially-invariant distributed and centralized controllers are synthesized for the modelled unit. The simulation results for both controllers are shown to satisfy the imaging performance requirements set by previous works. One should keep in mind that the centralized control problem requires more computation power as the number of segments increases. However, spatially-invariant distributed control problem is independent from the number of segments in the design.

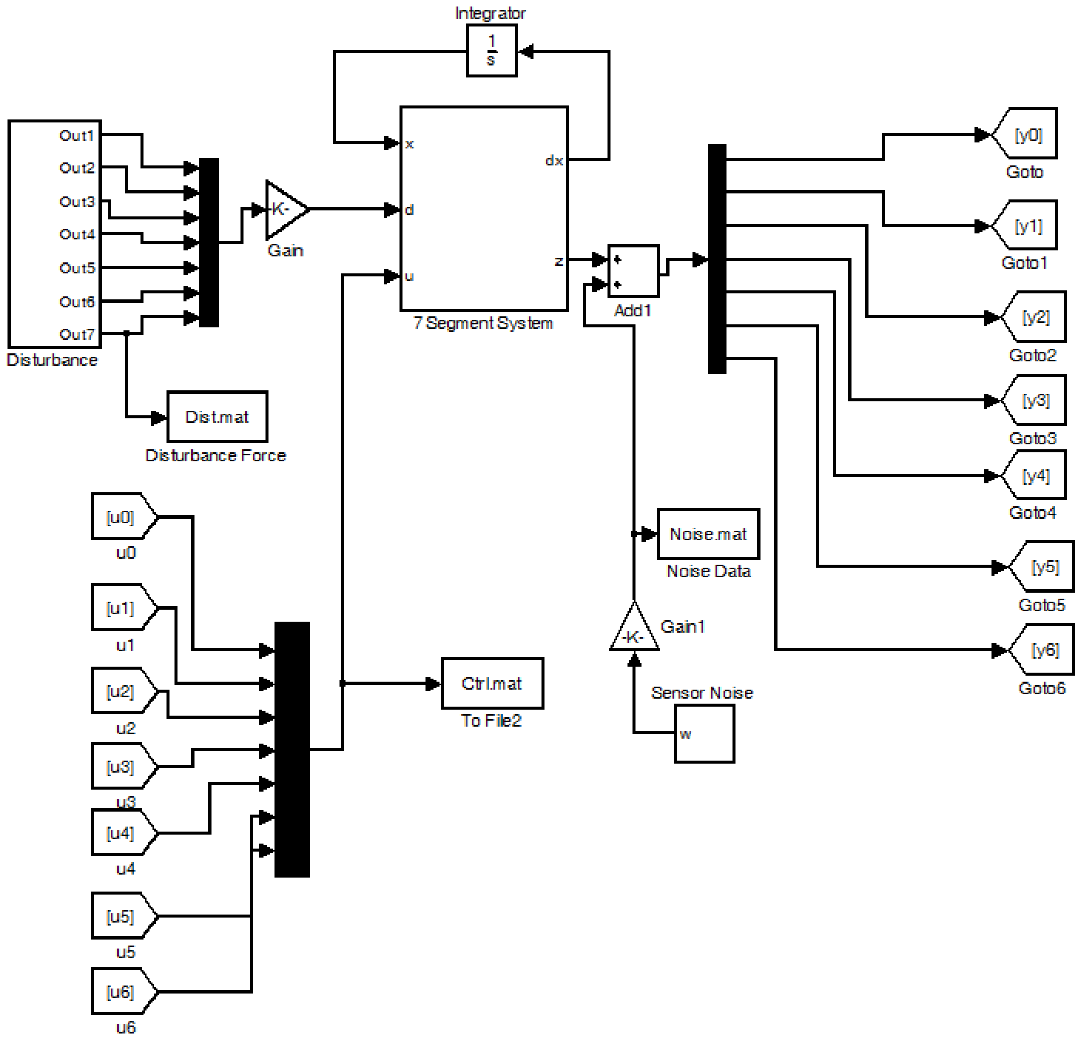

Figure 8-11. Seven segment plant model.

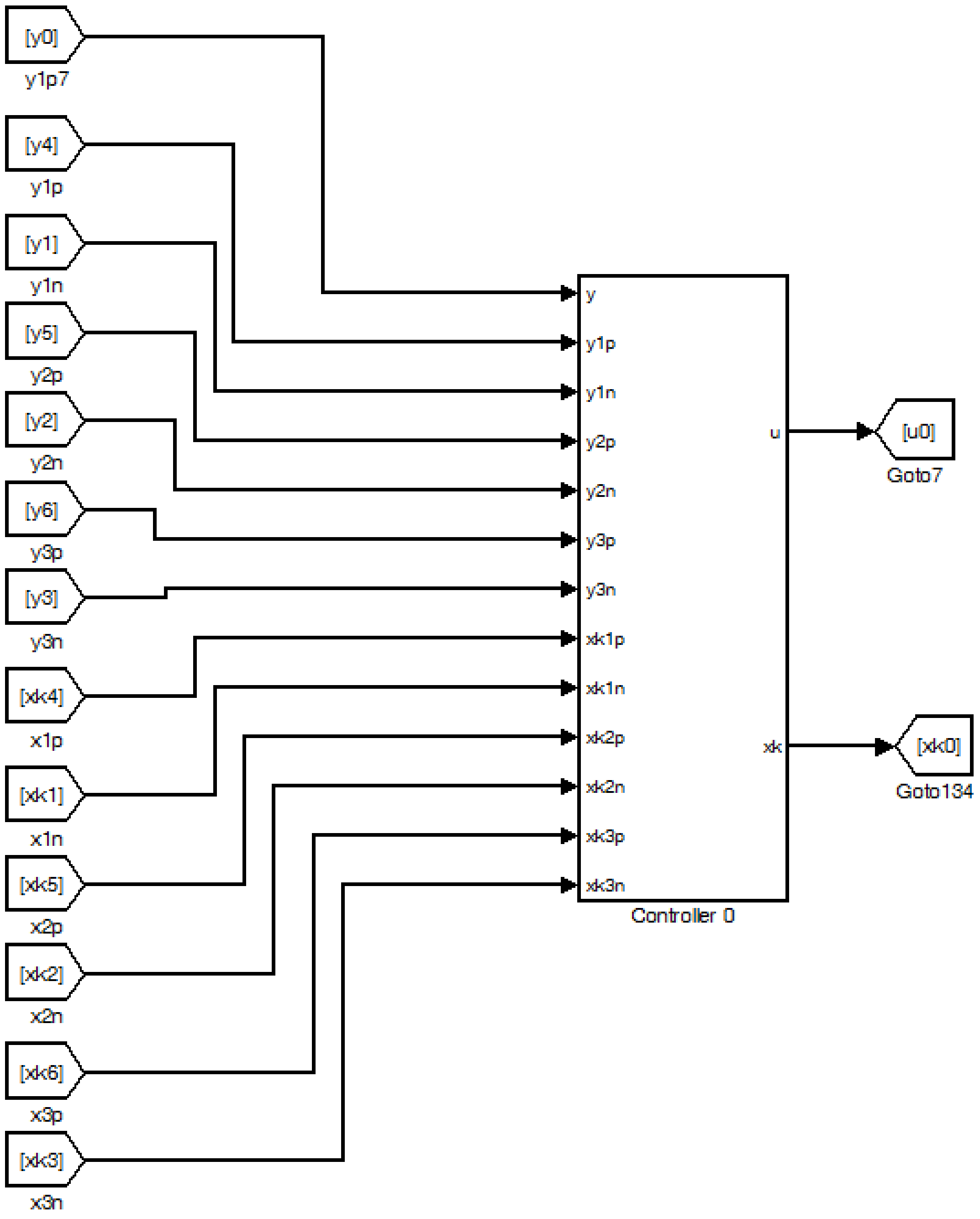

Figure 8-12. Individual distributed controller with spatial connections.

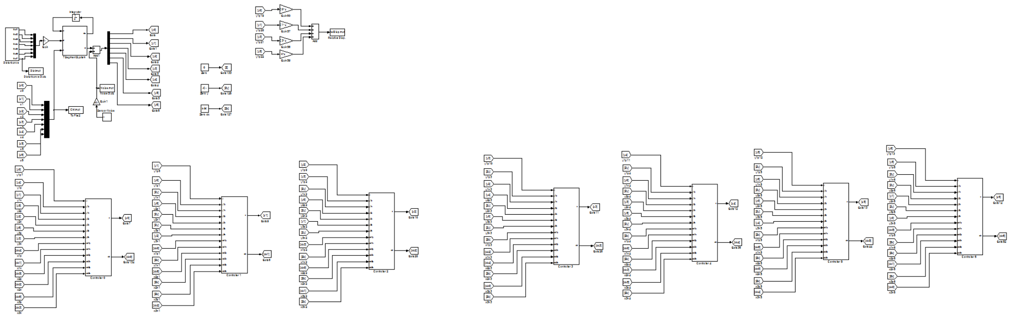

Figure 8-13. Overall system with 7 distributed controllers.

9. LMI-BASED DISTRIBUTED H_∞ CONTROL OF DYNAMICALLY COUPLED LARGE SEGMENTED MIRRORS

In this chapter, LMI-based H_∞ distributed control of dynamically coupled segments is investigated.

Segmented mirrors are to be used in the next generation of ground-based optical telescopes to increase the size of the primary mirror. A larger primary mirror enables the collection of more light, which results in higher image resolutions. The main reason behind the choice of segmented mirrors over monolithic mirrors is to reduce manufacturing, transportation, and maintenance costs of the overall system. Although segmented mirrors reduce the cost, they bring new challenges to the telescope control problem. The objective of keeping the mirror segments, which are dynamically coupled through a common support structure, aligned requires co-operation among individual segment controllers to maintain a smooth overall mirror surface. The vast number of inputs and outputs make the computations for centralized control schemes intractable. Any centralized controller employed also results in a system that is vulnerable to a complete system failure due to a malfunction of the controller. This chapter investigates the linear matrix inequality (LMI)-based distributed H_∞ control of dynamically coupled large segmented telescope mirrors. First, the distributed model in Section 2.2 will be used to design a distributed controller by using the LMI approach. Closed-loop simulations of a 492-segment system (in line with the Thirty Meter Telescope model) with the synthesized controller are run, and it is shown that the LMI-based distributed H_∞ controller can satisfy the stringent imaging performance requirements. The results of this chapter are published in [45].

9.1 Setting up the model for synthesis

9.1.1 Performance index coupling among segments

After the distributed dynamic model of a single candidate segment is obtained as in Section 2.2, the performance index coupling with its neighbouring segments needs to be defined. In order to set the relative displacements (i.e. the displacements of the edge points on a single segment with respect to the corresponding edge points on the neighbouring segments) as the individual system output for minimization, the absolute positions of the actuation points of the neighbouring segments must be augmented to the spatial inputs and outputs from the dynamic equation (see Eq. (2.6)). The augmented state-space representation of a single segment for controller synthesis with the performance index $z_i^G \in R^{12}$ as the output can be arranged as follows:

$$\begin{bmatrix} \dot{x}_i^G \\ r_i^G \\ z_i^G \\ y_i^G \end{bmatrix} = \begin{bmatrix} A_{TT}^G & A_{TS}^G & B_{Tw}^G & B_{Tu}^G \\ A_{ST}^G & A_{SS}^G & B_{Sw}^G & B_{Su}^G \\ C_{zT}^G & C_{zS}^G & D_{zw}^G & D_{zu}^G \\ C_{yT}^G & C_{yS}^G & D_{yw}^G & D_{yu}^G \end{bmatrix} \begin{bmatrix} x_i^G \\ p_i^G \\ w_i^G \\ u_i^G \end{bmatrix} \tag{9.1}$$

where $A_{TT}^G = A_{TT} \in R^{l\times l}$, $B_{Tw}^G = B_{Tw} \in R^{l\times 3}$, $B_{Tu}^G = B_{Tu} \in R^{l\times 3}$, $C_{yT}^G = C_T \in R^{3\times l}$, $D_{yw}^G = D_w \in R^{3\times 3}$, $D_{yu}^G = D_u \in R^{3\times 3}$, $x_i^G = x_i \in R^l$, $w_i^G = w_i \in R^3$, $u_i^G = u_i \in R^3$. As mentioned previously, the spatial inputs are augmented with absolute positions of neighbouring segment actuation points and take the following form:

$$\begin{aligned} p_i^G = \big[& S_1{}^{-1} y_i{}^T \, (\tilde{p}_i^1)^T \, S_2{}^{-1} y_i{}^T \, (\tilde{p}_i^2)^T \, S_3{}^{-1} y_i{}^T \, (\tilde{p}_i^3)^T \\ & S_1 y_i{}^T \, (\tilde{p}_i^4)^T \, S_2 y_i{}^T \, (\tilde{p}_i^5)^T \, S_3 y_i{}^T \, (\tilde{p}_i^6)^T \big]^T, \end{aligned} \tag{9.2}$$

where $\tilde{p}_i^* \in R^{m\times 1}$, *m* being the size of the spatial input and output in one spatial direction and superscript *T* representing the transpose of a matrix and

$$p_i = [(\tilde{p}_i^1)^T \quad (\tilde{p}_i^2)^T \quad (\tilde{p}_i^3)^T \quad (\tilde{p}_i^4)^T \quad (\tilde{p}_i^5)^T \quad (\tilde{p}_i^6)^T]^T \tag{9.3}$$

Firstly, to achieve the augmentation without affecting the dynamic equation, zero matrices should be added to the A_{TS} matrix as follows:

$$A_{TS}^{G} = [0_{l\times 3}\ \ \tilde{A}_{TS}^{1}\ \ 0_{l\times 3}\ \ \tilde{A}_{TS}^{2}\ \ 0_{l\times 3}\ \ \tilde{A}_{TS}^{3}\ \ 0_{l\times 3}\ \ \tilde{A}_{TS}^{4}\ \ 0_{l\times 3}\ \ \tilde{A}_{TS}^{5}\ \ 0_{l\times 3}\ \ \tilde{A}_{TS}^{6}] \tag{9.4}$$

where $\tilde{A}_{TS}^{*} \in R^{\boldsymbol{l\times m}}$ and

$$A_{TS} = [\tilde{A}_{TS}^{1}\quad \tilde{A}_{TS}^{2}\quad \tilde{A}_{TS}^{3}\quad \tilde{A}_{TS}^{4}\quad \tilde{A}_{TS}^{5}\quad \tilde{A}_{TS}^{6}] \tag{9.5}$$

Moreover, in order to send the absolute positions of segment actuation points to the neighbouring segments, A_{ST} matrix should be modified as follows:

$$\begin{gathered} A_{ST}^{G} = [{C_T}^{T}\ \ (\tilde{A}_{ST}^{1})^{T}\ \ {C_T}^{T}\ \ (\tilde{A}_{ST}^{2})^{T}\ \ {C_T}^{T}\ \ (\tilde{A}_{ST}^{3})^{T} \\ {C_T}^{T}\ \ (\tilde{A}_{ST}^{4})^{T}\ \ {C_T}^{T}\ \ (\tilde{A}_{ST}^{5})^{T}\ \ {C_T}^{T}\ \ (\tilde{A}_{ST}^{6})^{T}]^{T} \end{gathered} \tag{9.6}$$

where $\tilde{A}_{ST}^{*} \in R^{m\times l}$ and

$$A_{ST} = [(\tilde{A}_{ST}^{1})^{T}\quad (\tilde{A}_{ST}^{2})^{T}\quad (\tilde{A}_{ST}^{3})^{T}\quad (\tilde{A}_{ST}^{4})^{T}\quad (\tilde{A}_{ST}^{5})^{T}\quad (\tilde{A}_{ST}^{6})^{T}]^{T} \tag{9.7}$$

Also, note that $A_{SS}^{G} = 0_{(6m+18)\times(6m+18)}$ since $A_{SS} = 0_{6m\times 6m}$. The same resizing principle applies to B_{Sw}, B_{Su} and C_S as all matrices equal to a zero matrix with appropriate sizes.

To set the relative displacements as system output, C_{zT}^{G} and C_{zS}^{G} are modified. Before modification of the matrices, the system output can be represented with shift operations as follows:

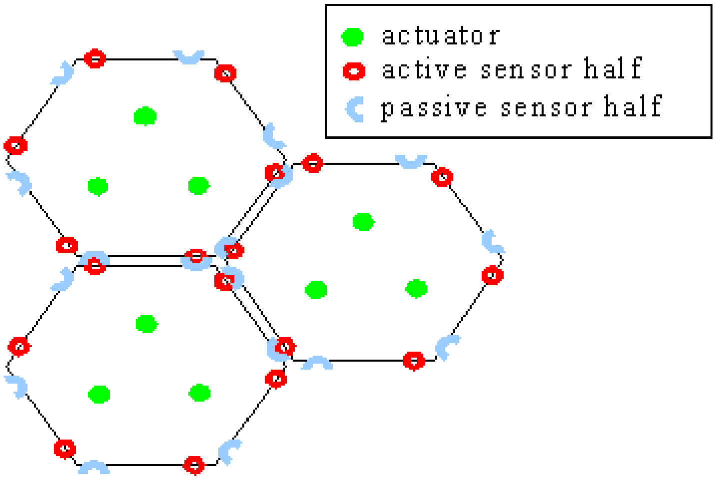

Figure 9-1. Geometric placements of sensors and actuators on the proposed TMT.

$$z_i = C_r y_i - (C_{S_1^{-1}} {S_1}^{-1} y_i + C_{S_2^{-1}} {S_2}^{-1} y_i + C_{S_3^{-1}} {S_3}^{-1} y_i + C_{S_1} S_1 y_i \\ + C_{S_2} S_2 y_i + C_{S_3} S_3 y_i) \tag{9.8}$$

where $C_r \in R^{12\times3}$, $C_{S_*} \in R^{12\times3}$, $C_{S_*^{-1}} \in R^{12\times3}$ map the absolute position of actuation points to the edge sensing points shown in Figure 9-1. C_{S_*} and $C_{S_*^{-1}}$ only map the absolute positions of actuation points of neighbouring segments to the corresponding edge points that are located across the inter-edge of the i^{th} segment sensing points, for example,

$$C_{S_1} = \begin{bmatrix} C_{rS_1} \\ \mathbf{0}_{9\times3} \end{bmatrix} \tag{9.9}$$

where

$$C_{rS_1} = \begin{bmatrix} -1 & \frac{5}{9} & \frac{13}{9} \\ -1 & \frac{13}{9} & \frac{5}{9} \\ 0 & 0 & 0 \end{bmatrix} \tag{9.10}$$

Since the neighbouring segment in S_1 direction only has two sensing points that are located across the i^{th} segment sensing points, two rows of the C_{rS_1} matrix have nonzero entries, i.e. $D_{zw}^G = 0_{12\times3}$ and $D_{zu}^G = 0_{12\times3}$, and do not contribute to the relative displacement output. Then, C_{zT}^G and C_{zS}^G can be defined as follows:

$$C_{zT}^G = C_r C_t \tag{9.11}$$

$$\begin{aligned} C_{zS}^G = [&C_{S_1^{-1}}\ \ 0_{12\times m}\ \ C_{S_2^{-1}}\ \ 0_{12\times m}\ \ C_{S_3^{-1}}\ \ 0_{12\times m} \\ &C_{S_1}\ \ 0_{12\times m}\ \ C_{S_2}\ \ 0_{12\times m}\ \ C_{S_3}\ \ 0_{12\times m}] \end{aligned} \tag{9.12}$$

9.1.2 Wind disturbance

As mentioned previously, the wind effect will be the main source of disturbance in the next generation of ground-based optical telescopes. Up until now, existing telescope controllers effectively ignored this disturbance. However, as the size of the primary mirror grows, the higher frequency wind disturbance must be taken into account. The wind loading on the TMT has been previously investigated by [46]. In this work, the power spectral density (PSD) plot of wind disturbance was obtained using a computational fluid dynamics (CFD) analysis. An experimental study of the wind disturbance of the Gemini telescope, which is one of the largest ground-based telescopes in operation, has also been carried out in [47]. In our simulations, the wind disturbance PSD plots provided in [46] and in [47] have been considered. If the area under a conservative upper bound of these PSD plots is calculated, a wind pressure square value of about 10 Pa^2 can be obtained. The square root of this number gives the wind pressure rms acting on the surface of the primary mirror. Multiplying this rms value with the area of the hexagonal segment with 0.33 m sides, i.e. 0.283 m^2, gives the total rms wind disturbance acting on the surface of the individual segments of our design, i.e. 0.895 N. Since each segment is supported by three actuators, the worst-case rms value of the wind disturbance input to each actuator can then assumed to be around 0.30 N. Figure 9-2 shows the system diagram with scaling matrices for controller synthesis. In this diagram, the scaling matrix for the wind disturbance is thus taken as follows:

$$W_n = 0.3 \times I_{3\times3}. \tag{9.13}$$

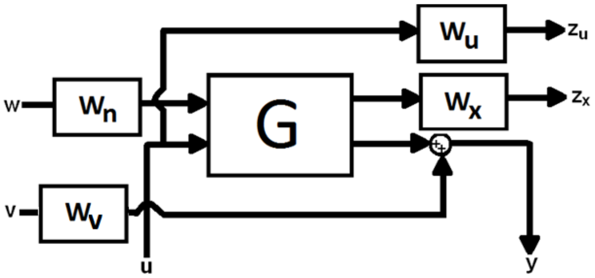

Figure 9-2. Control system block diagram for the H∞ control synthesis.

9.1.3 Imaging performance requirements

Imaging devices are diffraction-limited as their image resolutions are determined by their optical power. Some measures like peak-to-valley (P-V) criterion, rms criterion and Strehl ratio have been devised to define the optical quality of an imaging device. Among these measures, Strehl ratio suits better in defining the imaging quality of optical telescopes. It measures ranges from 0 to 1 as 1 being a theoretically perfect optical system. An optical system with Strehl ratio of 0.8 and over is considered to be diffraction-limited. A plot of Strehl ratio versus rms value of relative edge displacements has already been calculated for the particular design shown in [31]. Although our design, in which the dynamic couplings among segments have been modelled, is quite different from the design presented in [31] since the geometric parameters of the primary mirror surfaces are similar, it is possible to take the results of [31] to determine an objective rms value for the relative edge displacements of our design. As it can be seen from Figure 9-3, a rms value of less than 10^{-8} m corresponds to a Strehl ratio of greater than 0.8. In other words, a rms value of less than 10^{-8} m means that the system performance is only determined by the optical capabilities of the telescope. A controller achieving a rms value of less than 10^{-8} m does not put any restrictions on the resolution of the captured image by the optical telescope. In order to incorporate this objective into our control synthesis, the scaling matrix $W_x = 10^8 \times I_{12\times12}$ (see Figure 9-2) is multiplied to the relative edge displacements of a single segment distributed model output z_i^G in equation (9.2).

9.1.4 Feasible controller requirement

In order to synthesize a feasible controller that operates in a low frequency band with bounded actuation, the following scaling matrix W_u (see Figure 9-2) is used:

$$W_u = \frac{s + 200}{s + 20000}. \tag{9.14}$$

With this scaling filter, we set our objective of synthesizing a controller that will operate in frequencies around 3 kHz with supplied force of less than 100 N.

9.1.5 Noise

In our control synthesis, a rms value 10^{-10} m is assumed for the sensor noise. This value is comparable to the sensor noise level present in the Keck Telescope. This noise is added to the sensor feedback of the system and, in the synthesis, the noise input is scaled accordingly by applying $W_v = 10^{-10} \times I_{3\times 3}$ (see Figure 9-2). In our simulations, we realize the noise by filtering a unity PSD signal through the following filter:

$$W_{noise} = \frac{1.414 \times 10^{-9}}{s + 100}. \tag{9.15}$$

Notice that the above filter has a H_2 gain of 10^{-10}. Considering the time domain characteristics of the H_2 norm, by using the above filter with a unity PSD input, an expected noise rms value of 10^{-10} is realized in our simulations.

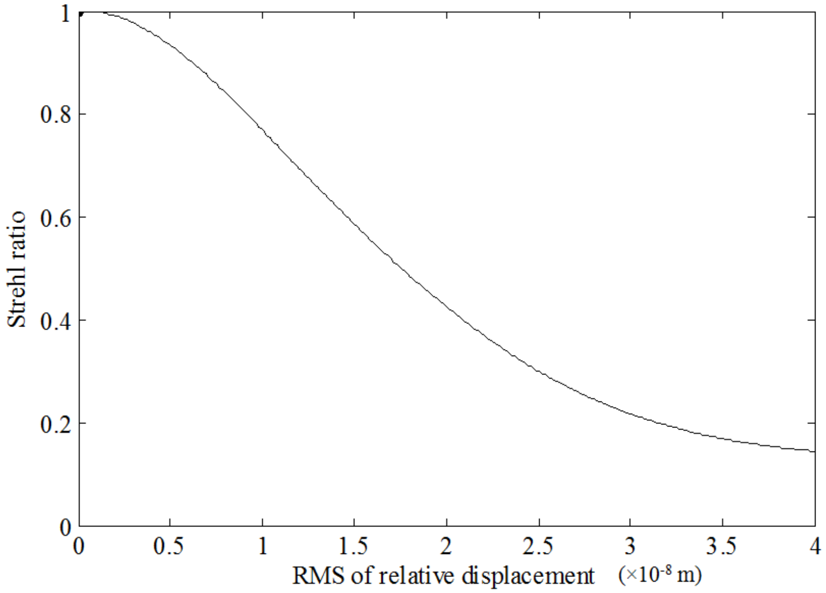

Figure 9-3. Effect of relative displacement to Strehl ratio [31].

9.2 LMI-based distributed controller synthesis

In our distributed controller synthesis, we follow the approach presented in [25]. In this approach, which is summarized in section 4, a controller that guarantees a closed-loop H$_\infty$ system gain of less than 1 (i.e. $\|T_{wz}\|_\infty < 1$) from disturbance inputs w to the objective output z is synthesized (see Figure 9-4). For its complete description and proofs, the reader can refer to [25].

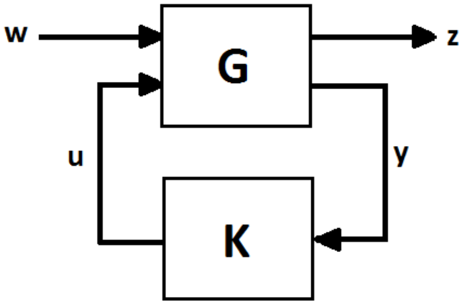

Figure 9-4. General closed-loop system representation for the minimization of the H$_\infty$ norm.

9.3 Simulation results

Open-loop and closed-loop systems with the proposed LMI-based H$_\infty$ distributed controllers are analysed, and the norms of systems are calculated from wind disturbance input to relative segment displacement outputs. Table 9-1 presents the calculated norms of the systems. As can be seen, the closed-loop system norms are well below the objective value ($10^{-8}/0.3$) set for the imaging requirement. Considering aforementioned worst-case disturbance of 0.3 N rms as the system input and the calculated H_∞ norm of the systems, it can be seen that the rms relative edge displacements will be less than 10^{-8} m. This value corresponds to the Strehl ratio of around 0.8 (see Figure 9-3), meaning that the resolution of the telescope images captured will only be determined by the optical power of the instrument (i.e. the resolution of the images will not degrade as a result of the controller performance). Unity PSD signals that were filtered through low pass filters were used in order to realize the wind disturbances and noise signals in the simulations. Furthermore, the performance objective set during the synthesis of the distributed controller and the analysis of the closed-loop gains above guarantees a Strehl ratio of around 0.8, for any wind disturbance and noise model with PSD plots that have underline areas of less than 10 Pa^2 and less than 10^{-20} m^2, respectively. Table 9-2 gives the calculated rms values of input and output of the system obtained from sample simulation runs. Note that, as expected, the system rms gain value is less than the calculated worst-case rms gain of the system (i.e. the H_∞ norm).

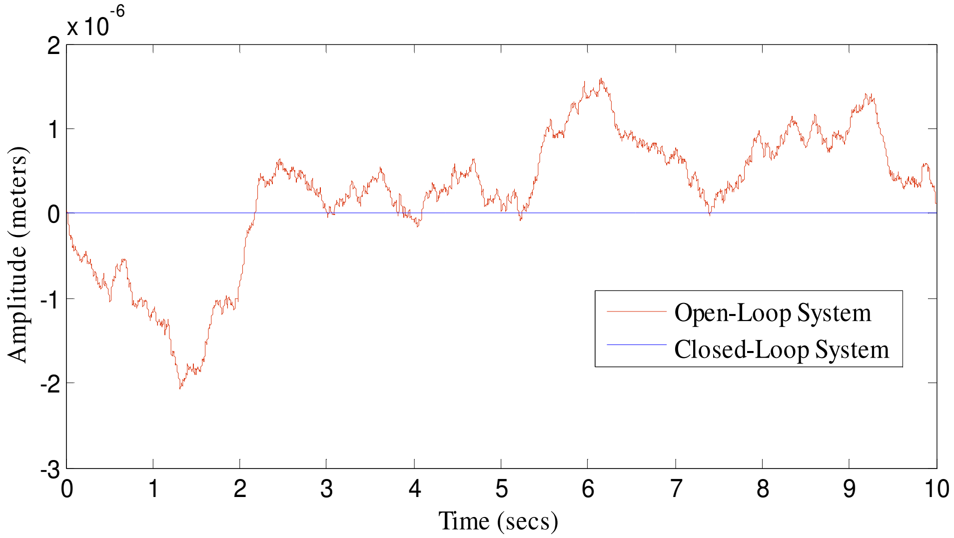

Figure 9-5. Comparison of the relative edge displacements between the open-loop system and closed-loop system with the distributed H_∞ controller.

Figures 9-5 shows the open-loop and closed-loop simulation results of the relative edge displacement. The effect of the distributed controller on the system is evident when the two results are compared. Figure 9-6 shows a close-up view of the same relative edge displacement of the closed-loop system, as it is shown as a straight in Figure 9-5 due to scaling. Figure 9-7 shows the corresponding simulated wind disturbance inputs.

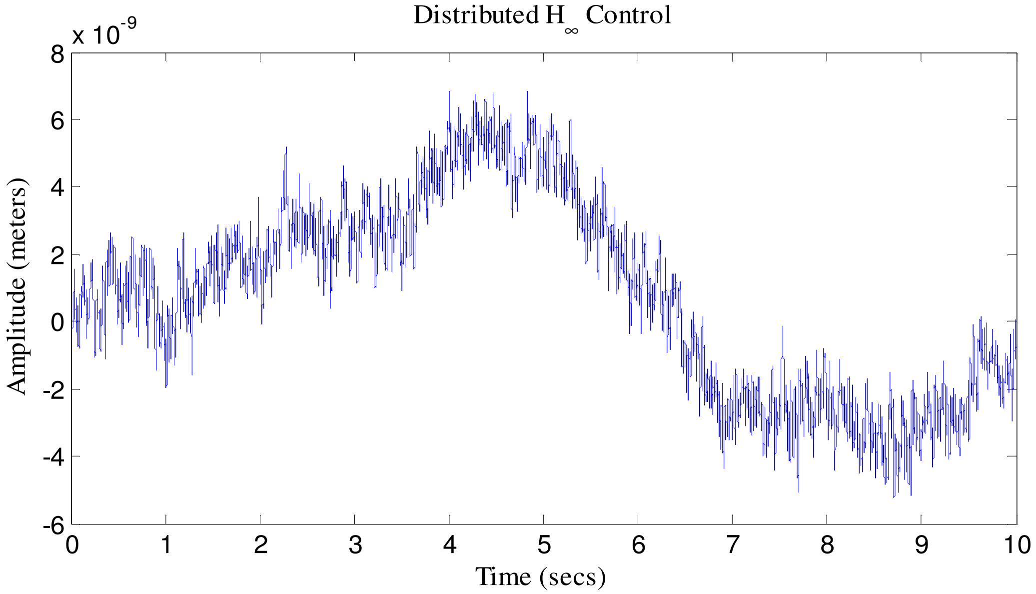

Figure 9-6. Close-up view of the relative edge displacement in the simulation of the closed-loop system with the distributed H_∞ controller.

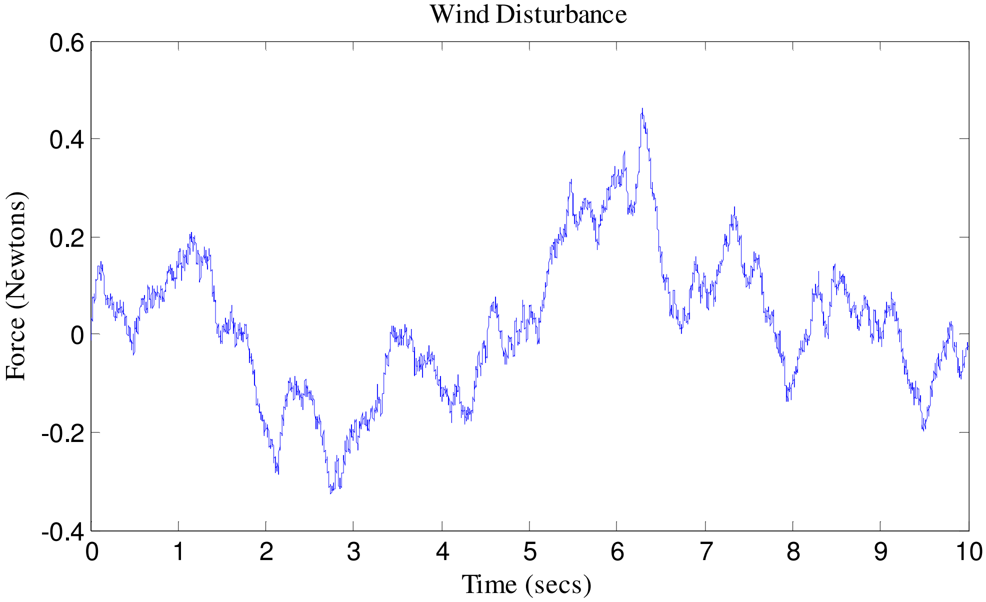

Figure 9-7. Simulated wind disturbance inputs.

Actuator forces of the *0^{th}* segment in the simulation of distributed controller are presented in Figure 9-8. In addition to the time plots of various functions, the maximum singular values versus frequency of the open-loop and closed-loop systems are given in Figures 9-9 and 9-10, respectively, from the wind disturbance inputs to the relative displacement outputs. Note that the peak values in both plots correspond to the H_∞ norms of the open-loop and closed-loop systems presented in Table 9-1.

Table 9-1. H_∞ norms (i.e. worst-case rms gain) of the open and closed-loop systems, from wind disturbance inputs to relative segment displacement outputs.

Open-loop system	2.0280×10^{-5} m/N
Distributed closed-loop system	4.1834×10^{-8} m/N

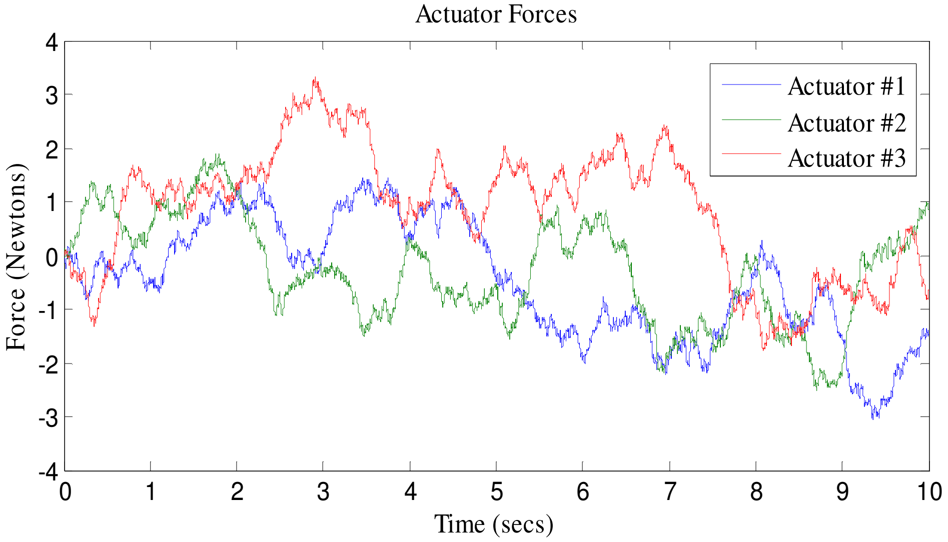

Figure 9-8. Actuator forces on the 0^{th} segment in the simulation of the distributed H_∞ controller.

The simulation results presented in this chapter shows that the distributed control method is indeed applicable to control of large scale systems and, in particular, to control of next generation large segmented telescope mirrors. Imaging performance requirements are still achieved with the distributed control method presented in this paper and the practical implementation difficulties (i.e. extensive cabling, high capacity computing unit, etc.) of the centralized schemes can be avoided. The simulation results demonstrate that it is possible to synthesize distributed controllers that allow us to push the extremely large segmented telescopes into their optical limits without affecting the observed image quality. In addition, the results comply with our analysis through system H_∞ norms as the calculated norms of sample simulations runs are smaller. A H_2 type approach, for instance, would not let us make conservative assumptions about the results of application data. As our future work, the distributed control method presented in this work will be applied to the TMT's actual finite element model, which is being developed from conceptual designs.

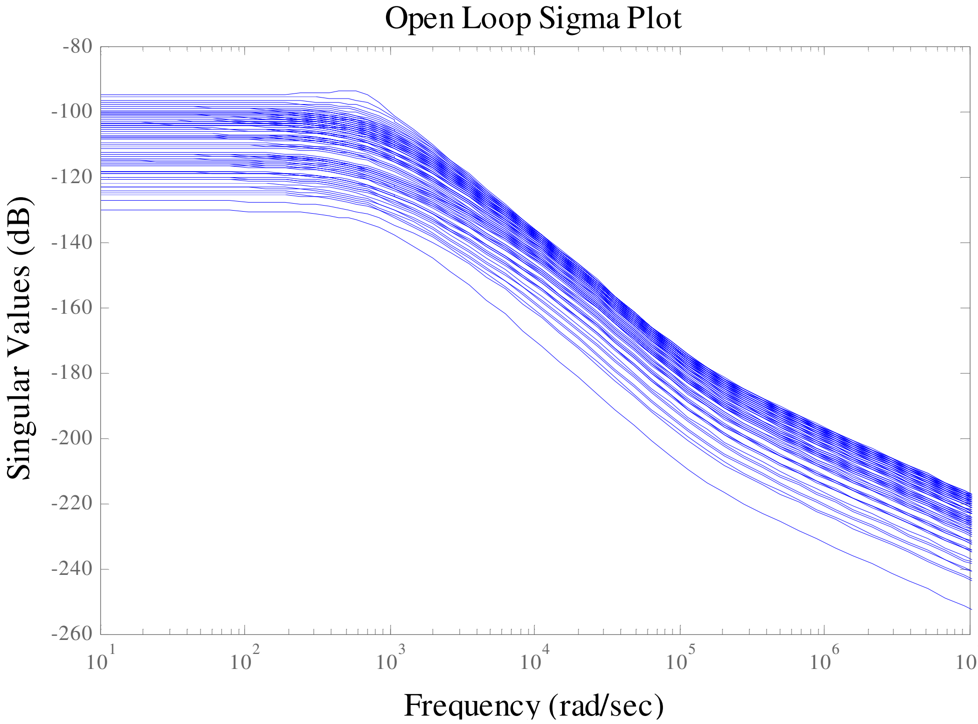

Figure 9-9. Open-loop sigma plots from wind disturbance inputs.

9.4 Conclusion

The next generation of ground-based optical telescopes will employ segmented mirrors to realize extremely large mirrors. With their larger primary mirrors it will be possible to observe fainter celestial objects in the cosmos and extend our knowledge deeper into the universe. Most of the existing telescopes have primary mirrors that are smaller than 8 m in diameter since they employ monolithic mirrors, which are cost prohibitive above the 8 m size limit compared to that of the segmented mirror counterparts. Two of the largest telescopes in operation today (the Keck telescope and the GTC) have segmented primary mirrors of around 10 m in diameter. With the introduction of the next generation telescopes, such as the TMT and E-ELT, primary mirrors of larger than 30 m in diameter will be employed. This implies a significant big leap in the size of the primary mirrors, thus a need for new primary mirror control techniques emerges. In this chapter, distributed control of large segmented mirrors via LMI is presented. A single segment is modelled with spatial inputs and outputs that account for the structural coupling among segments in the primary mirror. These spatial signals are augmented with segment and controller information to make co-operations among neighbouring segment controllers possible in achieving a common goal of stabilizing and maintaining the overall mirror shape. By using this single distributed model, a primary mirror with 492 segments, which is similar to the size of the TMT design, is obtained by connecting the segments through modelled spatial input and outputs. The performance requirements of the distributed primary mirror controllers are set to have diffraction-limited observations from the particular mirror design presented herein. Also, a wind pressure model for the next generation telescopes is taken into account to synthesize a distributed H_∞ controller that keeps the rms gain of the system within the limits of the diffraction-limited observations in the worst-case scenarios. A large scale simulation of the 492-segment system has been carried out and both time and frequency analysis results of both open and closed-loop systems are presented. The simulation results comply with the control objectives set in the design phase of the distributed controllers.

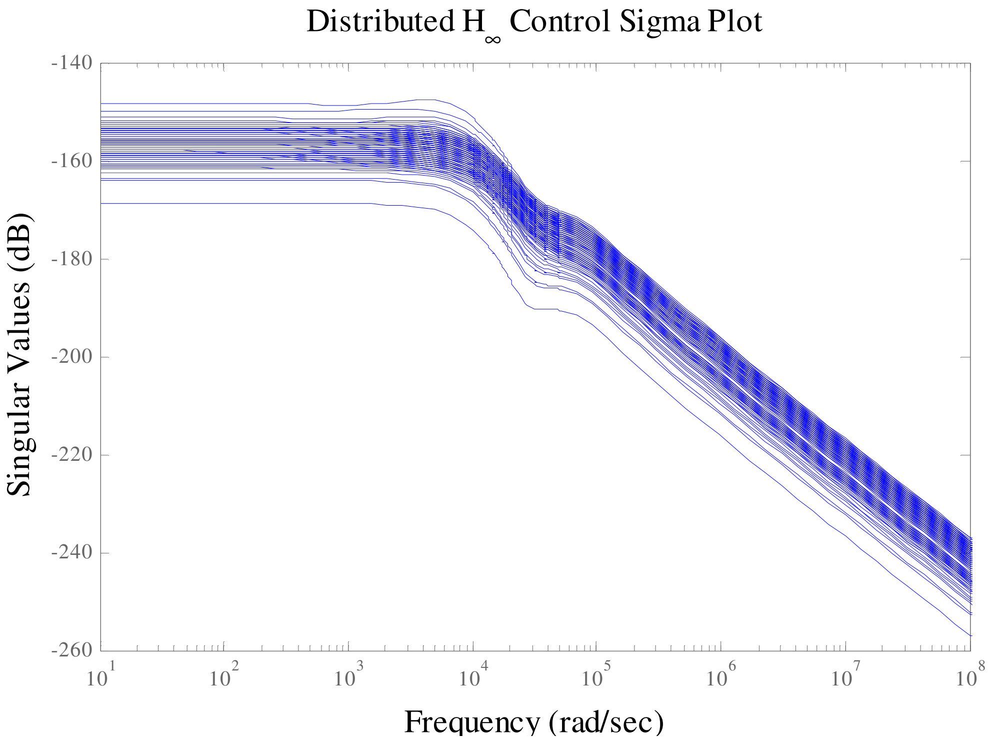

Figure 9-10. Distributed H_∞ control sigma plots from wind disturbance inputs.

Table 9-2. Rms values of various input-output pairs obtained from sample simulation runs and the corresponding system gains.

System	Rms values of wind disturbance	Rms value of relative segment displacements	Rms gain of system
Open-loop system	0.2310	6.3401×10^{-7} m	2.7446×10^{-6} m/N
Distributed closed-loop system	0.2309	2.9678×10^{-9} m	1.2853×10^{-8} m/N

10. DISTRIBUTED H$_\infty$ CONTROL OF THE THIRTY METER TELESCOPES PRIMARY MIRROR

In this chapter, LMI- and Fourier-based distributed H$_\infty$ control of the Thirty Meter Telescope (TMT) project is investigated. TMT is one of the next generation telescope projects in which 492 hexagonal segments will be employed to create a 30 meter diameter circular optical aperture. The vast number of control parameters introduced by the segmented mirror design makes stabilizing and aligning the segments against disturbances a very challenging task to handle. Although a decentralized design can simplify the control problem of a system with a large number of interconnected subsystems, the objective of keeping the relative displacement of the neighbouring segments couples the subsystems at the objective level. Also, since the segments are installed on a common support structure, any control action in one segment disturbs the overall system and results in a coupling at the dynamic level. In order to account for these two levels of couplings among the subsystems distributed control scheme is proposed. In this scheme, by sharing control data among neighbouring segments, objective and dynamic couplings can be addressed. In this chapter, we investigated the application of two different distributed H$_\infty$ control approaches to the next generation telescope control problem. H$_\infty$ control allows us to set certain bounds to the outputs and operate the telescope at its best performance possible in the case of bounded uncertainties. In our synthesis and simulations, we used the state-space model obtained through the analysis of the finite element model provided to us by the TMT project group. The main results of this chapter will be published.

10.1 Extraction of compatible single segment models from TMT model

This twenty one input three output state-space model of the i^{th} segment can be represented as follows:

$$\dot{x}_i = Ax_i + B_F f_i \tag{10.1}$$

$$y_i = Cx_i \tag{10.2}$$

where $f_i \in R^{21}$, $y_i \in R^3$ are the input and output vectors respectively. Since the dynamics is assumed to be spatially invariant, state-space matrices are identical for all single segment models. Input vector f_i and B_F matrix can be decomposed as follows:

$$\dot{x}_i = Ax_i + \begin{bmatrix} B & B_{S_1} & B_{S_3^{-1}} & B_{S_2} & B_{S_1^{-1}} & B_{S_3} & B_{S_2^{-1}} \end{bmatrix} \begin{bmatrix} u_i & u_{iS_1} & u_{iS_3^{-1}} & u_{iS_2} & u_{iS_1^{-1}} & u_{iS_3} & u_{iS_2^{-1}} \end{bmatrix}^T \tag{10.3}$$

where $u_i \in R^3$ is the actuator force input of the i^{th} segment and the remaining inputs $u_{i*} \in R^3$ are the actuator force inputs of the neighbouring segments in six spatial directions specified by the subscript. These neighbouring segment inputs can be specified in terms of u_i with the help spatial shift operators S_1, S_2, S_3 as follows:

$$\begin{aligned} \dot{x}_i &= Ax_i + \\ &\begin{bmatrix} B & B_{S_1}S_1 & B_{S_3^{-1}}S_3^{-1} & B_{S_2}S_2 & B_{S_1^{-1}}S_1^{-1} & B_{S_3}S_3 & B_{S_2^{-1}}S_2^{-1} \end{bmatrix} u_i \\ &= Ax_i + B_C u_i \end{aligned} \tag{10.4}$$

Although with the above representation dynamic couplings can be addressed via a coupling input matrix B_C, a mapping from the absolute positions of the actuator tip points y_i to relative displacements at the edges is needed to be able to address the misalignments in the controller synthesis. Assume, $C_0 \in R^{12x3}$ as a mapping from y_i to twelve edge segment points and $C_i \in R^{2x3}, i \in \{S_1, S_2, S_3, S_1^{-1}, S_2^{-1}, S_3^{-1}\}$ as the mapping from neighbouring segment actuator tip points in one spatial direction to the two edge points of that neighbouring segment that is across the edge gap between the two segments. Then in order to represent relative displacements, the following representation can be used:

$$z_i = C_0 x_i - \begin{bmatrix} C_{S_1} S_1 \\ C_{S_3^{-1}} S_3^{-1} \\ C_{S_2} S_2 \\ C_{S_1^{-1}} S_1^{-1} \\ C_{S_3} S_3 \\ C_{S_2^{-1}} S_2^{-1} \end{bmatrix} x_i = C_C x_i \tag{10.5}$$

where $z_i \in R^{12}$ is the relative displacements at the segment edges of the i^{th} segment.

In Eq.s (10.4) and (10.5) shift operators are coupled with the input $\mathrm{u_i}$ and the state of the segment x_i. Fourier transform can be used to separate these spatially invariant operators and by synthesizing a controller at each frequency in the Fourier domain and by the help of the inverse Fourier transform a controller in time domain can be calculated [24]. In other words, this representation is compatible with the first method that uses Fourier transform to calculate a distributed H_∞ controller. However for the second method (i.e. LMI method) this representation is needed to be converted to the following form:

$$\begin{bmatrix} \dot{x}_i^G \\ r_i^G \\ z_i^G \\ y_i^G \end{bmatrix} = \begin{bmatrix} A_{TT}^G & A_{TS}^G & B_{Td}^G & B_{Tu}^G \\ A_{ST}^G & A_{SS}^G & B_{Sd}^G & B_{Su}^G \\ C_{zT}^G & C_{zS}^G & D_{zd}^G & D_{zu}^G \\ C_{yT}^G & C_{yS}^G & D_{yd}^G & D_{yu}^G \end{bmatrix} \begin{bmatrix} x_i^G \\ p_i^G \\ d_i^G \\ u_i^G \end{bmatrix} \tag{10.6}$$

where the matrices A_{TT}^G, B_{T*}^G, C_{*T}^G, and D_{**}^G are the standard temporal based state-space matrices with x_i, y_i, d_i, u_i denoting the state vector, output(i.e. absolute positions of the actuator tips), disturbance and controller inputs of the i^{th} segment, respectively. The matrices with the S subscript are associated with the spatial signals p and r. Neighbouring segments affect the dynamics of each other through these spatial input and output vectors p and r.

From the representations shown in Eq. (10.6) it can be seen that $A_{TT}^G = A$ and $C_{yT}^G = C$. In Eq. (10.6), the information about objective and dynamic couplings can be shared among the neighbouring segments through the spatial signals p and r. To account for the dynamic interactions and to achieve co-operation among segments, the spatial signals can be defined as follows:

$$p_i^G = \left[x_{iS_1}{}^T \quad d_{iS_1}{}^T \quad u_{iS_1}{}^T \quad x_{iS_3^{-1}}{}^T \quad d_{iS_3^{-1}}{}^T \quad u_{iS_3^{-1}}{}^T \right. \tag{10.7}$$
$$\left. \dots \quad x_{iS_2^{-1}}{}^T \quad d_{iS_2^{-1}}{}^T \quad u_{iS_2^{-1}}{}^T \right]^T$$

$$r_i^G = [x_i{}^T \quad d_i{}^T \quad u_i{}^T \quad x_i{}^T \quad d_i{}^T \quad u_i{}^T \quad \dots \quad x_i{}^T \quad d_i{}^T \quad u_i{}^T]^T \tag{10.8}$$

where subscript specifies the neighbouring segment(in other words the origin of the spatial data). For instance, $x_{iS_3^{-1}}$ is the state of the neighbouring segment in the opposite of the S_3 direction of the i^{th} segment. As can be seen from the definitions of the spatial signals, the states, disturbance and control signals of the neighbouring segments affect the dynamics of an individual segment, and the states, disturbance and control signals of that individual segment flow to the neighbouring segments to be taken into account by the neighbouring segment controllers.

After defining the spatial input and output signals, we can continue to match the regular state-space matrices of an individual segment to the compatible form presented in Eq. (10.6). By defining the modified state-space matrices as below, a representation compatible to the synthesis of LMI-based method presented in [25] can be calculated:

$$\mathrm{A}_{\mathrm{TS}}^{\mathrm{G}} = \left[0 \quad \mathrm{B}_{\mathrm{S}_1} \quad \mathrm{B}_{\mathrm{S}_1} \quad 0 \quad \mathrm{B}_{\mathrm{S}_3^{-1}} \quad \mathrm{B}_{\mathrm{S}_3^{-1}} \quad 0 \quad \mathrm{B}_{\mathrm{S}_2} \quad \mathrm{B}_{\mathrm{S}_2} \right. \tag{10.9}$$
$$\left. 0 \quad \mathrm{B}_{\mathrm{S}_1^{-1}} \quad \mathrm{B}_{\mathrm{S}_1^{-1}} \quad 0 \quad \mathrm{B}_{\mathrm{S}_3} \quad \mathrm{B}_{\mathrm{S}_3} \quad 0 \quad \mathrm{B}_{\mathrm{S}_2^{-1}} \quad \mathrm{B}_{\mathrm{S}_2^{-1}} \right],$$

$$\mathrm{A}_{\mathrm{ST}}^{\mathrm{G}} \tag{10.10}$$
$$= [\mathrm{I} \quad 0 \quad 0 \quad \mathrm{I} \quad 0 \quad 0 \quad \mathrm{I} \quad 0 \quad 0 \quad \mathrm{I} \quad 0 \quad 0 \quad \mathrm{I} \quad 0 \quad 0 \quad \mathrm{I} \quad 0 \quad 0]^{\mathrm{T}},$$

$$\mathrm{B}_{\mathrm{Td}}^{\mathrm{G}} = \mathrm{B}, \tag{10.11}$$

$$\mathrm{B}_{\mathrm{Tu}}^{\mathrm{G}} = \mathrm{B}, \tag{10.12}$$

$$\mathrm{B}_{\mathrm{Sd}}^{\mathrm{G}} \tag{10.13}$$
$$= [0 \quad \mathrm{I} \quad 0 \quad 0 \quad \mathrm{I} \quad 0 \quad 0 \quad \mathrm{I} \quad 0 \quad 0 \quad \mathrm{I} \quad 0 \quad 0 \quad \mathrm{I} \quad 0 \quad 0 \quad \mathrm{I} \quad 0]^{\mathrm{T}},$$

$$\mathrm{B}_{\mathrm{Su}}^{\mathrm{G}} \tag{10.14}$$
$$= [0 \quad 0 \quad \mathrm{I} \quad 0 \quad 0 \quad \mathrm{I} \quad 0 \quad 0 \quad \mathrm{I} \quad 0 \quad 0 \quad \mathrm{I} \quad 0 \quad 0 \quad \mathrm{I} \quad 0 \quad 0 \quad \mathrm{I}]^{\mathrm{T}},$$

$$C^{G}_{zT} = C_0, \tag{10.15}$$

$$\begin{aligned} C^{G}_{zS} = \big[& C_{S_1} \quad 0 \quad 0 \quad C_{S_3^{-1}} \quad 0 \quad 0 \quad C_{S_2} \quad 0 \quad 0 \\ & C_{S_1^{-1}} \quad 0 \quad 0 \quad C_{S_3} \quad 0 \quad 0 \quad C_{S_2^{-1}} \quad 0 \quad 0 \big], \end{aligned} \tag{10.16}$$

and all the remaining matrices equal to zero matrices with appropriate sizes ($A^{G}_{SS} = 0$, $D^{G}_{zd} = 0$, $D^{G}_{zu} = 0$, $C^{G}_{yS} = 0$, $D^{G}_{yd} = 0$, $D^{G}_{yu} = 0$).

With the above definitions of the matrices, it can easily be shown that the modified state-space representation is identical to the combined equations presented in Eq.s (10.1), (10.2) and (10.5).

10.2 Setting up the model for synthesis

In this chapter, the setting up of the problem for the controller synthesis will be described.

Generic H_∞ control techniques assume unity signals and aims to calculate a feasible controller that will make the closed-loop system input-output H_∞ gain less than one. Figure 10-1 shows the closed-loop system with the plant G and the controller K that generic algorithm assumes. In this representation, d is the input disturbance, u is the control signal, y is the sensor output of the plant, and z is the output signal to be minimized. For a plant G generic H_∞ control algorithm calculates a controller K that will make closed-loop H_∞gain from d to z less than one (i.e. $\|T_{dz}\|_\infty < 1$). To be able to give the signals physical meaning scaling filters are used as shown in Figure 10-2.

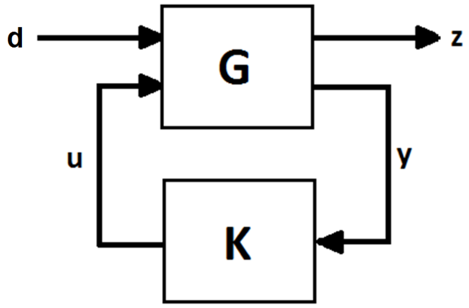

Figure 10-1. Closed-loop system representation for a generic H_∞ synthesis algorithm.

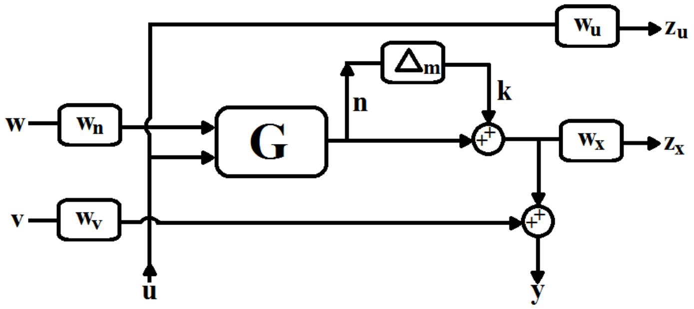

Figure 10-2. Control system block diagram for the H_∞ control synthesis.

10.2.1 Wind disturbance

Existing telescope controllers ignore the wind effect during the synthesis of controllers as the primary mirrors of earlier telescopes are much smaller than the ones designed for the next generation telescopes. However with the big leap in the size of the primary mirror, this effect becomes the dominant effect surpassing the thermal, gravitational and seismic disturbances. Moreover, compared to these disturbances wind effect has a higher frequency spectrum that requires faster controllers to account for the disturbances caused by the wind blowing in the enclosure [16, 18].

In order to have diffraction-limited observations even in the worst-case gain of the closed-loop system, we first need to determine the characteristics of the wind. To have an estimate of the wind in TMT, the wind characteristics study presented in [47] is considered. In [31], the experimental study presented in [47] about the wind disturbance of the Gemini telescope is taken into account in the calculation of the white noise pressure filter (see Figure 10-3). Since in this paper H_∞ approach is considered rather than H_2, we model the wind disturbance as a unity power spectral density (PSD) signal of bandwidth 4 Hz (highest modelled wind frequency in [47]) filtered through the force filter calculated according to the pressure filter provided in [31] and the geometric properties of the segment. The wind force scaling filter shown in Figure 10-2 for the wind disturbance is calculated as:

$$W_n = \frac{2 * (0.0856s + 1.3418)}{0.1196s^2 + 1.32s + 1} \times I_{3\times3}, \tag{10.17}$$

where pre-multiplier 2 of the numerator corresponds to the rms value of the 4 Hz unity PSD signal. If the H_2 norm of the above filter is investigated, the expected rms value of the wind can be calculated as 1.6795 N.

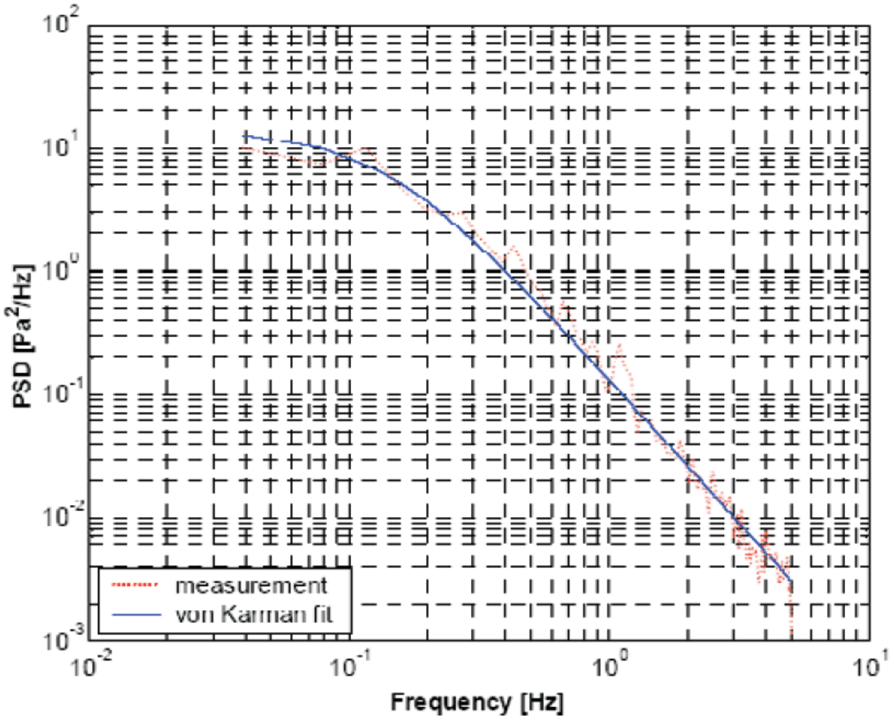

Figure 10-3. Pressure PSD on the primary mirror with the Von Karman fit. [47, 31].

10.2.2 Imaging performance requirements

In literature, there are various criteria in defining the imaging quality of an optical device. Some of the prominent measures are peak-to-valley (P-V) criterion, rms criterion and Strehl ratio. In this chapter, we concentrated on the Strehl ratio since it better describes the optical performance of telescopes compared to the other measures. The Strehl ratio of an optical device is defined in the range of 0 to 1 as 1 being a perfect optical device. A telescope performance is bounded by a limit called the diffraction limit. Diffraction occurs at the edges of opaque objects in the optical path of an imaging device.

Every optical device suffers from the diffraction phenomenon and the resolution of an image that can be obtained is limited and depends on the geometric properties of the device and the properties of the light to be observed. An optical system with a Strehl ratio that is greater than 0.8 is considered as a perfectly operating imaging device [2]. Observations of a perfectly operating optical device are called diffraction-limited observations. For the geometry of the TMT and the light that is going to be observed, the effect of the rms value of the relative displacements at the segment edges on the Strehl ratio versus rms tip-tilt error is given in Figure 10-4 [27]. It can be seen that if the rms value of relative displacements can be kept below 10^{-7} m, visible light observations can be considered diffraction-limited. This value is also close to the Marechal's approximation $\mathrm{rms} < \lambda/14$ where λ is the wavelength of the light to be observed and rms is the wavefront error that equals to the double of the rms surface error. This limit can easily be set as the performance bound during the synthesis of a H_∞ controller. Since generic H_∞ controller synthesis approach assumes unity signals and sets maximum H_∞ gain bound as 1, a scaling filter $W_x = 10^7 \times I_{12\times12}$ can be utilized to set the desired rms limit to the output signal of the plant (see Figure 10-2).

10.2.3 Feasible controller requirement

Any controller that is synthesized must be physically feasible. Since generic control synthesis methods assume unit signals for the input and output signals and do not restrict control actuation, in order to set bounds to the solution space of the controller, scaling filters can be used. By setting the control actuation signals as outputs through the following filter, a bounded frequency and bounded actuation is guaranteed:

$$W_u = \frac{s + 200}{s + 20000} \times I_{3\times3}. \tag{10.18}$$

Specifically, with the above filter synthesized controller is guaranteed to operate in frequencies below 3kHz with a less than 100 N actuation force.

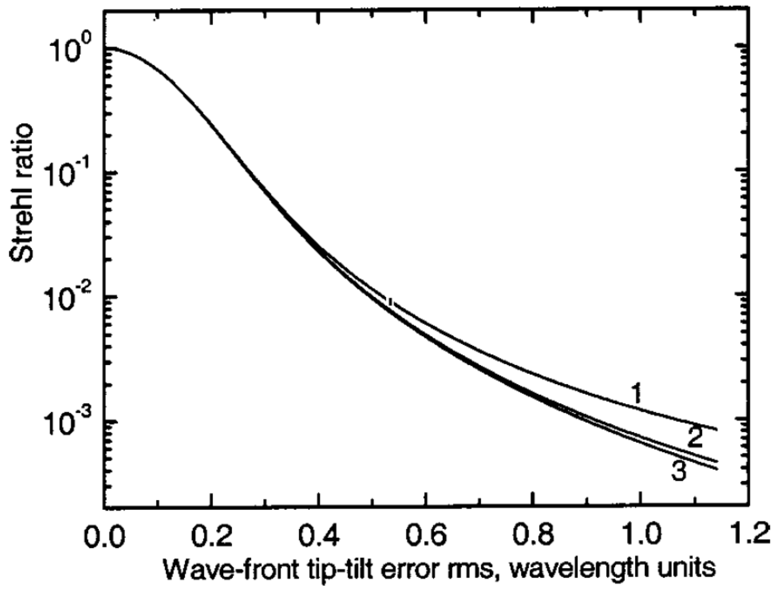

Figure 10-4. Strehl ratio as a function of tip-til rms in units of wavelength for different number of segments: 1, N=37; 2, N=217; 3, N=817 [26].

10.2.4 Noise

Every physical sensor suffers from noise when measuring continuous signals. In order to test synthesized controllers more realistically, noise signal with 5x10^{-10} m rms value is added to the sensor feedback by using the scaling filter $\mathrm{W_v} = 5 \times 10^{-10} \times \mathrm{I}_{3\times 3}$. This number is comparable to the noise present in the Keck edge sensors [48]. In order to simulate this signal, unity PSD signal source is filtered through the following filter:

$$W_{noise} = \frac{7.07 \times 10^{-9}}{s + 100}. \tag{10.19}$$

Above filter has a H_2 gain of 5x10^{-10} and with a unity PSD as input and output signal with rms value of 5x10^{-10} m can be realized.

10.3 Synthesis of a distributed H∞ controller with Fourier-based method

For the sake of concise publication, the reader is assumed to have an experience of a generic H∞ controller synthesis. For readers who are not familiar with the theory are referred to [28] for a complete discussion.

In this section we will discuss the synthesis of distributed H∞ controller using Fourier transform. With a slight abuse of notation, we repeat the state-space representation of a single segment with the robustness criteria, wind disturbance, noise and scaling filters as follows:

$$\dot{x}_i = Ax_i + B_C u_i + B_C W_n w_i, \tag{10.19}$$

$$z_{xi} = W_x C_C x_i, \tag{10.20}$$

$$z_{ui} = W_u u_i, \tag{10.21}$$

$$n_i = k_i, \tag{10.22}$$

$$y_i = Cx_i + W_v v_i. \tag{10.23}$$

As explained in the extraction phase of a single segment model, B_C and C_C matrices contain spatial shift operators which carry information of the neighbouring segments and model the dynamic and objective couplings. By following the steps described in [24], one can synthesize a distributed H∞ controller. As the first step we can take the Fourier transform of the state-space equations in order to decouple the shift operators:

$$\frac{\partial}{\partial t}\breve{x}_i = \breve{A}\breve{x}_i + \breve{B}_c\breve{u}_i + \breve{B}_C\breve{W}_n\breve{w}_i \tag{10.24}$$

$$\breve{z}_{xi} = \breve{W}_x\breve{C}_c\breve{x}_i \tag{10.25}$$

$$\breve{z}_{ui} = \breve{W}_u\breve{u}_i \tag{10.26}$$

$$\breve{n}_i = \breve{k}_i \tag{10.27}$$

$$\breve{y}_i = \breve{C}\breve{x}_i + \breve{W}_v\breve{v}_i \tag{10.28}$$

After decoupling the shift operators from signals, we can design a H∞ controller in the Fourier domain and by calculating the inverse Fourier transform a controller in time domain can be obtained. However, taking the inverse is not trivial and the controller in time domain will possibly include infinite degree in shift operators. By taking into account the fact (given in [24]) that convolution kernels have exponential rates of decays, we can approximate a controller in time domain by using finite shift operators. If just the first neighbouring segments are considered, the state-space representation of a controller will be in the following form:

$$A_K(S) = A_{K0} + A_{K1}S_1 + A_{K2}S_2 + A_{K3}S_3 + A_{K4}S_1^{-1} + A_{K5}S_2^{-1} + A_{K6}S_3^{-1}, \tag{10.29}$$

$$B_K(S) = B_{K0} + B_{K1}S_1 + B_{K2}S_2 + B_{K3}S_3 + B_{K4}S_1^{-1} + B_{K5}S_2^{-1} + B_{K6}S_3^{-1}, \tag{10.30}$$

$$C_K(S) = C_{K0} + C_{K1}S_1 + C_{K2}S_2 + C_{K3}S_3 + C_{K4}S_1^{-1} + C_{K5}S_2^{-1} + C_{K6}S_3^{-1}, \tag{10.31}$$

$$D_K(S) = D_{K0} + D_{K1}S_1 + D_{K2}S_2 + D_{K3}S_3 + D_{K4}S_1^{-1} + D_{K5}S_2^{-1} + D_{K6}S_3^{-1}. \tag{10.32}$$

By following the procedure described in [28], H_∞ controllers in Fourier domain at some gridding points can be synthesized. The matrices given in Eq.s (10.29)-(10.32) can be estimated by using the Least Squares Estimation (LSE). Since we have three spatial dimensions, an example mth gridding point will be $(\theta_{1m} \quad \theta_{2m} \quad \theta_{3m})$. At this particular point, the state-space matrices in Eq.s (10.29)-(10.32) in Fourier domain can be represented as follows:

$$\begin{aligned} A_{K_m} \cong A_{K0} &+ A_{K1}I_n e^{j\theta_{1m}} + A_{K2}I_n e^{j\theta_{2m}} + A_{K3}I_n e^{j\theta_{3m}} \\ &+ A_{K4}I_n e^{-j\theta_{1m}} + A_{K5}I_n e^{-j\theta_{2m}} + A_{K6}I_n e^{-j\theta_{3m}} \end{aligned} \tag{10.33}$$

$$\begin{aligned} B_{K_m} \cong B_{K0} &+ B_{K1}I_n e^{j\theta_{1m}} + B_{K2}I_n e^{j\theta_{2m}} + B_{K3}I_n e^{j\theta_{3m}} \\ &+ B_{K4}I_n e^{-j\theta_{1m}} + B_{K5}I_n e^{-j\theta_{2m}} + B_{K6}I_n e^{-j\theta_{3m}} \end{aligned} \tag{10.34}$$

$$\begin{aligned} C_{K_m} \cong C_{K0} &+ C_{K1}I_n e^{j\theta_{1m}} + C_{K2}I_n e^{j\theta_{2m}} + C_{K3}I_n e^{j\theta_{3m}} \\ &+ C_{K4}I_n e^{-j\theta_{1m}} + C_{K5}I_n e^{-j\theta_{2m}} + C_{K6}I_n e^{-j\theta_{3m}} \end{aligned} \tag{10.35}$$

$$\begin{aligned} D_{K_m} \cong D_{K0} &+ D_{K1}I_n e^{j\theta_{1m}} + D_{K2}I_n e^{j\theta_{2m}} + D_{K3}I_n e^{j\theta_{3m}} \\ &+ D_{K4}I_n e^{-j\theta_{1m}} + D_{K5}I_n e^{-j\theta_{2m}} + D_{K6}I_n e^{-j\theta_{3m}} \end{aligned} \tag{10.36}$$

After calculating H$_\infty$ controllers at enough gridding points the matrices in Eq.s (10.29)-(10.32) can be estimated by using the LSE. As a result of our synthesis, we will have a controller in the following form:

$$\begin{aligned}\dot{x}_{K_i} &= (A_{K0} + A_{K1}S_1 + A_{K2}S_2 + A_{K3}S_3 + A_{K4}S_1^{-1} + A_{K4}S_2^{-1} + A_{K4}S_3^{-1})x_{K_i} \\ &\quad + (B_{K0} + B_{K1}S_1 + B_{K2}S_2 + B_{K3}S_3 + B_{K4}S_1^{-1} + B_{K4}S_2^{-1} \\ &\quad + B_{K4}S_3^{-1})y_i,\end{aligned} \tag{10.37}$$

$$\begin{aligned}u_{K_i} &= (C_{K0} + C_{K1}S_1 + C_{K2}S_2 + C_{K3}S_3 + C_{K4}S_1^{-1} + C_{K4}S_2^{-1} + C_{K4}S_3^{-1})x_{K_i} \\ &\quad + (D_{K0} + D_{K1}S_1 + D_{K2}S_2 + D_{K3}S_3 + D_{K4}S_1^{-1} + D_{K4}S_2^{-1} \\ &\quad + D_{K4}S_3^{-1})y_i,.\end{aligned} \tag{10.38}$$

From the above form, it can be seen that the controller does not only use its sensor signal and states but also takes into account the neighbouring segment controller sensor signal and states in order to calculate its actuation signals (i.e. control input).

10.4 Synthesis of a distributed H$_\infty$ controller with LMI-based method

The modified state-space representation compatible with the method provided in [25] is already discussed at the extraction phase of the single segment model. To be concise, we will not provide the discussion of the procedure presented in [25]. Just like the generic H$_\infty$ controller synthesis, the controller calculated following [25] will satisfy the closed-loop H$_\infty$ gain bound 1. In other words, the resultant closed-loop system will have a H$_\infty$ gain from disturbance inputs $d = [w^T \quad v^T]^T$ to the objective output $z = [z_u^T \quad z_x^T]^T$ less than 1 (i.e. $\|T_{dz}\|_\infty < 1$) (see Figure 10-1). To be able to achieve robustness criteria, controller also will keep the H$_\infty$ gain from k to n less than 1 (i.e. $\|T_{kn}\|_\infty < 1$). For the complete description and proofs please refer to [18].

10.5 Simulation results

In order to test two distributed H$_\infty$ controllers, two simulation models have been designed. In both simulations, state-space equations of the overall TMT model obtained via finite element analysis of the FEM provided to us by the project group are used to simulate the TMT primary mirror dynamics. In this state-space model, inputs are set as the force inputs applied to the 492×3 actuator tip points and the outputs are taken as the absolute positions of the same 492×3 actuator tip points. Noise added to the absolute position information of the actuator tips is fed to the 492 identical distributed H_∞ controllers as sensor feedback and 492×3 control inputs calculated by these 492 controllers are applied to the TMT state-space model as inputs. For the overall simulation model output, relative displacements at the segment edges are calculated by using the absolute positions of the 492×3 actuator tip points. Disturbance inputs are applied to the TMT state-space model through the same input matrix that control inputs are applied. Figure 10-5 shows overall simulation design and 492 distributed segment controllers connected in a honeycomb pattern.

Figures 10-6, 10-7 and 10-8 present a sample relative displacement at the edge between segments 31 and 32 for open loop and closed loops systems with LMI-based and Fourier-based distributed H_∞ controllers. As can be seen, distributed controllers can keep the relative displacement below the threshold set before the synthesis of the controller via the scaling filter. This is also supported by the Table 1 that gives sample rms values of the input wind disturbance and the output relative edge displacements obtained, as well as the corresponding Strehl ratio calculated assuming the observation of a median wavelength (i.e. 650 nm) of the visible light spectrum from a sample simulation run. Hence, images obtained by the closed-loop systems can be considered as diffraction-limited. In other words, images obtained by the optical systems will not be limited as a lack of controller performance since the error will already stay in the diffraction zone which is inevitable for any optical system. Figure 10-9, 10-10 and 10-11 show sample wind disturbance inputs acting on segments 31 and 32, and the resultant forces produced by the actuators to segments aligned. From the figures and the Table 10-1 it can be said that wind disturbance inputs are less than 2 N rms as set during the simulation by filtering unity PSD signals and also the controller produces bounded actuation force as set during the synthesis phase by using the scaling filter in Equation (10.18) to obtain physically realizable controllers. Figures 10-12, 10-13 and 10-4 show the rms surface error overall surface for the open-loop and the closed-loop systems.

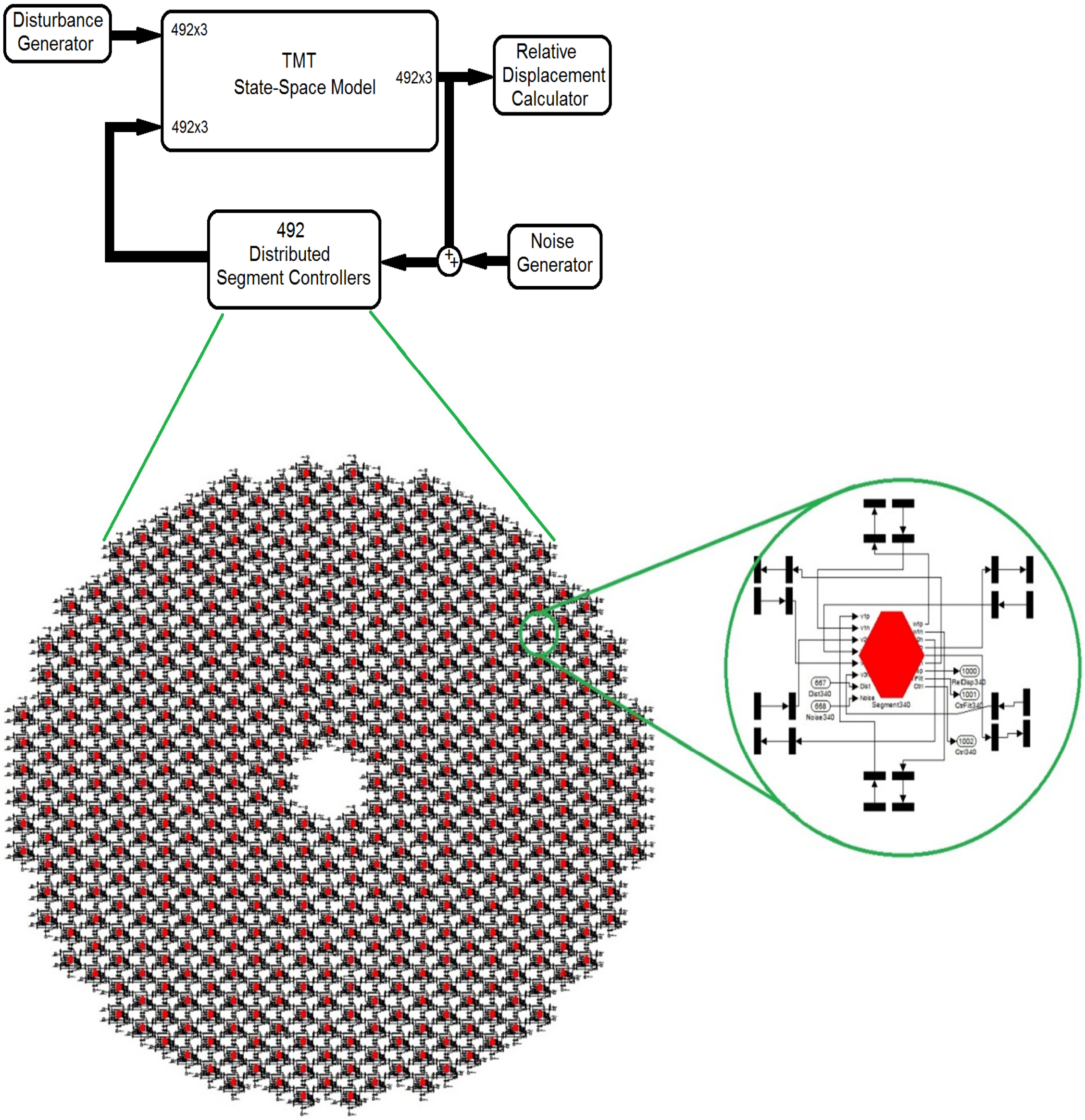

Figure 10-5. Distributed H_∞ control simulation TMT primary mirror.

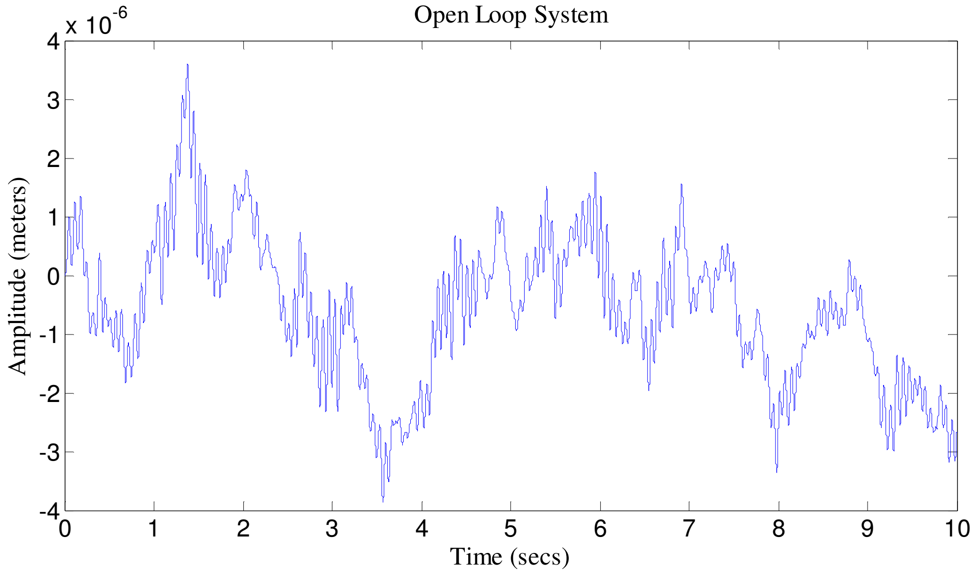

Figure 10-6. Relative displacements at the segment edge of the segments 31 and 32 in the simulation of the open-loop.

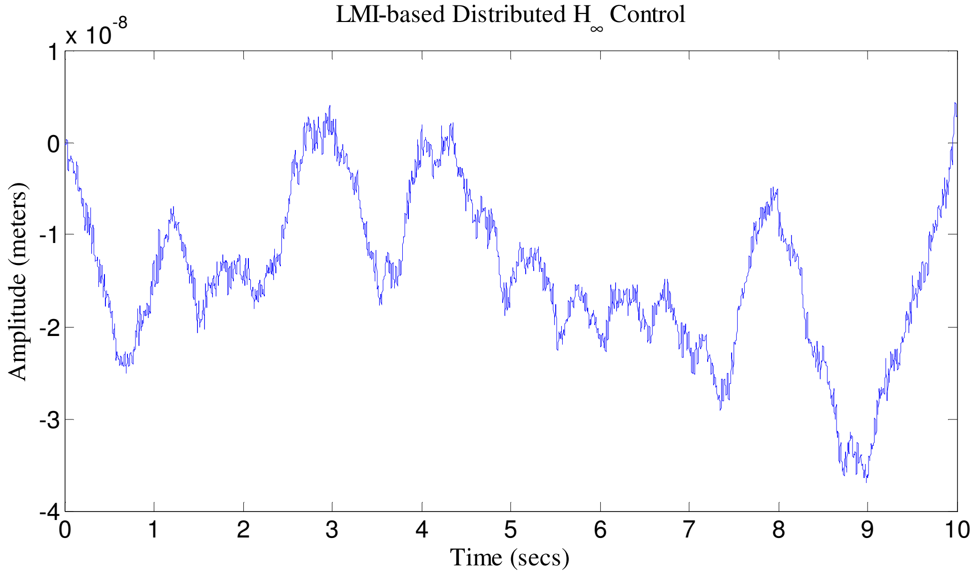

Figure 10-7. Relative displacements at the segment edge of the segments 31 and 32 in the simulation of the LMI-based distributed H_∞ controller.

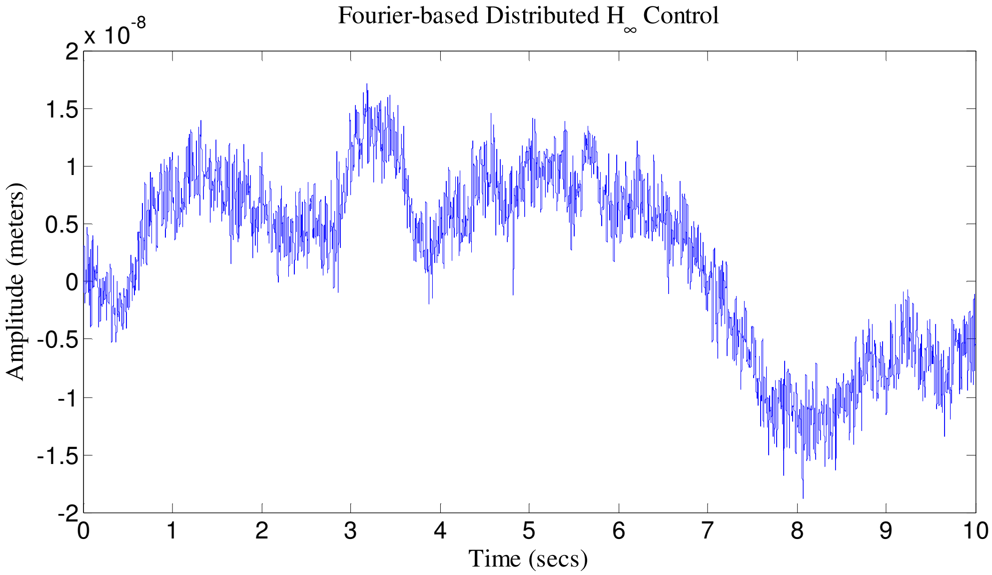

Figure 10-8. Relative displacements at the segment edge of the segments 31 and 32 in the simulation of the Fourier-based distributed H_∞ controller.

As a result of the simulations, we propose the use of distributed H_∞ controllers to maintain the continuity of the primary mirror surface in the presence of wind disturbance. This proposition is very important as the current techniques used in the control of telescope primary mirrors ignore the wind effect by considering the fact that primary mirror is not affected as much compared to the larger primary mirrors of the next generation extremely large telescopes. Also in the next generation telescopes, high frequency wind disturbance is expected to interact with the structural dynamics of the telescope which will bring new challenges to the active control problem. Current controllers only account for the thermal and gravitational disturbances to keep the bandwidth of the active control low enough to avoid the excitation of the structural modes of the telescope. With the introduction of the next generation telescope the dynamic coupling cannot be avoided and decentralized controllers will be ruled out as they cannot account for the interaction between controller and support dynamics. Also a coupled objective of keeping the relative displacements between segment edges rather than the absolute positions of the segments cannot be set as control objective with decentralized controllers. A centralized controller, on the other hand, will require a powerful high computing node with a high communication bandwidth that will make system vulnerable to system failures and also will require extensive cabling. Distributed control seems to be a better choice that will have simple connection architecture while with the capability of addressing coupling problems among segments, controllers and the support structure.

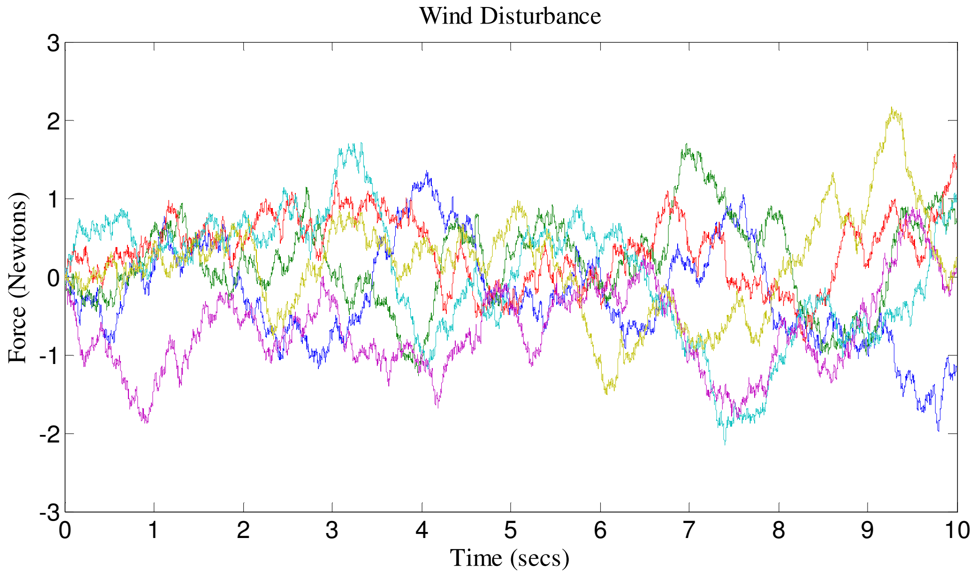

Figure 10-9. Simulated 6 wind disturbance inputs acting at 3 actuation points on segments 31 and 32.

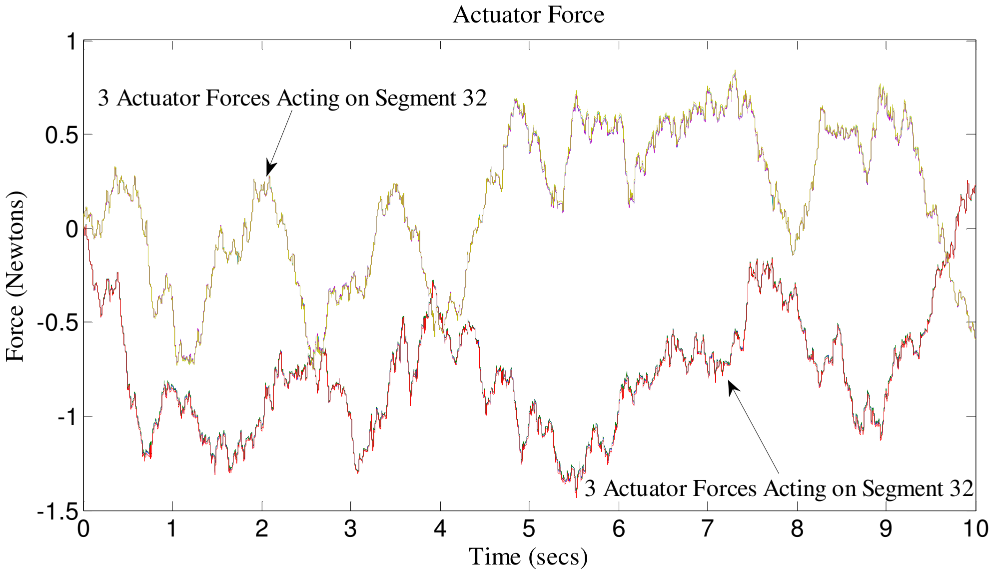

Figure 10-10. Actuator forces on segments 31 and 32 in the simulation of the LMI-based distributed H_∞ controller.

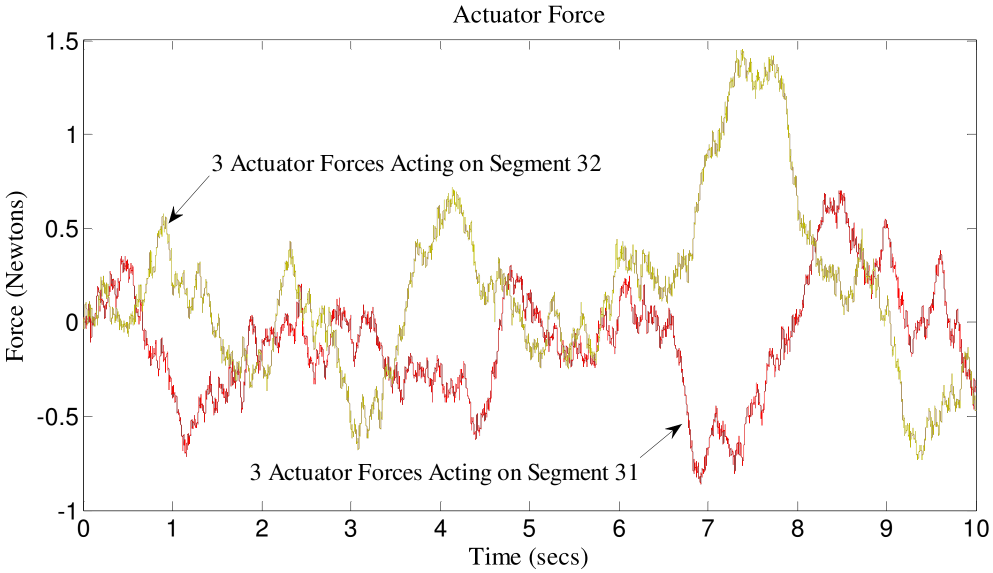

Figure 10-11. Actuator forces on segments 31 and 32 in the simulation of the Fourier-based distributed H_∞ controller.

10.6 Conclusion

To be able to investigate the workings of the universe, astronomers have always been trying to improve the optical capabilities of the telescopes. In the early telescopes, active control was not given much attention as the telescopes performances already suffer from the wavefront disturbances resulting from the change in the refraction index of the atmosphere. However with the introduction and advancements in the adaptive optics field that uses deformable mirrors to indirectly correct the distorted wavefront, the use of the ground-based optical telescopes at their limits became possible. The angular resolution of telescopes is limited by the phenomenon called diffraction. Any opaque object on the optical path will result in the spreading of the light energy on the image plane. The physically possible resolution is inversely proportional to the diameter of the telescope aperture. Hence, the size of the telescope apertures has been increasing according to the advancements in the manufacturing techniques of the mirrors and control devices.

Table 10-1. Rms values of various input-output pairs obtained from sample simulation runs and the corresponding system gains.

System	Rms values of wind disturbance	Rms value of relative segment displacements	Rms gain of system	Strehl Ratio
Open-loop system	1.4430 N	1.3681×10^{-6} m	9.480×10^{-7} m/N	~0
LMI-based Distributed closed-loop system	1.3604 N	1.6677×10^{-8} m	1.2259×10^{-8} m/N	~0.90
Fourier-based Distributed closed-loop system	1.1283 N	7.8958×10^{-9} m	6.9980×10^{-9} m/N	~0.98

Telescopes with primary mirrors over 8 meters are designed with segmented layouts as studies show that beyond this limit the cost of single monolithical mirrors exceeds that of segmented mirrors. Two of the largest aperture telescopes in use today (GTC and KECK with 10 m apertures) employ segmented mirrors and almost all of the next generation telescope projects opt for hexagonal segmented mirrors to realize large optical surfaces. In the near future with the introduction of the next generation extremely large optical telescopes there will be a big leap in the size of the telescope apertures. Wind effect ignored by the current telescope control techniques will become a dominant factor for the next generation extremely large telescopes. As the primary mirror size of a telescope is increased not only the resonant frequencies of the telescope structure will decrease, but also primary mirror will become more sensitive to high frequency wind disturbance. In the next generation telescope control, it is feared that controller that accounts for wind disturbance will excite structural modes of the telescope. Maintaining the continuity and higher order shape of the primary mirror asks for new control techniques. Distributed control seems to be the better choice for the control of the next generation telescope mirrors compared to decentralized and centralized control techniques. Distributed controllers use simple networked controllers that can co-operate towards a common goal of maintaining smooth mirror surface and share information to account for the interactions between telescope structure and controllers.

In this chapter, we designed two spatially-invariant distributed H_∞ controllers using two methods available in literature for the state-space model of the TMT project that is calculated via the analysis of the finite element model provided to us. First single segment models compatible with both methods (i.e. LMI and Fourier) are calculated. Spatial invariance assumption of the single segment model is made use of by using LMI and Fourier methods. Small spatial variances among segments are accounted for by introducing uncertainties to the synthesis problem. Both controllers are tested with simulations. In these simulations 492 identical controllers for each segment are connected in a honeycomb pattern and the control signals are routed between TMT state-space model and these 492 distributed controllers. The results show that distributed H_∞ controllers can keep the effect of wind disturbance on the relative edge displacements below the calculated diffraction limit. In other words, by the help of distributed controllers the resolution of the image obtained by the optical telescope will not be limited by the wind disturbance acting on the segmented mirrors.

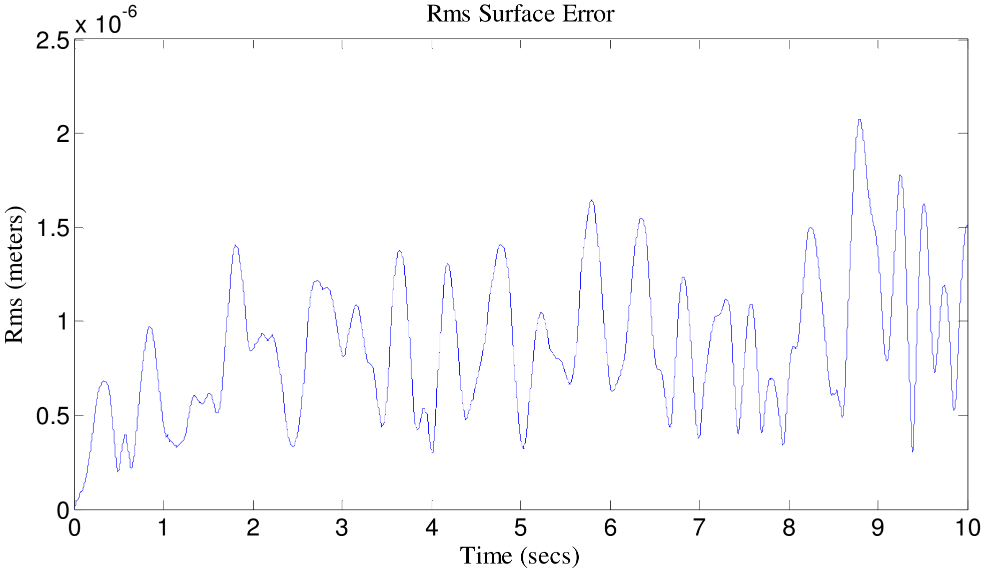

Figure 10-12. TMT primary mirror overall rms surface error in open-loop simulation.

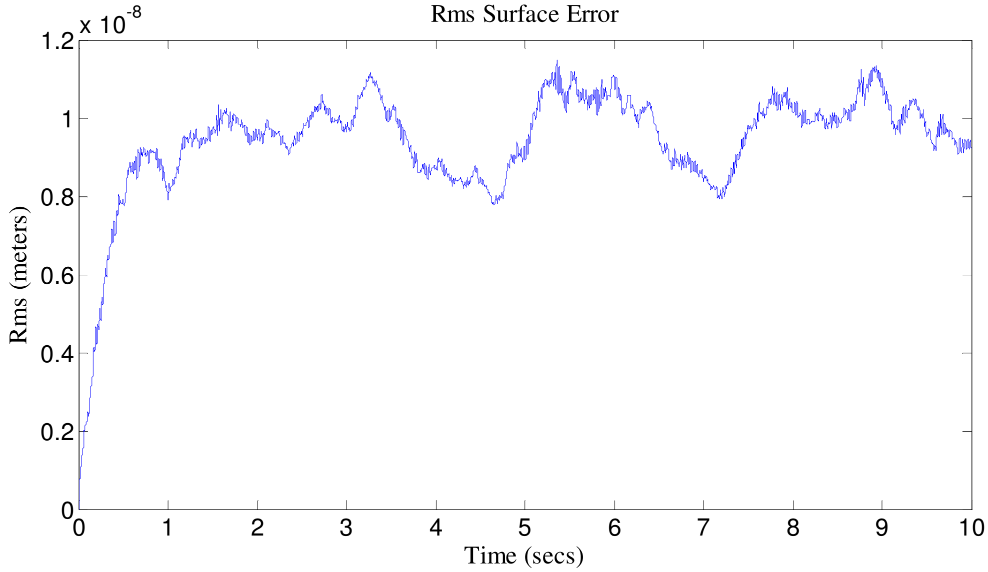

Figure 10-13. TMT primary mirror overall rms surface error in LMI-based distributed controller simulation.

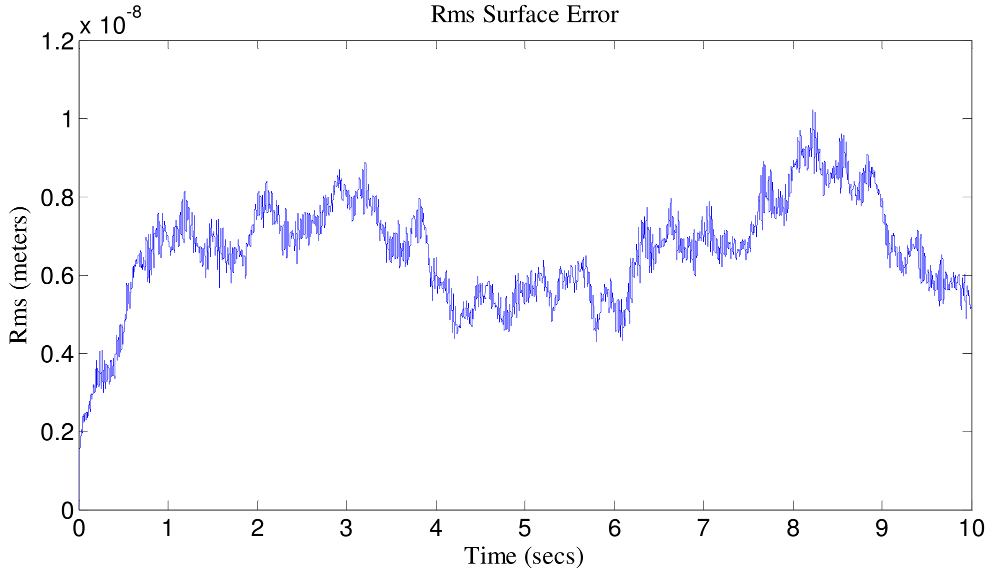

Figure 10-14. TMT primary mirror overall rms surface error in Fourier-based distributed controller simulation.

11. PRELIMINARY SYSTEM IMPLEMENTATION

In this chapter, a possible experimental set up for performance evaluation is discussed. This setup will allow one to check and compare the performances of various designed controllers. Simulation results and experimental results could also be compared and mathematical model could be updated accordingly. More information about the CAD (Computer-Aided Design) of the setup can be obtained from [49].

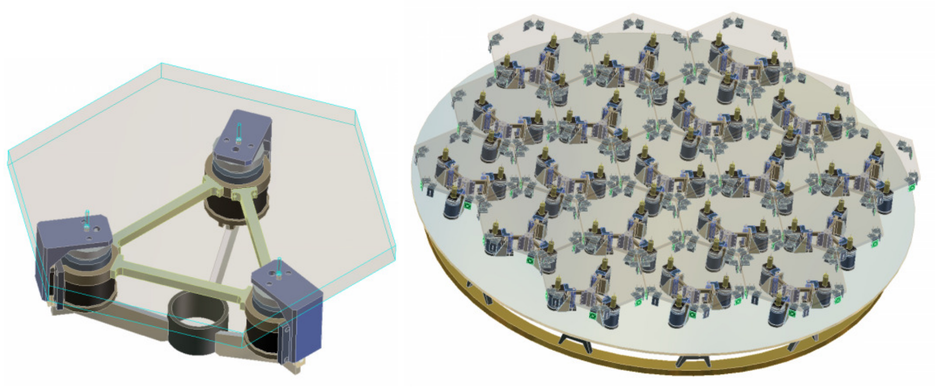

Figure 11-1. CAD design for the planned unit [49].

The Segmented Mirror Control (SMC) testbed is planned to be custom-designed, built and used in control-based experiments. Figure 11-1 shows both the first prototype segment that was built for proof-of-concept and the detailed CAD design of the entire testbed. The testbed consists of 19 hexagonal segments, 57 linear actuators and 84 hall effect edge sensors. A set of three linear actuators supports each segment allowing for tip, tilt and piston control motion. The edge sensors that ring each segment are used to estimate the relative displacement between adjacent segments. The segments will be mounted on a common support structure that will sit on a large "Unertl" tilt/rotation table (see Figure 11-2) that will simulate the gross telescope motion and, along with a shaker, induce vibrations. Note that while this research program is independent of the TMT project, the scaled SMC testbed matches the TMT primary mirror design requirements. We have obtained permission from the TMT project to use their design specifications for the testbed. Each segment, made of aluminum plates, will be approximately a ¼ scale of that of the actual TMT, which will be built at Mauna Kea, Hawaii, by 2018.

The SMC testbed will be capable of performing control-based experiments that simulate the complex 3D structural dynamics of a highly segmented primary mirror. It will be an experimental tool capable of addressing the following technical challenges: control-structure interactions, distributed control of multi-input multi-output systems, distributed model and controller scalability, actuator and sensor testing, etc. The testbed will be an invaluable tool for analyzing the performance and robustness of our new distributed controllers and for addressing various practical implementation issues involved in such a scheme, including the required network communication protocols. It will also be used to verify and improve Herzberg Institute of Astrophysics (HIA)'s extensive IM, ultimately helping in their future involvement and planning of large optical telescope projects worldwide.

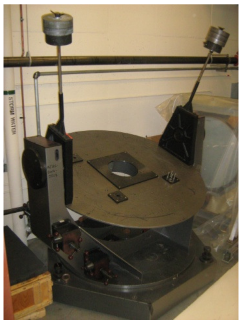

Figure 11-2. "Unert" tilt/rotation table.

Various components of the test unit were decided and the samples were assembled into a single segment prototype. This prototype is going to be used to assess the performance of the sample parts before placing orders for the remaining parts of the additional 18-segments.

Following is the brief information about the components that are going to be tested. A detailed list of the available and required components is given in Table 11-1.

Actuators: MotiCont LVCM-051-051-01 voice coil actuators are chosen for the control of three out-of-plane degrees of freedom. The main reason for the choice of these actuators is because they are non-contact; that is they have a long life cycle. The wire wounded coil and magnetic core are coupled through the magnetic field interactions. By being non-contact, there is less concern about the torn-worn effects. In addition, this type of actuators does not bring any limitation to the control bandwidth to be used. Bandwidth of the actuators almost infinite compared to the other components in the design. Each voice coil actuator can supply 28 N of continuous force with peak force up to 88 N.

Amplifiers: A current amplifier is required to supply power to each actuator. A-M-C® AZ12A8 amplifier found compatible with our design. These amplifiers can provide 6 Amps of continuous current with 12 Amps of peak current which is more than required by the actuators. ±10 V analog voltage will be used to control the current to the actuators.

DC Power Supply: A DC power supply is going to be used to supply power to the amplifiers. A-M-C® PS300W24 is going to be used in our design. This 300 Watt power supply can provide 12 A of output current at 24 Volts, which is compatible with the amplifier input specs. Our 19-segment test unit will require a total of seven of these power supplies.

Data Acquisition Board: Quanser Q8 board with QuaRC® software is going to be used for input-output data acquisition. This card has 8 analog inputs, 8 analog outputs and 32 digital I/Os which can operate at 2 MHz sampling rate. Hence, multiplexing is needed to support more inputs and outputs. According to our calculations, control bandwidth of around 200 Hz is required to control the 19-segment test unit. By the help of multiplexing, sufficient number of input and output ports can be obtained.

Encoders: MicroE Systems Mercury II™ 1600 linear optical encoders are going to be used to feedback the absolute position of the individual actuators with respect to the support structure.

Position Sensor: A MacroSensors™ PR-750 LVDT sensor is also going to be used to feedback the position information of the actuators. Each of these sensors requires a signal conditioner to operate. LVC 2500 signal conditioner supplied by the same company is compatible with the PR-750 sensor. The performances of the LVDT and the optical encoder are going to be compared and a decision will be made about the absolute position sensor for the 19-segment unit.

Edge sensor: Two candidate custom solutions are being considered for the relative displacement sensor. A Hall Effect sensor and laser Doppler sensor are currently the two candidates for the inter-edge displacement sensing. Sample laser Doppler sensors are going to be obtained by hacking laser computer mice, whereas sample Hall Effect sensors are ready to be mounted to single segment prototype.

Table 11-1. List of available and required components for the SMC.

Item	Description
A	**Linear actuators and sensors required for the 19-segment SMC testbed:** A.1 Linear voice coil actuator: (3 units already available) MotiCont, LVCM 051-051-01, 54 units A.2 LVDT sensor as encoder for the above actuator: (3 units already available) Macro Sensors, PR750-500, 54 units A.3 LVDT signal conditioner: (3 units already available) EAZY-CAL, MME-1000, 54 units A.4 Amplifier for the actuator: (3 units already available) Advanced Motion Controls, AZ12A8, 54 units A.5 Linear slide support for the actuator: (3 units already available) THK, HSR 12R, 54 units A.6 DC power supply: (1 unit already available) AMC, PS300W24, 18 units A.7 Hall effect displacement edge sensors: (1 prototype unit already available) Custom-built using Analog Devices AD22151 magnetic field sensor, 84 units
B	**Real-time rapid control prototyping controller required for the 19-segment SMC testbed for advanced control development and testing:** B.1 Real-time control hardware: Quanser, Q8-USB, 7 units Quanser, Q2-USB, 1 unit B.2 Real-time control software: Quanser, QuaRC real-time control software, 1 license

	B.3 Host computer configured to run above hardware and software
C	**Machining and material costs for the 19-segment SMC testbed:** C.1 General assembly: (3 units already available) Custom, 54 units C.2 Mirror blank assembly: (1 unit already available) Custom, 18 units C.3 Central hub assembly: (1 unit already available) Custom, 18 units C.4 Actuator assembly: (3 units already available) Custom, 54 units C.5 Arm assembly: (3 units already available) Custom, 54 units C.6 HE magnet bracket assembly: (12 units already available) Custom, 72 units C.7 Support structure assembly: (3 units already available) Custom, 54 units

In addition to the components of the segments, a preliminary study of the platform to run the distributed controllers is also investigated. In this preliminary study a 'Distributed control system' (DCS) is built to test the capabilities of QuaRC software and gumstix platform. 'Distributed control system' (DCS) refers to a dynamic system, in which the controller elements are not central in location (like the brain) but are distributed throughout the system with each component subsystem controlled by individual controllers. The entire system of controllers is connected by networks for communication and monitoring. Hence, the overall objective of the preliminary study is to implement distributed control in real time and apply innovative technologies of Quanser in developing the required network communication protocol for distributed control of extremely large telescopes. Quanser's QuaRC rapid prototyping and implementation environment is used in the realization of distributed controllers on gumstix. Gumstix are computers which are approximately in the size of stick of a gum with limited capabilities. Each gumstix with wireless communication capabilities is chosen to run distributed controllers that will control one or more segment alignments in the telescope mirror. A data acquisition hardware compatible with gumstix is needed to sample and send sensor and actuation signals, respectively. The main reason in the selection of gumstix over microcontrollers is their compliance with QuaRC that makes real-time implementation of Simulink models on such targets straight forward. Moreover, already available communication options in QuaRC libraries also played an important role in this selection.

In the realization of distributed control, first step is the design of controller models in Simulink environment. In these models, the communications among neighbouring segments are achieved by the help of Quanser's QuaRC Simulink communication blocks. TCP/IP is chosen as the communication protocol among neighbouring segments. In each model, the IP addresses of neighbouring segments and server and clients pairs are specified in a suitable fashion to minimize communication bandwidth as much as possible. Each model is then compiled using QuaRC compiler with gumstix specified as the target system. After compilation, the models are uploaded and run on target gumstix through wireless ad-hoc network connection. A central desktop computer is used to monitor the communications, sensor feedbacks and the resulting actuation commands.

In this prelimary study, we showed how distributed controllers can be implemented by using Quanser's innovative real-time control tools. Quanser's rapid prototyping environment QuaRC and its compatible platform gumstix are also shown to be suitable for easy prototyping and implementation of distributed controllers and their communications through Simulink. Also, the communication and control bandwidth characteristics and limitations of such platforms are investigated and some recommendations are mentioned below.

The wireless communication capabilities of the gumstix force the designer to limit the number of controllers that can be run on same target. Also, the bandwidth of such controllers is limited to approximately 500 Hz. Any increase in the controller bandwidth is not allowed by the QuaRC compiler. Any additional controller that is tried to run on same target results in package losses due to the soft real-time characteristic of gumstix Linux arm operating system. Another problem with the usage of gumstix is their incompetency with most of the high capability and precision data acquisition hardware.

This limits the precisions of sampled feedback sensor and sent actuation command signals.

The finite element analysis of our segmented mirror design shows that controller bandwidths of 50 Hz or less will be required from the distributed controllers. The same analysis of the TMT also gives comparable numbers. This limit is well below the gumstix capabilities. However for control applications where high bandwidth is needed, gumstix may not be able to satisfy the requirements.

Although in this preliminary study sample implementation of distributed controllers are investigated for segmented mirrors, distributed control is not limited to next generation telescope control. Same approach can easily be extended to other control applications like satellite control, group of automated vehicles, unmanned air vehicles...etc. Especially for unmanned air vehicles, the light weight and wireless communication capabilities of gumstix will be very advantageous in the implementation of distributed controllers.

12. CONCLUSIONS AND FUTURE WORK

12.1 Conclusions

This thesis focuses on the distributed H_∞ control of next generation ground-based extremely large optical telescopes. Next-generation extremely large telescopes will employ segmented mirrors to increase the overall area of the light collecting mirror (i.e. primary mirror). The segmented mirrors, when compared to a monolithic design for a mirror over approximately 8 meters diameter, yield a more cost effective design. Most of the largest telescopes operating today have segmented designs. Particularly the hexagonal segmented designs of two of the largest telescopes Keck telescope and Gran Telescopio Canarias proved the feasibility of the hexagonal design in increasing the primary mirror size. Following the same design principles, engineers have planned two extremely large telescopes: the North American project for the Thirty Meter Telescope and the EU project for the European Extremely Large Telescope. Although the design principles are similar, there will be a big difference in terms of the size of the primary mirror and in the number of segments employed, and the current control techniques seem to be not adequate to maintain the shape of the primary mirror against wind inside the telescope dome. In the Keck telescope, a static controller is used to correct the mirror shape by assuming a rigid support and ignoring the wind effect. However with the next generation telescopes, because of the lower natural frequencies of the larger primary mirrors and the greater wind effects on larger primary mirrors, structural deformations will be significant enough to include it in the controller design. In addition, with the sheer number of segments in the next generation telescope projects, the calculations required by a centralized scheme where all sensor data is fed and actuation signals are calculated become very hard to be handled by a single computing unit. Also this scheme has the potential of stopping the device during important observations as a result of a failure of the computing unit. Therefore, distributed control architecture is proposed to be able to address the structural deformations that couples neighbouring segments at the dynamic level and to maintain a smooth surface that couples neighbouring segments at the objective level. In this architecture, a controller with small control matrices has been proposed to control a single segment and by sharing information among neighbouring segments' controllers two levels of coupling can be addressed. This scheme also makes the control system more robust compared to the centralized scheme as any failure of a control will result in local errors on the surface of the primary mirror.

The main focus in the control of telescopes is to focus as much light as possible (that is emitted from a distant point in space) to an area that is as smaller as possible on the image plane. However as the light travels towards the optical telescope's primary mirror and is focused on the image plane, its wavefront gets distorted by various sources of disturbances. Generally the control of the telescope is separated to four levels to account for the disturbances. Adaptive optics aims at correcting the wavefront by sensing the shape of the wavefront and using a deformable secondary mirror to indirectly account for various atmospheric disturbances resulting from the changes in the refractive index of the air. The tracking of the celestial bodies and the rigid body alignments are addressed by other levels of control. In active optics, mainly the shape of the primary mirror is corrected against disturbances like thermal, gravitational, wind disturbances. In this thesis, we focused on the shape control of the primary mirror of the next generation extremely large telescopes against wind disturbance. Wind disturbance as mentioned in various studies will be the main source of the disturbance for the next generation extremely large telescopes' active optics problem.

Even with a perfectly operating telescope the quality of the images obtained from observations are bounded by the limit called the diffraction limit. Any opaque object on the optical path of the telescope results in the diffraction phenomenon. This limit can be calculated by the nature of the light observed and the geometric properties of the telescope. If the surface error that we focused in this thesis can be kept below a certain limit, the observations can be considered as the diffraction-limited as the error stays in below the threshold already determined by the diffraction. This limit can easily be taken into account by the H_∞ control synthesis. Also H_∞ control allows accounting for the small spatial variances among single segment dynamics. Moreover, it results in controllers that guarantee the stability and the imaging performance requirements in all closed-loop gain scenarios.

In this thesis, the performances of three distributed H_∞ controller synthesis techniques (Fourier-based, LMI-based, and Decomposition-based) were evaluated on the three system models: dynamically uncoupled, dynamically coupled and Thirty Meter Telescope primary mirrors.

First, the three models have been presented in Chapter 2 followed by the discussion of the three control techniques in Chapters 3, 4 and 5. In Chapters 6 and 7 present a preliminary study for the dynamically uncoupled primary mirror segments. In Chapter 6, a Fourier-based controller and in Chapter 7, a decomposition-based controller, are shown to satisfy the imaging performance requirements for 37-segment and 492-segment (TMT-like) models, respectively. In Chapters 8 and 9, in addition to the objective couplings, structural couplings are also accounted for. Here, the 7-segment and 492-segment (TMT-like) dynamically coupled models have been utilized to test the performances of Fourier-based and LMI-based controllers capable to address structural couplings. In Chapter 10, LMI-based and Fourier-based controllers are tested on the model obtained from the finite element analysis of the finite element model of the Thirty Meter Telescope provided by NRC-HIA. Also, it is shown that Fourier and LMI-based controller synthesis can also take the small variances among individual segment model dynamics into account. In Chapter 11, a possible system implementation for the performance evaluation of distributed controllers is presented. The brief information of various components to realize an experimental set up is given.

12.2 Future works

The study presented in this dissertation can be further improved by evaluating the performances of the distributed controllers on a real-time experimental set up. A single segment unit is already assembled. The components bought and the custom equipment built for a single segment should be tested and their performances should be validated. An additional 18 segments could be added to create a two-ring 19 segment experimental set up where the inner ring will be isolated from boundary conditions. Even though in order to test the performances of the distributed controllers at least 7 segments are required to complete one ring segmented mirror, by using a single segment and assuming virtual segments hardware-in-the-loop type simulations can be carried out. A preliminary study of hardware-in-the-loop type communications network by using gumstix and QuaRC software has already been carried out. The results of this preliminary study are discussed in the previous chapter. As the next step, gumstix can be equipted with data acquisition capabilities and the single segment sensor signals can be sampled, processed and the command signals to the actuators can be delivered through the gumstix input-outputs (I/Os). And as described in the preliminary study, additional Simulink models can be run as executable threads on the desktop PC. Wireless communications can be tested through desktop PC ports and the gumstix.

In all simulations throughout this thesis, Matlab Simulink environment is used. For better visualization of the segmented mirror system, by the help of Matlab graphical user interface packages a visual simulation environment can be designed. Although Matlab's graphical user interface packages can give a visualization of the overall system, it will still be hard to separate segments and their controllers from each other. In other words, all system components are needed to be simulated using a single Simulink model where all components are integrated. In order to overcome the Matlab's limitations, a platform that allows multithreading can be utilized. For this purpose extensive coding may be required. One example of such platforms is the Java platform where each segment controller can be modeled as a thread with its own communication capabilities. Overall primary mirror model can be simulated in a separate thread with accessible I/Os for the sensor feedback and actuator command signals. Hence in this scheme, each controller with its own I/Os can be connected to a single segment I/Os in the overall primary mirror model and to the neighbouring segment controllers spatial I/Os. Since each segment controller runs as a separate thread a simulation environment closer to the actual system with varying sampling times can be designed. A 3-D user interface in Java can easily be designed that visualizes the movements of primary mirror by getting model data from the overall primary mirror thread.

Although in this thesis distributed H_∞ control is focused on for the reasons listed in the first chapter, another way to approach the problem as was done in [31] is to use H_2 control. However with the H_2 approach the stability margins would not be as good as the H_∞ type approach and small uncertainties in the system model could result in system instabilities. In order to overcome this problem and also account for the small variances among single segment models, a mixed H_2/H_∞ approach can be followed. While the performance objectives can be attained by the H_2 synthesis, variances can be addressed by the H_∞ robustness analysis. Although mixed approach can result in a system where the performances cannot be guaranteed for all closed-loop system gains, since H_2 synthesis problem has exact solutions distributed controller synthesis would be much faster compared to the suboptimal synthesis of H_∞ controllers.

In our simulations, we assumed that the sensor data is available to us with noise comparable to the Keck noise. A further improvement in simulations could be to model the sensor system in the segmented primary mirror as the sensor drift may need to be accounted for in the controller synthesis.

Another interesting investigation could be the effect of the extent of the communication neighbourhood to the performance of the overall closed-loop system. In this thesis, only the nearest neighbouring segments are assumed to communicate with each other. However, for the Fourier and Decomposition-based methods this neighbourhood can be extended to cover the second ring surrounding a segment. In other words, in this thesis one segment controller is assumed to communicate with 7 neighbouring segment controllers that constitute the one-ring neighbourhood. This can be extended to 19 segments for two-ring or 37 segments for three-ring neighbourhoods.

Bibliography

[1] D. Enard, A. Marechal, J. Espiard, Progress in ground-based optical telescopes, Reports on Progress in Physics, 59(5) (1996) 601-656.

[2] P. Bely, The design and construction of large optical telescopes, New York: Springer, 2003.

[3] L.N. Allen, R.E. Keim, T.S. Lewis, J.R. Ullom, Surface error correction of a Keck 10-m telescope primary mirror segment by ion figuring, In 8th Intl Symp on Gas Flow and Chemical Lasers, International Society for Optics and Photonics, (1992) 195-204.

[4] J.M. Rodriguez-Espinosa, P. Alvarez, Gran Telescopio Canarias: a 10-m telescope for the ORM, Proceedings of SPIE, 2871 (1997) 69-73.

[5] J. Nelson, Thirty-Meter Telescope: progress and approaches, Proceedings of SPIE, 6986 (2008) 02.1-14.

[6] A. Preumont, R. Bastaits, G. Rodrigues, Scale effects in active optics of large segmented mirrors, Mechatronics, 19(8) (2009) 1286-1293.

[7] Thirty Meter Telescope Project, Online: www.tmt.org, (2014).

[8] R.N. Wilson, The history and development of the ESO active optics system, The Messenger, 113 (2003) 2-9.

[9] Airy Disk, Online: en.wikipedia.org/wiki/Airy_disk, (2014).

[10] H.W. Babcock, The possibility of compensating astronomical seeing, Publications of the Astronomical Society of the Pacific, (1953) 229-236.

[11] G.Z. Angeli, M.K. Cho, M.S. Whorton, Active optics and control architecture for a giant segmented mirror telescope, Proceedings of SPIE, 4840 (2003) 129-139.

[12] Subaru Telescope Improves its Eyesight by a Factor of Ten, Press Release, Online: www.naoj.org/Pressrelease/2006/11/20/index.htm, (2006).

[13] K. Tapping, Removing the twinkle, Online: www.nrc-cnrc.gc.ca/eng/education/astronomy/tapping/2010/2010-08-25.html, (2010).

[14] L. Noethe, Active optics in modern, large optical telescopes, Progress in optics, 43 (2002) 1-70.

[15] R.W. Cohen, T.S. Mast, J.E. Nelson, Performance of the W.M. Keck telescope active mirror control system, Advanced Technology Optical Telescope V, Proceedings of SPIE, 2199 (1994) 105-116.

[16] J.N Aubrun, K. Lorell, T. Mast, J. Nelson, Dynamic analysis of the actively controlled segmented mirror of the W.M. Keck ten-meter telescope, IEEE Control Systems Magazine, 7(6) (1987) 3-10.

[17] J. Spyromilio, Real-time control for the world's largest telescope, Advanced Imaging Magazine, Online: sine.ni.com/cs/app/doc/p/id/cs-11465, (2009).

[18] D.G. MacMynowski, P.M. Thompson, M.J. Sirota, Analysis of TMT primary mirror control-structure interaction, Proceedings of SPIE, 7017 (2008) 15.1-12.

[19] H. Raza, P. Ioannou, Vehicle following control design for automated highway systems, IEEE Control Systems, 16(6) (1996) 43-60.

[20] G.B. Shaw, The generalized information network analysis methodology for distributed satellite systems, PhD Thesis, Massachusetts Institute of Technology, MA, 1999.

[21] S.S. Stankovic, M.J. Stanojevic, D.D. Siljak, Decentralized overlapping control of a platoon of vehicles, IEEE Transactions on Control Systems Technology, 8(5) (2000) 816-832.

[22] P. Seiler P, Coordinated control of unmanned aerial vehicles, PhD Thesis, University of California, Berkeley, CA, 2001.

[23] E. Kamen, Stabilization of linear spatially-distributed continuous-time and discrete-time systems, Multidimensional System Theory, (1985) 101-146.

[24] B. Bamieh, F. Paganini, M.A. Dahleh, Distributed control of spatially invariant systems, IEEE Transactions on Automatic Control, 47(7) (2002) 1091-1107.

[25] R. D'Andrea, G.E. Dullerud, Distributed control design for spatially interconnected systems, IEEE Transactions on Automatic Control, 48(9) (2003) 1478-1495.

[26] P. Massioni, M. Verhaegen, Distributed control of identical dynamically coupled systems: a decomposition approach, IEEE Transactions on Automatic Control, 54(1), (2009) 124-135.

[27] N. Yaitskova, K. Dohlen, P. Dierickx, Analytical study of diffraction effects in extremely large segmented telescopes, Journal of the Optical Society of America, 20(8) (2003) 1563-1575.

[28] D.W. Gu, P.H. Hetkov, M.M. Konstantinov, Robust Control Design with MatLab, Springer, 2005.

[29] T.S. Mast, J.E. Nelson, Figure control for a fully segmented telescope mirror, Applied Optics 21(14) (1982) 2631-2641.

[30] C. Shelton, T. Mast, G. Chanan, J. Nelson, J. Roberts, C. Lewis, M. Troy, et al. Advances in edge sensors for the thirty meter telescope primary mirror, Proceedings of SPIE, 7012 (2008) 10.1-13.

[31] S. Jiang, P.G. Voulgaris, L.E. Holloway, L.A. Thompson, H_2 control of large segmented telescopes, Journal of Vibration and Control, 15(6) (2009) 923-949.

[32] D. Kerley, Distributed control of a segmented telescope mirror, Master's Thesis, University of Victoria, BC, Canada, 2010.

[33] B. Recht, R. D'Andrea, Distributed control of systems over discrete groups, IEEE Transactions on Automatic Control, 49(9) (2004) 1446-1452.

[34] R.S. Chandra, J.M. Fowler, R. D'Andrea, Control of interconnected systems of finite spatial extent, Proceedings of 41st IEEE conference on decision and control, (2002) 238-239.

[35] M. Hovd, S. Skogestad, Control of symmetrically interconnected plants, Automatica 30 (6) (1994) 957-973.

[36] M.K. Sundareshan, R.M. Elbanna, Large-scale systems with symmetrically interconnected subsystems: Analysis and synthesis of decentralized controllers, Proceedings of 29th IEEE conference on decision control, (1990) 1137-1142.

[37] R.W. Brockett, J.L. Williems, Discretized partial differential equations: Examples of control systems defined on modules, Automatica, 10(4) (1974) 507-515.

[38] M. Hovd, R.D. Braatz, S. Skogestad, SVD controllers for H_2, H_∞ and μ-optimal control, Automatica, 33(3) (1994) 433-439.

[39] J.G. VanAntwerp, A.P. Featherstone, R.D. Braatz, Robust cross-directional control of large scale sheet and film processes, Journal of Process Control, 11 (2001) 149-177.

[40] J.W. Brewer, Kronecker products and matrix calculus in system theory, IEEE Transaction on Circuits Systems, 25(9) (1978) 772-781.

[41] B. Ulutas, E.J. Park, A. Suleman, Distributed and centralized H_∞ control of large segmented telescopes, Proceedings of ASME International Mechanical Engineering Congress and Exposition, Vancouver, BC, (2010) 1129-1137.

[42] B. Ulutas, E.J. Park, A. Suleman, Decomposition-based distributed H_∞ control of large segmented telescopes, Proceedings of CSME International Congress, Toronto, ON, (2014).

[43] C. Baffes, T. Mast, J. Nelson, E. Ponslet, V. Stephens, L. Stepp, E.C. Williams, Primary mirror segmentation studies for the Thirty Meter Telescope, Proceedings of SPIE, 7018 (2008) 0S.1-15.

[44] B. Ulutas, D. Kerley, J. Dunn, A. Suleman, E.J. Park, Distributed H_∞ control of dynamically coupled segmented telescope mirrors: Design and simulation, Mechatronics, 22(1) (2012) 121-135.

[45] B. Ulutas, E.J. Park, A. Suleman, LMI-based Distributed H_∞ control of dynamically coupled large segmented telescope mirrors, Proceedings of IEEE/ASME International Conference on Advanced Intelligent Mechatronics, Besancon, France, (2014).

[46] K. Vogiatzis, A. Segurson, G.Z. Angeli, Estimating the effects of wind loading of telescope performance using computational fluid dynamics, Proceedings of SPIE, 5497 (2004) 311-320.

[47] G.Z. Angeli, M.K. Cho, M. Sheehan, L.M. Stepp, Characterization of wind loading of telescopes, Proceedings of SPIE, 4757 (2002) 72-83.

[48] T.S. Mast, G. Gabor, J.E. Nelson, Edge sensors for a segmented mirror, Proceedings of SPIE, 0444 (1983) 297-309.

[49] A. Anthony, Mechanical design of a segmented telescope testbed, Honour's thesis, University of Victoria, Victoria, BC, Canada, 2010.